Fisheries and Oceans Canada | Pêches et Océans Canada
Ecosystems and Oceans Science | Sciences des écosystèmes et des océans

Canadian Science Advisory Secretariat (CSAS)

Research Document 2021/002

Québec Region

Chemical and Biological Oceanographic Conditions in the Estuary and Gulf of St. Lawrence during 2019

M. Blais, P. S. Galbraith, S. Plourde, L. Devine and C. Lehoux

Fisheries and Oceans Canada
Institut Maurice-Lamontagne
850 route de la Mer, P.O. Box 1000
Mont-Joli, QC, G5H 3Z4

February 2021

Foreword

This series documents the scientific basis for the evaluation of aquatic resources and ecosystems in Canada. As such, it addresses the issues of the day in the time frames required and the documents it contains are not intended as definitive statements on the subjects addressed but rather as progress reports on ongoing investigations.

Published by:

Fisheries and Oceans Canada
Canadian Science Advisory Secretariat
200 Kent Street
Ottawa ON K1A 0E6

http://www.dfo-mpo.gc.ca/csas-sccs/
csas-sccs@dfo-mpo.gc.ca

ISSN 1919-5044

Correct citation for this publication:

Blais, M., Galbraith, P.S., Plourde, S., Devine, L. and Lehoux, C. 2021. Chemical and Biological Oceanographic Conditions in the Estuary and Gulf of St. Lawrence during 2019. DFO Can. Sci. Advis. Sec. Res. Doc. 2021/002. iv + 66 p.

Aussi disponible en français :

Blais, M., Galbraith, P.S., Plourde, S., Devine, L. et Lehoux, C. 2021. Les conditions océanographiques chimiques et biologiques dans l'estuaire et le golfe du Saint-Laurent en 2019. Secr. can. de consult. sci. du MPO. Doc. de rech. 2021/002. iv + 68 p.

TABLE OF CONTENTS

ABSTRACT

An overview of chemical and biological oceanographic conditions in the Gulf of St. Lawrence (GSL) in 2019 is presented as part of the Atlantic Zone Monitoring Program (AZMP). Data from the AZMP regional monitoring program were analyzed and results were described in relation to long-term means (climatology) in the context of a strong warming event that began in 2010. During 2019, oxygen at 300 m depth reached the lowest concentration observed to date in the Estuary, while the second or third lowest concentrations of the time series were observed in other subregions. The nitrate inventories in the surface (0–50 m) layer were near or slightly above normal during wintertime and generally below normal during summer and fall, suggesting that a large nitrate drawdown occurred between March and June, particularly in the southern (sGSL) and eastern (eGSL) GSL. In 2019, the deep water (300 m) nitrate inventory was near normal in eGSL, a first since 2012 when intrusions of warm and salty waters started to be observed in association with above-normal nitrate inventories. However, deep phosphate and silicate inventories remained above normal in 2019 in the GSL. Despite an overall large spring nitrate drawdown, satellite imagery indicates that the spring bloom had below-normal magnitude and amplitude across the GSL. The annual anomalies of vertically integrated chlorophyll *a* (chl *a;* 0–100 m) were above normal in the western GSL (wGSL) and eGSL mostly because of high chl *a* concentrations during fall. Taxonomic analyses showed a large proportion of diatoms at Rimouski station in 2019, while most of the phytoplankton abundance consisted in small-sized cells at Shediac Valley station. Zooplankton biomass in 2019 was above normal at Rimouski station and in wGSL for the first time since 2013-2014, but remained below normal elsewhere in the GSL. The abundances of large calanoid were either near or slightly above normal in all subregions in 2019. It was mostly due to near-normal abundances of *Calanus finmarchicus* everywhere, high abundances of *Calanus hyperboreus* at Rimouski station and in wGSL (spring only), and to record high abundance of *Calanus glacialis* in eGSL. Small calanoid and warm-water-associated copepod abundances were generally near or above normal , in agreement with the trend observed in recent years. The abundances of cold-water-associated copepods were above normal in eGSL due to *C. glacialis,* and at a record high at Shediac Valley station due to both *C. glacialis* and *Metridia longa*. The phenology of *C. finmarchicus* at Rimouski station suggests a near-normal or slightly early timing of emergence from diapause and development into the adult stage. The peak of the early copepodite stages (CI–CIII) started early in May but was long-lasting and reached its maximum abundance in late June. The infrequent and irregular sampling at Shediac Valley limited our ability to describe seasonal patterns associated with nutrients or lower trophic levels at this station.

INTRODUCTION

The Atlantic Zone Monitoring Program (AZMP) was implemented in 1998 (Therriault et al. 1998) with the aim of (1) increasing Fisheries and Oceans Canada's (DFO) capacity to understand, describe, and forecast the state of the marine ecosystem and (2) quantifying the changes in the ocean's physical, chemical, and biological properties and the predator–prey relationships of marine resources. AZMP provides data to support the sound development of ocean activities. A critical element in the AZMP observational program is the annual assessment of the distribution and variability of nutrients and the plankton communities they support.

A description of the spatiotemporal distribution of dissolved oxygen, nutrients (nitrate, silicate, and phosphate), and chlorophyll a (chl a) concentrations provides important information on water mass movements and on the location, timing, and magnitude of biological production cycles. A description of phytoplankton and zooplankton distributions provides important information on the organisms forming the base of the marine food web. Understanding plankton production cycles is essential for an ecosystem approach to fisheries management.

The AZMP derives its information on the state of the marine ecosystem from data collected at a network of sampling locations (high-frequency monitoring stations, cross-shelf sections) in each DFO region (Québec, Gulf, Maritimes, Newfoundland and Labrador; see Figure 1 for Québec region station locations) occupied at a frequency of weekly to once annually. The sampling design provides valuable information on the natural variability in physical, chemical, and biological properties of the Northwest Atlantic continental shelf: cross-shelf sections provide detailed geographic information but are limited in their seasonal coverage while strategically located high-frequency monitoring stations complement the sampling by providing more detailed information on seasonal-scale changes in ecosystem properties.

In this document, we review the chemical and biological oceanographic (lower trophic levels) conditions in the Gulf of St. Lawrence (GSL) in 2019. Physical oceanographic conditions that prevailed in 2019 are described in Galbraith et al. (2020). The annual average freshwater discharge into the Estuary was at its highest level since 1976. The maximum volume of sea-ice was near normal, but the winter mixed layer volume was at a record high due to large inflow of Labrador Shelf Water. The May to November average sea-surface temperature (SST) was below normal. Overall, the annual average SST in 2019 was the second coldest (after 2018) since 2002. The seasonally averaged minimum temperature of the cold intermediate layer (CIL) was near normal. Deep-water temperatures (> 150 m) were above normal, with inward advection from Cabot Strait: GSL annual average temperature reached record highs at 250 m and 300 m. This report describes the 2019 production cycles and community composition of phytoplankton and zooplankton in the context of these physical conditions.

METHODS

SAMPLE COLLECTION

All sample collection and processing steps meet the standards of the AZMP protocol (Mitchell et al. 2002). Field measurements included in this report were made along seven oceanographic sections during surveys carried out in winter, summer, and fall (mainly in March, June, and November) of each year and at two high-frequency monitoring stations (Figure 1). In this document, the seven sections, as well as supplementary stations in between sections, were grouped into three subregions to better match spatial scales addressed by AZMP in other regions (Figure 2):

(1) western GSL (wGSL): this region is generally deep (> 200 m) and cold in summer. It is strongly influenced by freshwater runoff from the St. Lawrence River and cold and dense waters from the Laurentian Channel. It includes TESL, TSI, and TASO;

(2) southern GSL (sGSL): this region is shallow (< 100 m) and warm in summer. It is under the influence of the Gaspé Current and includes TIDM only;

(3) eastern GSL (eGSL): this region, with deep channels and a relatively wide shelf (< 100 m), is characterized by high surface salinity and is directly influenced by the intrusion of water from the Labrador and Newfoundland shelves. It includes TCEN, TDC, and TBB.

Table 1 provides details about the 2019 sampling surveys and Figures 2 and 3 summarize the sampling effort during the seasonal AZMP surveys and at the high-frequency monitoring stations, respectively. Rimouski station (depth 320 m) has been sampled since 1991—about weekly throughout the summer, once or twice a month in early spring and late fall, and rarely in winter (except during the winter survey) because of sea ice. It has been included in AZMP's annual review of environmental conditions since 2004 to represent conditions in the St. Lawrence Estuary (SLE) and wGSL. Since the beginning of AZMP, Shediac Valley station (depth 84 m) has represented conditions in sGSL and the SLE outflow. Because of its remoteness, sampling frequency at Shediac Valley station is closer to monthly between May–November and decreases during January–April. Sampling at oceanographic sections and high-frequency monitoring stations includes a CTD profile (temperature, salinity, fluorescence, dissolved oxygen) as well as water sampling using Niskin bottles (surface, 5 m, 15 m, 25 m, 50 m, 100 m, 200 m, 300 m, 400 m, bottom). Water from the Niskin bottles is collected for the analysis of dissolved oxygen (Winkler method), nutrients (Technicon or Alpkem AutoAnalyzer), chlorophyll *a* concentration (chl *a*, fluorometer), and phytoplankton enumeration (inverted microscopy) (Mitchell et al. 2002). Finally, mesozooplankton (< 1 cm) is sampled with bottom-to-surface vertical ring net tows (75 cm diameter, 200 µm mesh) for identification, counts, and biomass measurements.

Since 1996, a survey of the winter surface mixed layer of the GSL has been conducted, usually in early to mid-March, using a Canadian Coast Guard (CCG) helicopter. Surface nutrients (2 m) have been sampled since 2001 (Galbraith 2006, Galbraith et al. 2006), and additional depths were sampled in March 2016 and 2017 because sampling was carried out from CCG ships rather than the helicopter during these two years. The winter survey has added a considerable amount of data to the previously sparse winter sampling in the region. Over a hundred stations were sampled by helicopter from the 4th to 13th of March 2019.

OXYGEN

Oxygen concentrations at 300 m are used as a monitoring indicator of hypoxic conditions in the GSL since they are less variable over time than surface oxygen concentrations, which vary seasonally because of water column mixing and primary production. Oxygen concentration was measured using an oxygen probe (Sea-Bird SBE43) mounted on the CTD; the probe was calibrated against seawater samples collected and analyzed by Winkler titration on every cast (for the calibration procedure, see Sea-Bird application notes 61-1, -2, -3). Here, we present the mean annual distribution of deep oxygen in the GSL derived from the CTD-mounted probe along with time series of annual concentrations of deep oxygen.

NUTRIENTS AND PHYTOPLANKTON

Nutrient and chl *a* data collected along the AZMP sections and at the high-frequency monitoring stations were integrated over various depth intervals (i.e., 0–100 m for chl *a*; 0–50 m and 50–150 m for nutrients) using trapezoidal numerical integration. Chlorophyll *a* is used as a proxy for

phytoplankton biomass. The concentration at the upper integration limit is assumed to be the same as the one measured at the shallowest sampling depth, and the concentration at the lower integration limit is assumed to be the same as the concentration of the sample collected at the closest depth to the lower integration limit. In 2016 and 2017, the vertical profiles of nutrients in the GSL revealed that nitrate concentrations were relatively homogeneous in the upper 50 m of the water column during winter. Thus, for years when vertical nutrient profiles were not available, including 2019, integrated nitrate values for the winter survey were calculated using surface concentrations (2 m) × 50 m, assuming homogeneity of nitrate concentrations in the winter mixed layer.

In this document, a detailed description of the seasonal patterns is provided for different nutrient and phytoplankton indices. For the high-frequency monitoring stations, we present nitrate inventories in surface, mid, and deep water column layers, chl *a* concentration, total phytoplankton abundance, and the relative abundance of its main taxa. Taxonomic identification of phytoplankton is performed for high-frequency monitoring stations only. The ratio between diatoms and flagellates, or between diatoms and dinoflagellates can be used as a proxy for the phytoplankton community size-structure. For the three GSL subregions described above, the seasonal nitrate and chl *a* concentrations integrated over different depth layers as well as the spatial distribution of nutrients (nitrate, phosphate, silicate, N:P ratio) and chl *a* are presented. Spring nutrient drawdown was estimated using the difference between the March and June nitrate inventories and is used as a proxy for phytoplankton spring production since sampling occurs after the spring bloom. Anomalies were computed for these indices (see Scorecard section below) for both high-frequency monitoring stations and GSL subregions.

SATELLITE REMOTE SENSING OF OCEAN COLOUR

Satellite ocean colour data provide large-scale images of surface phytoplankton biomass (chl *a*) over the Northwest Atlantic. We used two-week satellite composite images of four GSL boxes (northwest and northeast GSL [NWGSL, NEGSL], Magdalen Shallows, Cabot Strait; see Figure 4 for locations) to supplement our ship-based observations, especially regarding spring bloom phenology, and to provide seasonal coverage and a large-scale context over which to interpret our survey data. The ocean colour imagery provides information about the timing and spatial extent of the spring and fall blooms but does not provide information on the dynamics that take place below the top few metres of the water column. In addition, satellite ocean colour data for the St. Lawrence Estuary are largely biased by suspended inorganic particles and coloured dissolved organic matter. Thus, these data cannot be used in an absolute manner. While knowledge on phytoplankton dynamics at the surface of the St. Lawrence Estuary during spring is gathered using the weekly sampling at Rimouski station, the temporal resolution is not sufficient to allow the calculation of bloom metrics as discussed below. Thus, the spring bloom metrics are not presented for the Estuary, but seasonal and interannual variability of phytoplankton biomass is described. In addition, the broad-scale oceanographic surveys include a transect in the Estuary (TESL) that is used to provide an estimate of phytoplankton concentrations during summer and fall in this region.

Near-surface phytoplankton biomass has been estimated from ocean colour data collected by the Sea-viewing Wide Field-of-view Sensor (SeaWiFS) satellite launched by NASA in late summer 1997, by the Moderate Resolution Imaging Spectroradiometer (MODIS) “Aqua” sensor launched by NASA in July 2002, and most recently by the Visible Infrared Imaging Radiometer Suite (VIIRS) satellite, launched in October 2011. In this report, SeaWiFS data from 1998–2007 and MODIS data from 2008–2011are combined with VIIRS data for the 2012–2018 period to construct a continuous time series of surface chl *a* in four GSL statistical boxes (Figure 4). The accuracy of the MODIS satellite in estimating chl *a* has been compared with that of SeaWiFS for

some regions of the globe. Although differences in sensor design, orbit, and sampling between MODIS and SeaWiFS cause some differences in calculated chl *a* values (Gregg and Rousseaux 2014), the biases associated with these satellites are overall not significantly greater than algorithm uncertainties, especially in non-turbid waters (Zibordi et al. 2006, Arun Kumar et al. 2015). Recent studies comparing all three sensors indicate that they provide consistent global ocean colour data records, with similar patterns and magnitudes, and generally high cross-sensor fidelity (Wang et al. 2013, Barnes and Hu 2016).

All statistical boxes for the satellite imagery are located outside of the St. Lawrence River plume because ocean colour data in this region are unreliable due to contamination by riverine inputs loaded with terrestrially derived coloured matter, as mentioned previously. Composite satellite images were provided by BIO's remote sensing unit (Bedford Institute of Oceanography, DFO, Dartmouth, NS) sourced from NASA's Goddard Space Flight Center. Basic statistics (mean, range, standard deviation) were extracted from semi-monthly average composites by averaging all pixels within each box (SeaWiFS and MODIS have a 1.5 km spatial resolution while VIIRS has a 1 km spatial resolution).

A shifted Gaussian function of time model was used to describe characteristics of the spring phytoplankton bloom based on the combined satellite data (Zhai et al. 2011). Four metrics were computed to describe the spring bloom characteristics: start date (day of year), cycle duration (days), magnitude (the integral of chl *a* concentration under the Gaussian curve), and amplitude (maximum chl *a*). In addition, seasonal mean chl *a* biomass during spring (March to May), summer (June to August), and fall (September to November) as well as annual average (March to November) were computed. For each of these eight metrics, we computed normalized annual anomalies (see Scorecard section below) to describe temporal trends for each statistical box.

ZOOPLANKTON INDICES

We provide a detailed description of the seasonal patterns for different zooplankton indices, mostly at Rimouski and Shediac Valley stations, but also for the three GSL subregions described above. For the high-frequency monitoring stations, we present total mesozooplankton biomass (dry weight), total copepod abundance, and the relative abundance of the copepod species making up 95% of total abundance. In addition, we include *Pseudocalanus* spp. (Rimouski station only) and *Calanus finmarchicus* abundances and stage composition. Because of its importance to the total zooplankton biomass in the GSL, a detailed description of *Calanus hyperboreus* is provided for Rimouski and Shediac Valley stations. We also present the spring and fall total zooplankton biomass and total abundance of *C. finmarchicus*, *C. hyperboreus*, and *Pseudocalanus* spp. for the three GSL subregions since they represent distinct oceanographic regimes. Since zooplankton samples are collected over the entire water column, zooplankton indices represent depth-integrated metrics.

Changes in zooplankton phenology were described using *C. finmarchicus*. We used the time series at Rimouski station because adequate sampling and stage identification started there 25 years ago (1994). However, sampling methodology changed over time. From 1994 to 2004, prior to the use of the AZMP standard nets (75 cm diameter, 200 µm mesh bottom-to-surface ring net tows) [Mitchell et al. 2002], *C. finmarchicus* copepodite stage abundance was determined using samples collected with 333 µm (CIV–CVI) and 73 µm (CI–III) mesh nets, towed from bottom to surface and from 50 m to surface respectively, that were analyzed for six years (1994, 1996–2000) of the time series (see Plourde et al. 2009 for details). In other years before 2004 for which 73 µm samples were not analyzed, the abundance of CI–III in the 333 µm samples was adjusted based on a comparison performed with a 158 µm mesh net (S. Plourde, DFO, Mont-Joli, QC; unpublished data). The phenology of *C. finmarchicus* was described using the following steps: (1) stage relative abundances were normalized (proportion of a copepodite

stage/maximum proportion for the stage) within each year for CI–III, CIV, CV, and CVI (male and female) and (2) stage proportions were smoothed using a Loess algorithm.

Finally, anomalies were computed for zooplankton biomass and for the abundance of several zooplankton indices that reflect either key copepod taxa, different functional groups, or groups of species indicative of cold- or warm-water intrusions and/or local temperature conditions specific to the GSL (see Scorecard section below) for both high-frequency monitoring stations and GSL subregions. A detailed list of species included in each large copepod index is presented in Appendix 1. Occasionally, taxonomists cannot distinguish *C. finmarchicus* from *C. glacialis* and record them in a common category. Since 2018, we used the results of a genetic study based on prosome length to distinguish these species (Parent et al. 2011). This could have had a minor influence on anomaly patterns discussed in previous reports.

SCORECARDS

Normalized anomalies for the chemical and biological indices presented in scorecards were computed for the high-frequency monitoring stations and oceanographic subregions. These anomalies are calculated as the difference between the variable's average for the season or for the complete year and the variable's average for the reference period (usually 1999–2015 unless otherwise noted); this number is then divided by the reference period's standard deviation.

Anomalies are presented as scorecards with positive anomalies depicted as shades of red, negatives as blues, and anomalies within ± 0.5 SD as white (considered as normal conditions, i.e., similar to the reference period). A standard set of indices representing anomalies of nutrient concentrations, phytoplankton biomass and bloom dynamics, mesozooplankton biomass, and the abundance of dominant mesozooplankton species and groups (*C. finmarchicus, Pseudocalanus* spp., total copepods, and total non-copepods) are produced for each AZMP region. To visualize Northwest Atlantic shelf-scale patterns of environmental variation, a zonal scorecard including observations from all AZMP regions is presented in DFO 2020.

Annual nutrient, phytoplankton, and zooplankton index anomalies are based on the mean annual concentration (mmol m^{-2} for nutrients and mg chl a m^{-2} for phytoplankton biomass) or density (cells L^{-1} for phytoplankton abundance and ind m^{-2} for zooplankton abundance) estimated at each high-frequency monitoring station and each GSL subregion. These annual estimates are the results of general linear models (GLM) of the form

$\text{Log}_{10}(\textit{Density}+1) = \alpha + \beta_{YEAR} + \delta_{MONTH} + \varepsilon$ for the high-frequency monitoring stations and $\text{Log}_{10}(\textit{Density}+1) = \alpha + \beta_{YEAR} + \delta_{STATION} + \gamma_{SEASON} + \varepsilon$ for the subregions,

as in Pepin et al. (2013) and Johnson et al. (2016); α is the intercept, and ε is the error. The GLM is applied to the three subregions separately. For the high-frequency monitoring stations, β and δ are the categorical effects for year and month, respectively. For the subregions, β, δ, and γ are the categorical effects of year, station, and season, respectively. The model's least-square mean based on type III sums of squares was used as the year average. Results of the GLM analysis for high-frequency monitoring stations and GSL subregions are presented in Appendices 2–6. We log-transformed concentrations and density values before computing anomalies to compensate for the skewed distribution of the observations. One was added to the *Density* term to include observations with a value of zero. Zooplankton biomass anomalies were also computed using GLM, without log-transformation.

OBSERVATIONS

PHYSICAL ENVIRONMENT

The temperature and salinity of the water column in 2019 are described in detail in Galbraith et al. (2020). Stratification is one of the key parameters controlling primary production. For this reason, we present the upper water column stratification at the high-frequency monitoring stations (Figure 5). The very large freshwater discharge into the Estuary during springtime (Galbraith et al. 2020) led to strong above normal stratification during May and June at Rimouski station and from June to August at Shediac Valley station.

DEEP OXYGEN

In the GSL, a dissolved oxygen value of 100 µM corresponds to approximately 30% saturation, below which the water is considered to be hypoxic and can reduce the survival of some species such as Atlantic cod (Plante et al. 1998). The lowest levels of dissolved oxygen (below 20% saturation in recent years) have been found in the deep waters at the head of the Laurentian Channel in the Estuary (Figure 6). In 2019, concentrations of dissolved oxygen at 300 m were again well below normal everywhere along the Laurentian Channel (Figure 6), reaching time-series record lows in the Estuary (Figure 7). The deep waters of the Estuary have consistently been hypoxic since 1984, and dissolved oxygen concentration was 52 µM in 2019, corresponding to ca. 17% saturation (Figure 7). Elsewhere, deep dissolved oxygen concentrations were the second or third (NWGSL) lowest of the time series, being slightly above the 2018 record lows (Figure 7).

NUTRIENTS AND PHYTOPLANKTON

Distributions of the dissolved inorganic nutrients (nitrate, silicate, phosphate) included in AZMP's observational program strongly co-vary in space and time (Brickman and Petrie 2003). For this reason and because the availability of nitrogen controls phytoplankton growth in coastal waters of the GSL, emphasis in this document is given to the variability in nitrate concentrations and inventories, even though the distributions of other nutrients are also briefly discussed. In this document, we use the terms "nitrate" or "total nitrate" to refer to nitrate+nitrite (NO_3^-+NO_2^-).

High-frequency monitoring stations

The main highlights of 2019 in terms of nitrate inventories and phytoplankton biomass are illustrated in Figure 8 for both high-frequency monitoring stations. Detailed vertical profiles and anomaly patterns of nitrate and chl *a* are shown in Figures 9 and 10 for Rimouski and Shediac Valley stations, respectively. On these latter figures, vertical profiles during 2017 and 2018 are also shown to provide some context. Nutrient and chl *a* concentrations are roughly two to three times higher at Rimouski station than at Shediac Valley station. The two stations typically exhibit a reduction in surface nitrate inventories in spring/summer mediated by phytoplankton consumption, a minimum during summer, and a subsequent increase during fall/winter once water column mixing intensifies due to cooling processes and wind forcing. However, chl *a* levels and phytoplankton abundance show distinct seasonal patterns between stations. Both indices reach their maximum during summer at Rimouski station (Figures 8c, 11a) while maxima are reached in early spring before diminishing rapidly and staying stable for the remainder of the season at Shediac Valley station (Figures 8d, 12a).

In 2019 at Rimouski station, nitrate inventories were near normal most of the year, except during spring when they were above normal, leading to high chl *a* concentrations in late April – early May (Figure 8a, c). Phytoplankton biomass was highly variable throughout the year,

varying between near to or slightly below normal levels and above normal values. Overall, the annual chl *a* inventory anomaly was positive, as was the annual intermediate layer nitrate inventory (Figure 8 scorecard). Most of the phytoplankton biomass was in the upper 15 m of the water column throughout the year, where nitrate inventories were depleted (Figure 9).

At Shediac Valley station, sampling was sparse and limited (Figure 8b, d), making the description of seasonal patterns difficult. Over the year, the surface nitrate inventory and chl *a* concentration were mostly near or slightly below normal, with the exception of a very high chl *a* concentration (ca. 550 mg m^{-2}) that was measured in early May (Figure 8b, d). At this moment, phytoplankton biomass was evenly distributed throughout the water column while it was restricted to the upper 15 m for the rest of the year (Figure 10). As we saw for the intermediate layer (50–150 m) at Rimouski station, deep nutrient values at Shediac Valley were above normal (Figure 8 scorecard).

Phytoplankton abundances at Rimouski station were near or below normal during spring–early summer and late fall and was above normal in between (Figure 11a), leading to a positive annual anomaly in 2019 for this index (Figure 13). The seasonal phytoplankton community composition was similar to the reference period, with an increased proportion of diatoms during summer and early fall (Figure 11b, c). Dinoflagellates showed an annual negative anomaly in 2019, continuing a trend observed since 2014 for this index as well as for the diatom:dinoflagellate ratio (Figure 13).

In contrast, the phytoplankton assemblage at Shediac Valley during 2019 was different from the climatology. The relative abundance of diatoms decreased from about 70% to less than 20% with a greater proportion of smaller-sized cells (Figure 12b, c). Annual anomalies were thus negative for diatoms and largely positive for dinoflagellates, flagellates, and ciliates (Figure 13). Since 2014, the anomaly pattern at Shediac Valley station has suggested that a change in the size structure of the phytoplankton community might be occurring. However, one must keep in mind that these anomaly patterns are the result of fewer than 10 phytoplankton samples analyzed each year in recent years. In 2019, only five samples were collected for phytoplankton identification and there was no sampling in April, when the spring diatom bloom usually occurs (Figure 12a).

Gulf subregions

An overview of the seasonal distributions of nutrient inventories, phytoplankton biomass, and their anomalies in the GSL is presented in Figures 14 to 20. Time series of regional annual and seasonal anomalies for nutrient concentrations and phytoplankton biomass are presented in Figures 21 and 22. The distributions of all nutrients in the surface layer during March 2019 were similar to the reference period (Figure 14) while their concentrations were generally below normal in sGSL and eGSL in June 2019 (Figure 15). While not dismissing possible changes in water mass composition through the year, this suggests large nutrient drawdown by phytoplankton during spring in these two regions (Figure 19). Nutrient concentrations in the surface layer were also mostly below normal during fall everywhere in the GSL (Figure 16), leading to negative annual nutrient anomalies in eGSL and sGSL (Figure 21). Interestingly, the N:P ratio showed strong negative anomalies in these two regions as well (Figures 15, 16). The mid-layer nutrient inventory also generally showed negative anomalies, except for the Gaspé Peninsula in summer and sGSL in fall (Figures 17, 18). In contrast, since 2012, there have been strong positive anomalies for deep nitrates in eGSL and for deep phosphates and silicates in eGSL and wGSL as well as negative N:P anomalies in these two regions at 300 m (Figure 21). This was also generally true in 2019, but the nitrate inventory was near normal in eGSL.

In June 2019, the phytoplankton biomass followed the average distribution over the reference period, with strong positive anomalies in areas under the influence of freshwater, i.e., along the Gaspé Peninsula, in Chaleur Bay, and along the western coast of sGSL (Figure 20). Positive phytoplankton biomass anomalies were more widespread during fall (Figure 20), with the second highest anomaly of the times series in wGSL and third highest in eGSL (Figure 22). These large spatial patterns were mirrored by local conditions encountered at the high-frequency monitoring stations, with near-normal nitrate concentrations and high phytoplankton biomass at Rimouski station and in wGSL and low surface nitrate levels and phytoplankton biomass at Shediac Valley station and in sGSL (Figure 8).

Remote sensing of ocean colour

Satellite imagery suggests that the spring phytoplankton bloom started first in early April near Cabot Strait, in late April in sGSL and wGSL, and in early May in the Estuary and most of eGSL (Figures 23, 24). In the Estuary, strong surface chl *a* concentrations were observed until the end of June, matching observations at Rimouski station (Figures 8, 24). Maximum chl *a* concentrations in the surface layer during spring averaged ca. 3 mg chl *a* m^{-3} over the GSL and were close to or below normal (Figure 23). The start of the spring bloom was near normal in the Magdalen Shallows and Cabot Strait boxes, while it was delayed in NEGSL. It also seems that the spring bloom was shorter and weaker in terms of both amplitude and magnitude in all boxes (Figure 26). Calculation of the spring bloom statistics for the NWGSL in 2019 was not performed in reason of low satellite data availability during spring, but samples from Rimouski station suggest an early start and high amplitude of the spring bloom in the Estuary that might well have occurred in NWGSL. Annual anomaly patterns suggest low phytoplankton biomass in the surface layer across the GSL, mostly because the anomalies during spring and fall were strongly negative as well. However, high phytoplankton biomass during spring were expected, at least in the Magdalen Shallows and NEGSL boxes, according to the large nutrient uptake that seemed to occur in these regions during spring (Figure 19). Low surface chl *a* concentrations during fall (Figures 23, 25) also contrast with the high phytoplankton biomass measured during the fall AZMP survey, especially in eGSL (Figures 20, 22). These diverging patterns could be caused by the vertical structure of phytoplankton in the water column. However, during the 2019 fall cruise, most of the phytoplankton biomass was in the upper 25 m of the surface layer in eGSL and was relatively homogenously distributed within this layer (data not shown). The seasonal anomalies derived from satellites are calculated from three month periods while our sampling at sea is generally completed within a few days, so these different timeframes might better explain divergences between in situ and remote sensing data. In addition, bias in remote sensing data during fall due to higher cloud cover as well as the timing of sampling could also account for some of the discrepancies between satellite and field data.

ZOOPLANKTON

High-frequency monitoring stations

In 2019, the zooplankton biomass at Rimouski station followed the seasonal climatology, with above or near-normal values for most of the year (Figure 27a). At Shediac Valley, however, the few zooplankton biomass data collected were generally below normal (Figure 27b). Total copepod abundances followed a pattern similar to biomass, with above-normal abundances at Rimouski station and below or near-normal abundance at Shediac Valley station (Figures 28a, 29a). The copepod assemblage at Rimouski station in 2019 was like the reference period with a higher proportion of *Microcalanus* spp. (Figure 28b, c). At Shediac Valley, the proportion of large calanoids (*C. finmarchicus, C. glacialis, C. hyperboreus*) was also lower in 2019 than during the

reference period (Figure 29b, c). New taxa, *Oithona atlantica* and *Triconia borealis,* also make their arrival among the dominant taxa in 2019 at this station.

Calanus finmarchicus abundances in 2019 at Rimouski station were mostly below the monthly climatology, except for a few samples collected in June and July (Figure 30a). There was a large peak of *C. finmarchicus* early stages (CI–CIII) in May, i.e., slightly earlier than for the reference period, and the peak lasted until mid-July. Beside that, the proportion of each *C. finmarchicus* copepodite stage and their developmental timing were similar to the reference period (Figure 30b, c). The abundance of *C. hyperboreus* was above the climatology most of the year; its stage composition and phenology were similar to the reference period, with the main difference being the decreased contribution of CIV stage that was balanced by a larger contribution of the CV stage (Figure 31). In addition, the stable composition of the population from June onward indicates that most individuals went into diapause at stage CV (Figure 31b, c). It might also indicate a lower contribution of the new generation (CIV) to the overwintering stock, i.e., lower recruitment. This has been observed in the past, even during the 1990s, when environmental conditions were markedly different (Plourde et al. 2003). The seasonal abundance of *Pseudocalanus* spp. at Rimouski station in 2019 mostly reflected the monthly climatology. However, spring abundance was higher than normal, and this was associated with a large contribution of early copepodite stages (Figure 32 a–c). The few zooplankton samples collected at Shediac Valley station suggest relatively near-normal abundances for these three species (Figures 30d, 31d, 32d). The main difference with the climatology is the low abundance of all three species in May, but also in June for *C. hyperboreus*. No stage analysis was carried out for *Pseudocalanus* spp. at Shediac Valley station.

Gulf subregions

As observed at the high-frequency monitoring stations, the average total zooplankton biomasses were above normal in wGSL and below normal in sGSL in 2019 (Figure 33). In fact, the 2019 summer zooplankton biomass in wGSL was the highest of the time series. In eGSL, summer and fall biomasses were close to the climatology. In this region, it is mostly the near-average *C. finmarchicus* abundances that allowed biomass to stay somewhat similar to the times series average, whereas the high abundance of *C. hyperboreus* during summer explained the high zooplankton biomass in wGSL (Figures 34, 35). Abundances of the small calanoid *Pseudocalanus* spp. were still rising in most regions, especially during fall. Indeed, nearly the highest densities of the fall time series were recorded in all regions. However, their summer abundances in eGSL and sGSL were low (Figure 36).

Copepod phenology

Changes in the timing of zooplankton development were described using the detailed seasonal pattern of the relative copepodite stage abundances of *C. finmarchicus* at Rimouski station from 1994 to 2019 (Figure 37). Overall, there is a trend towards earlier population development. The proportion of adults (CVI) was large in May 2019, suggesting an early start of the CV copepodite stage moulting to the adult stage. It thus seems that developmental timing in 2019 followed this general trend. However, development from stage CI to CIII lasted longer, from May to July, whereas it had previously lasted less than a month (Figure 37). There was a second smaller CI–CIII cohort during fall 2019 (Figure 37).

Scorecards

The time series of annual zooplankton biomass anomalies highlights recent major changes in the community, with mostly negative anomalies across the GSL since 2010 (Figure 38). In 2019, positive biomass anomalies were recorded both at Rimouski station and in wGSL, a first since

2007. Negative anomalies persisted elsewhere but were not as strong as the 2016–2017 record lows (Figure 38). A synthesis of standard AZMP zooplankton indices (abundance of *C. finmarchicus*, *Pseudocalanus* spp., total copepods, non-copepods) was performed using annual normalized abundance anomalies and is presented as a scorecard (Figure 39). The near-normal to below-normal anomalies for *C. finmarchicus* in 2019 in all GSL subregions are a continuation of the pattern initiated in 2010. Positive *Pseudocalanus* spp. anomalies also appeared in 2010, and 2019 was no exception, with positive anomalies across the GSL. Total copepod abundance only showed positive anomalies at Rimouski station and in eGSL, while it was close to the average in other subregions. Non-copepod abundance has also been increasing since 2010, and this index showed positive anomalies in eGSL and sGSL in 2019 while it was near normal in wGSL (Figure 39).

The annual normalized abundance anomalies for six additional zooplankton indices (*C. hyperboreus* and five zooplankton groups: small calanoids, large calanoids, cyclopoids, warm-water species, and cold/arctic species) are presented in Figure 40. A detailed list of species included in each of these indices is presented in Appendix 1. *Calanus hyperboreus* abundance was above normal at Rimouski station and slightly below normal in eGSL and sGSL during 2019. Overall since 2009, there has been a decline in large calanoid abundance and an increase in small calanoid abundance (Figure 40). Positive anomalies for small calanoids were again observed in 2019 in all regions except sGSL. Interestingly, large calanoids showed weak positive anomalies at Rimouski station and eGSL, and were near normal in other subregions in 2019. The increases in large calanoid abundance recorded at Rimouski station and eGSL were attributable to *C. hyperboreus* and *C. glacialis* (data not shown), respectively. The increase in small calanoid abundance was mostly attributable to *Pseudocalanus* spp. in wGSL and eGSL, and to *Microcalanus* spp. at Rimouski station (data not shown). Warm-water-associated copepods is another group that has been on the rise since about 2010, and it was true again in 2019 except in sGSL, where its abundance was similar to the climatology. Cold-water-associated copepods have shown increased abundances in eGSL since 2007, including 2019, because the abundance of *C. glacialis* was almost twice as high as the next highest abundance recorded over the time series (data not shown). The high abundances of *C. glacialis* as well as *Metridia longa* also explained a record high anomaly of cold-water-associated copepods at Shediac Valley station (data not shown; N.B., there were only eight samples collected at Shediac Valley). These annual anomalies were relatively coherent among the high-frequency monitoring stations (Rimouski and Shediac Valley stations) and their associated GSL subregions (Figures 38, 39, 40).

DISCUSSION

ENVIRONMENTAL CONDITIONS

The timing of the onset and extent of water column stratification plays a role in defining spring bloom phenology, phytoplankton production, species succession, and trophic interactions over the complete growth season (Levasseur et al. 1984). In 2019, the timing of upper water column stratification was very similar to the climatology, but stratification was stronger during spring and early summer at Rimouski station and during summer at Shediac Valley station. In addition to the effect of water column stratification on phytoplankton dynamics, thermal properties of the surface, intermediate, and deep-water masses play a role in defining zooplankton dynamics (Plourde et al. 2002). Galbraith et al. (2020) reported on the physical conditions that prevailed in the GSL during 2019, showing cold conditions in the surface layer, average temperatures in the CIL, and warm conditions in deep waters. This document reports on the chemical and biological conditions in the GSL in the context of these conditions.

Changes in dissolved oxygen of the deep waters entering the GSL at the continental shelf are related to the varying proportions of Labrador Current water (cold/fresh, high dissolved oxygen levels) and slope water (warm/salty, low dissolved oxygen levels), which together are the source of GSL deep water (McLellan 1957, Lauzier and Trites 1958, Gilbert et al. 2005). These waters travel from the mouth of the Laurentian Channel to the Estuary in roughly three to four years (Gilbert 2004), decreasing in dissolved oxygen as a result of *in situ* respiration and oxidation of organic material as they progress to the channel heads. Based on interdecadal variability, the inflow of warmer waters to the Estuary is expected to exacerbate the hypoxic conditions since these waters are typically poor in dissolved oxygen (McLellan 1957, Lauzier and Trites 1958, Gilbert et al. 2005). In the St. Lawrence Estuary, temperature of the deep water layer is well correlated with deep oxygen concentration over the time series (R^2 = -0.86). At 300 m in the Estuary, water temperature has increased by 1.64°C between the early 1970s and 2019 (Figure 50 in Galbraith et al. 2020). Considering the relationship of oxygen solubility with temperature, this should translate into a decrease in dissolved oxygen of 12.3 µM over the same timeframe, but the decrease has exceeded 50 µM. Moreover, given the inherent properties of GSL source waters (North Atlantic Central Water vs Labrador Current Water; Gilbert et al. 2005), changes in their mixing ratio at Cabot Strait imply that a decrease of 1.46 µM might be expected for each 0.1°C temperature increase. However, dissolved oxygen at 300 m decreased by ca. 65 µM at Cabot Strait over the time series for a 1.7°C increase in temperature (Figure 50 in Galbraith et al. 2020). Thus, warming of bottom water and changes in the mixing ratio of source waters are not the only factors contributing to the decrease in oxygen concentrations in the GSL. Other factors that can cause variability in oxygen concentration include interannual changes in the vertical flux of organic matter to the bottom waters of the Lower St. Lawrence Estuary.

Winter mixing is a critical process for bringing nutrient-rich deep water to the surface. In the GSL, winter convection is partly caused by buoyancy loss of surface waters attributable to cooling and reduced freshwater runoff, brine rejection associated with sea-ice formation, and wind-driven mixing prior to ice formation (Galbraith 2006). Warmer-than-normal surface waters throughout the winter and minimal sea-ice formation imply low winter convection and may reduce the amount of nutrients available for spring primary production. The CIL represents the winter surface mixed layer that has been insulated from the atmosphere by near-surface stratification and whose nutrient inventory will supply primary producers during the growth season through vertical mixing. In 2019, CIL temperature and winter mixed layer volume suggest that winter convection was near or above normal, and nutrient content was indeed relatively high in the surface layer at the onset of the spring bloom but low after it occurred. Nutrient exchange between the CIL and the surface layer might have been limited later during the season because of the strong stratification during spring and summer. Negative nitrate anomalies in the surface layer have been regularly encountered in the GSL since 2010, a period over which several temperature and ice-cover indices have shown clear warming of the GSL (Galbraith et al. 2020). The sum of regional annual anomalies suggests a significant nitrate decrease of about 5 mmol m^{-2} yr^{-1} (i.e., a decrease of between 1 and 5% per year depending on the regional climatology) in the surface layer over the time series. Riverine nutrient input to the GSL might be another factor to consider to improve our understanding of nutrient dynamics and interannual variability, at least in areas of significant freshwater inputs.

Positive anomalies in deep-water (300 m) nutrients have been observed since 2012 in eGSL in association with high temperature and salinity water intrusions into the GSL from Cabot Strait (Galbraith et al. 2020). These higher-than-average deep inventories may be associated with a water mass composition that has a greater contribution of slope water than Labrador Shelf water, intensifying the effect of a shallower thermocline that reduces exchanges between the upper and bottom layers (Galbraith et al. 2020 and references therein). In contrast, negative deep-water nitrate anomalies were observed at Rimouski station for a fourth consecutive year,

and possibly elsewhere in the Estuary. These could be the result of changes in nitrogen cycle due to microbial activity, such as decreased nitrification associated with low oxygen concentrations. The routine measurement of NH_4 concentrations has recently been added to AZMP sampling in the GSL and will eventually be helpful in verifying this latter hypothesis. Moreover, the ongoing modeling of processes involved in the nitrogen cycle in the GSL (Diane Lavoie, DFO, Mont-Joli, QC) will allow a detailed understanding of key processes involved in nitrate distribution.

The N:P ratio is another index that requires further attention since variability in the stoichiometry of the nutrient supply is a key determinant of oceanic nutrient limitation (Arrigo 2005). Thus, changes in the CIL N:P ratio over time may be a better predictor of changes in the phytoplankton community and productivity than nitrate concentrations themselves. For example, if the negative anomalies in the N:P ratio observed since 2017 in eGSL were to persist through time, they might entail a change in the productivity of this region.

PHYTOPLANKTON

Except at Rimouski station, where sampling regularly covers the spring bloom period, phytoplankton production during the spring bloom must be inferred either from indirect indices, such as the difference in the nutrient inventory of the surface mixed layer between the winter and the summer surveys, or from satellite observations. Interestingly, the nutrient drawdown associated with spring production in 2019 was among the most intense observed over the times series in eGSL and sGSL, contrasting with bloom metrics that generally suggest a short and relatively weak spring bloom. Overall, field samples suggest high annual phytoplankton biomass, mostly associated with the strong positive fall anomalies. These annual positive chl a anomalies have been regularly observed since 2013 in sGSL and eGSL. These increases of chl a over the years are significant in these two regions ($p = 0.03$ and $p < 0.001$, respectively), and may suggest that either environmental conditions are good for the growth of phytoplankton biomass, or that reduced grazing pressure favours the accumulation of phytoplankton biomass during fall. The diminution of nitrate inventories in the surface layer over the time series as well as recent observations at Shediac Valley indicate a possible phytoplankton community shift towards smaller-sized cells, which are known to perform better in nutrient-poor and stratified waters (Levasseur et al. 1984, Li and Harrison 2008). This suggests that changes in both grazing pressure and grazer community composition are more likely to explain the high chl a concentrations rather than ideal growth conditions. The AZMP program has not regularly documented the taxonomic composition of the phytoplankton community elsewhere in the GSL, and we must be cautious when generalizing these results to other GSL subregions. Moreover, the effect of survey timing on the annual averages cannot be ignored despite the use of a GLM approach to analyse the data that reduces spatio-temporal bias. High annual chl a concentrations may well be explained by earlier sampling during fall in recent years.

In contrast with field data, ocean colour observations suggested low phytoplankton biomass in the surface layer, especially during spring and fall. Such negative anomalies have been frequently encountered since the use of VIIRS satellite data began in 2012. These negative anomalies suggest a decrease of 5 to 15% of surface chl a since 2012, depending on the statistical box. It is possible that the VIIRS satellite performs better in coastal waters in terms of minimizing the overestimation of chl a concentration in turbid waters compared to previous satellites. If so, this could partly explain why most satellite-derived chl a anomalies have been negative since data from this satellite have been used. Improved algorithms for the retrieval of chl a in the Gulf of St. Lawrence from the SeaWIFS satellite have recently been published (Laliberté et al. 2018) and should eventually be incorporated into our statistical boxes, which could modify the time series anomaly pattern. However, as far as the spring bloom metrics are

concerned, the change of satellite platforms over the time series does not seem to lead to any questionable trends over time. There are no apparent trends over the time series for any of these indices, except perhaps for the duration and magnitude of the spring bloom. Indeed, it seems that the occurrence of strong positive anomalies has increased since 2010, suggesting that spring bloom productivity—and how it may fulfill its role in terms of the food web's main energy source—has become much more variable in the last decade. In addition, 2010, 2012, and 2016–2018 show the strongest anomalies of the times series regarding early bloom timing. These changes could be associated with the combined effects of warming on the onset of stratification and the reduced densities of overwintering copepods (low annual biomass) during these years (Sommer and Lengfellner 2008).

ZOOPLANKTON

There was heterogeneity in zooplankton biomass anomalies over the GSL in 2019. Positive anomalies were recorded at Rimouski station and in wGSL—a first in the past five years—because of the high abundance of *C. hyperboreus* throughout the year at Rimouski station and during spring in wGSL, but negative anomalies were encountered in other GSL subregions. Zooplankton biomass had generally shown below-normal values in recent years, with record lows in 2016–2017. There is a significant ($p < 0.0001$) biomass decrease of ca. 0.18 g m^{-2} yr^{-1} over the monitoring period for the GSL (i.e. this corresponds to a general diminution of 1.5 to 4% per year depending on the regional climatology). Lower biomass is typically associated with a decrease in the abundance of large-sized zooplankton species. The mean weight of large-sized calanoids (e.g., *C. hyperboreus*: 3.5 mg per adult female) is between one and two orders of magnitude greater than that of small-sized calanoids (e.g., *Pseudocalanus* spp.: 0.02 mg per adult female) [Conover and Huntley 1991, Plourde et al. 2003]. Thus, the decrease in large calanoid abundance has a greater impact on zooplankton biomass than, for instance, the increase of *Pseudocalanus* spp. abundance that was recorded in all GSL subregions in 2019. The increase in small calanoids seems to be coupled with the increase in non-copepod abundance, mostly larvae of benthic organisms. Suitability of environmental conditions, competition for food, and/or differential predation pressure might favour the dominance of either one of these communities, i.e., one dominated by large calanoids versus one dominated by a combination of small calanoids and non-copepod (Hall et al. 1976; Daewel et al. 2014), with potential implications for the pelagic food web and pelago–benthic coupling.

Life cycle strategies vary among large copepod species, and the timing of reproduction relative to the freshet—considering its influence on water-mass circulation and transport—could explain dissimilarities in the distribution patterns of these species (Runge et al. 1999) in subregions that are under the influence of freshwater (i.e. wGSL and sGSL). The subregion eGSL is less influenced by freshwater; environmental conditions modifying the zooplankton community there might instead include the volume and temperature of cold and saline Labrador Shelf water that flows into eGSL through the Strait of Belle Isle, which have both shown negative anomalies in recent years, except in 2019 (Cyr et al. 2020; Figure 35 in Galbraith et al. 2020). The differences in these environmental drivers might explain why eGSL often shows distinct anomaly patterns for the zooplankton assemblage, notably that it is the only region where cold-water-associated copepods have shown positive anomalies over the past 10 years, including in 2019, when this index reached its maximum. However, in 2019, eGSL generally followed the main trends observed since about 2010, i.e., positive anomalies for *Pseudocalanus* spp., small calanoids, non-copepods, and warm-water-associated copepods, as was seen in other subregions.

Questions that may arise from these clear changes in zooplankton community composition and size structure could concern the underlying explanatory drivers and what is to be expected in a

near future. While the role of predation and of changing predator stocks in the observed trends has yet to be determined, it is possible to get a few insights regarding the effect of environmental variables using a simple correlation matrix (Figure 41). This matrix shows that, over the time series, phytoplankton biomass is better correlated with nitrate levels in the mid-layer rather than in the surface layers. Even though the correlations are generally not significant, temperature seems to act as an important driver in defining the phytoplankton phenology and zooplankton community. Warm conditions in the mid layer favour early bloom start, and warmer temperature in the deep layer are ideal for warm-water-associated copepods and non-copepods. Nitrate levels in the surface layer also seems to shape zooplankton community, favouring large-sized zooplankton taxa, possibly through its effect on bloom timing. These environmental factors may also trigger changes in the developmental timing of zooplankton taxa (not illustrated on the figure), such as the earlier development of *C. finmarchicus* at Rimouski station in recent years. A regional correlation matrix could highlight some of these linkages or reveal new ones. Overall, zooplankton communities in the GSL seem to be shaped by a combination of changing water-mass properties and of bottom-up controls, although the relative importance of these processes is not yet well understood.

SUMMARY

This document reports on the chemical and biological (plankton) conditions in the GSL in 2019 in the context of a strong warming event initiated in 2010. Data from 2019 are compared to time-series observations.

- Concentrations of dissolved oxygen at 300 m reached record lows in 2019 in the Estuary and were the second or third (NW GSL) lowest of the time series in other regions, being slightly above the 2018 record lows.
- Surface nitrate inventories (0–50 m) were near or below the climatology in all GSL subregions. Positive deep-water (300 m) nutrient anomalies have been frequently observed since 2012 in eGSL and are associated with intrusions of high temperature/high salinity water into the GSL through Cabot Strait.
- In situ nutrients and chl a data suggest high phytoplankton biomass during 2019, especially during fall, while ocean colour data suggest below-normal phytoplankton biomass in the surface layer during spring and fall.
- According to satellite imagery, the duration, magnitude, and amplitude of the spring bloom were below normal in all regions in 2019. Data did not allow the calculation of bloom metrics in NWGSL, but samples from Rimouski station suggest an early start and high amplitude of the spring bloom in the Estuary.
- The phytoplankton community was similar to the climatology community at Rimouski station, but diatom abundance was above normal most of the year and the abundance of dinoflagellates has declined since 2014. At Shediac Valley, the few samples collected in 2019 suggest a decrease in the abundance of diatoms concomitant with an increase of small-sized cells, also since 2014.
- Zooplankton biomass was above normal at Rimouski station and in wGSL because of high *C. hyperboreus* abundances. In wGSL, the spring zooplankton biomass recorded in 2019 was the highest of the time series. Biomass was below normal elsewhere in the GSL.
- Positive anomalies of small calanoids, non-copepods, and warm-water-associated copepods were once again recorded in 2019 although they were not as widespread as in previous years. These trends have generally been observed since 2010. It is also worth noting that the abundance of cold-water-associated copepods was above normal in eGSL for the sixth consecutive year, and that a record high of their abundance was observed at Shediac Valley station.
- The emergence from diapause for *C. finmarchicus* at Rimouski station was on time and the peak of early copepodite stages (CI–III) lasted until mid-July. There was a second small CI–III cohort in fall 2019.

ACKNOWLEDGEMENTS

We thank Jean-Yves Couture, Marie-France Beaulieu, Caroline Lebel, Isabelle St-Pierre, and Caroline Lafleur for preparation and standardization of the phytoplankton and zooplankton data. The data used in this report would not be available without the work of François Villeneuve and his AZMP team (Rémi Desmarais, Marie-Lyne Dubé, Yves Gagnon, Line McLaughlin, Roger Pigeon, Michel Rousseau, Félix St-Pierre, Liliane St-Amand, Sonia Michaud, David Leblanc, and Caroline Lafleur) in organizing and carrying out AZMP surveys and analyzing samples. We thank Jeff Spry and Kevin Pauley for providing data from the Shediac Valley station and BIO's remote sensing unit for the composite satellite images. We are grateful to Emmanuel Devred and David Bélanger for their critical reviews.

REFERENCES CITED

Arrigo, K. R. 2005. Marine microorganisms and global nutrient cycles. Nature. 437:349–355.

Arun Kumar, S.V.V., Babu, K.N., and Shukla, A.K. 2015. Comparative analysis of chlorophyll-a distribution from SeaWiFS, MODIS-Aqua, MODIS-Terra and MERIS in the Arabian Sea. Mar. Geod. 38: 40–57.

Barnes, B., and Hu, C. 2016. Dependence of satellite ocean color data products on viewing angles: A comparison between SeaWiFS, MODIS, and VIIRS. Remote Sens. Environ. 175: 120–129.

Brickman, D., and Petrie, B. 2003. Nitrate, silicate and phosphate atlas for the Gulf of St. Lawrence. Can. Tech. Rep. Hydrogr. Ocean Sci. 231: xi + 152 pp.

Conover, R. J., and Huntley, M. 1991. Copepods in ice-covered seas - Distribution, adaptations to seasonally limited food, metabolism, growth patterns and life cycle strategies in polar seas. J. Mar. Syst. 2: 1–41.

Cyr, F., Colbourne, E., Galbraith, P.S., Gibb, O., Snook, S., Bishop, C., Chen, N., Han, G., and D. Senciall. 2020. Physical Oceanographic Conditions on the Newfoundland and Labrador Shelf during 2018. DFO Can. Sci. Advis. Sec. Res. Doc. 2020/018 iv + 48 p.

Daewel, U., Hjøllo, S.S., Huret, M., Ji, R., Maar, M., Niiranen, S., Travers-Trolet, M., Peck, M.A., and van de Wolfshaar, K. E. 2014. Predation control of zooplankton dynamics: a review of observations and models. ICES J. Mar. Sci. 71(2): 254–271.

DFO. 2020. Oceanographic conditions in the Atlantic zone in 2019. DFO Can. Sci. Advis. Sec. Sci. Advis. Rep. 2020/028.

Galbraith, P. S. 2006. Winter water masses in the Gulf of St. Lawrence. J. Geophys. Res. 111, C06022, doi: 10.1029/2005JC003159.

Galbraith, P. S., Desmarais, R., Pigeon, R., and Cantin, S. 2006. Ten years of monitoring winter water masses in the Gulf of St. Lawrence by helicopter. AZMP Bulletin PMZA 5: 32–35.

Galbraith, P.S., Chassé, J., Shaw, J.-L., Dumas, J., Caverhill, C., Lefaivre, D. and Lafleur, C. 2020. Physical oceanographic conditions in the Gulf of St. Lawrence during 2019. DFO Can. Sci. Advis. Sec. Res. Doc. 2020/030. iv + 84 p.

Gilbert, D. 2004. Propagation of temperature signals from the northwest Atlantic continental shelf edge into the Laurentian Channel. ICES CM, 2004/N: 7, 12 pp.

Gilbert, D., Sundby, B., Gobeil, C., Mucci, A., and Tremblay, G.-H. 2005. A seventy-two-year record of diminishing deep-water oxygen in the St. Lawrence estuary: The Northwest Atlantic connection. Limnol. Oceanogr., 50(5): 1654–1666.

Gregg, W. W., and Rousseaux, C. S. 2014. Decadal trends in global pelagic ocean chlorophyll: A new assessment integrating multiple satellites, in situ data, and models. J. Geophys. Res. Oceans, 119: 5921–5933, doi 10.1002/2014JC010158.

Hall, D.J., Threlkeld, S.T., Burns, C.W., and Crowley, P.H. 1976. The size-efficiency hypothesis and the size structure of zooplankton communities. Annu. Rev. Ecol. Evol. Syst. 7: 177–208.

Johnson, C., Casault, B., Head, E., and Spry, J. 2016. Optical, chemical, and biological oceanographic conditions on the Scotian Shelf and in the Eastern Gulf of Maine in 2014. DFO Can. Sci. Advis. Sec. Res. Doc. 2016/003. v + 51 p.

Laliberté, J., Larouche, P., Devred, E., and Craig, S. 2018. Chlorophyll-a concentration retrieval in the optically complex waters of the St. Lawrence Estuary and Gulf using principal component analysis. Remote Sens. 10, 265, doi: 10.3390/rs10020265.

Lauzier, L.M., and Trites, R.W. 1958. The deep waters of the Laurentian Channel. J. Fish. Res. Board Can. 15: 1247–1257.

Levasseur, M., Therriault, J.-C., and Legendre, L. 1984. Hierarchical control of phytoplankton succession by physical factors. Mar. Ecol. Prog. Ser. 19: 211–222.

Li, W. K. W., and Harrison, W. G. 2008. Propagation of an atmospheric climate signal to phytoplankton in a small marine basin. Limnol. Oceanogr. 53(5): 1734–1745.

McLellan, H.J. 1957. On the distinctness and origin of the slope water off the Scotian Shelf and its easterly flow south of the Grand Banks. J. Fish. Res. Board Can. 14: 213–239.

Mitchell, M. R., Harrison, G., Pauley, K., Gagné, A., Maillet, G., and Strain, P. 2002. Atlantic Zonal Monitoring Program sampling protocol. Can. Tech. Rep. Hydrogr. Ocean Sci. 223: iv + 23 pp.

Parent, G.J., Plourde, S., and Turgeon, J. 2011. Overlapping size ranges of *Calanus* spp. off the Canadian Arctic and Atlantic coasts: impact on species' abundances. J. Plankton Res. 33: 1654–1665.

Pepin, P., Maillet, G., Fraser, S., Shears, T., and Redmond, G. 2013. Optical, chemical, and biological oceanographic conditions on the Newfoundland and Labrador Shelf during 2011-12. DFO Can. Sci. Advis. Sec. Res. Doc. 2013/051. v + 38 p.

Plante, S., Chabot, D., and Dutil, J.-D. 1998. Hypoxia tolerance in Atlantic cod. J. Fish Biol. 53: 1342–1356.

Plourde, S., Dodson, J. J., Runge, J. A., and Therriault, J.-C. 2002. Spatial and temporal variations in copepod community structure in the lower St. Lawrence Estuary, Canada. Mar. Ecol. Prog. Ser. 230: 221–224.

Plourde, S., Joly, P., Runge, J.A., Dodson, J., and Zakardjian B. 2003. Life cycle of *Calanus hyperboreus* in the lower St. Lawrence Estuary and its relationship to local environmental conditions. Mar. Ecol. Prog. Ser. 255: 219-233.

Plourde, S., Maps, F., and Joly, P. 2009. Mortality and survival in early stages control recruitment in *Calanus finmarchicus*. J. Plankton Res. 31(4): 371–388.

Runge, J. A., Castonguay, M., de Lafontaine, Y., Ringuette, M., and Beaulieu, J. L. 1999. Covariation of climate, zooplankton biomass and mackerel recruitment in the southern Gulf of St. Lawrence. Fish. Oceanogr. 8(2): 139–149.

Sommer, U., and Lengfellner, K. 2008. Climate change and the timing, magnitude, and composition of the phytoplankton spring bloom. Global Change Biol. 14: 1199–1208.

Therriault, J.-C., Petrie, B., Pépin, P., Gagnon, J., Gregory, D., Helbig, J., Herman, A., Lefaivre, D., Mitchell, M., Pelchat, B., Runge, J., and Sameoto, D. 1998. Proposal for a Northwest Atlantic zonal monitoring program. Can. Tech. Rep. Hydrogr. Ocean Sci. 194: vii + 57 pp.

Wang, M., Liu, X., Tan, L., Jiang, L., Son, S. H., Shi, W., Rausch, K., and Voss, K. 2013. Impacts of VIIRS SDR performance on ocean color products. J. Geophys. Res. Atmos. 118: 10,347–10,360, doi:10.1002/jgrd.50793.

Zhai, L., Platt, T., Tang, C., Sathyendranath, S., and Hernández Walls, R. 2011. Phytoplankton phenology on the Scotian Shelf. ICES J. Mar. Sci. 68: 781–791, doi:10.1093/icesjms/fsq175.

Zibordi, G., Mélin, F., and Berthon, J.-F. 2006. Comparison of SeaWiFS, MODIS and MERIS radiometric products at a coastal site. Geophys. Res. Letters 33: L06617, doi:10.1029/2006GL0257.

TABLES

Table 1. List of AZMP surveys with locations, dates, and sampling activities for 2019. wGSL, eGSL, and sGSL denote the western, eastern, and southern subregions of the Gulf of St. Lawrence. See Figure 1 for station locations.

	Name	**Location**	**Dates (2019)**	**Vessel**	**CTD/bottle**	**Net**
High-frequency monitoring stations	*Rimouski*	*48°40.0'N 068°35.0'W*	*26 Feb – 6 Dec*	*Beluga II (+ others)*	*38*	*33*
	Shediac Valley	*47°46.8'N 064°01.8'W*	*3 Mar – 23 Oct*	*Multiple*	*9*	*8*
Winter Survey	*-*	*Estuary and Gulf*	*4 – 13 March*	*GC-945 Helicopter*	*103*	*0*
Summer Survey	*TESL*	*wGSL*	*24 May – 16 Jun*	*Teleost*	*7*	*7*
	TSI	*wGSL*	*24 May – 16 Jun*	*Teleost*	*6*	*6*
	TASO	*wGSL*	*24 May – 16 Jun*	*Teleost*	*5*	*5*
	TIDM	*sGSL*	*24 May – 16 Jun*	*Teleost*	*10*	*10*
	TDC	*eGSL*	*24 May – 16 Jun*	*Teleost*	*6*	*6*
	TCEN	*eGSL*	*24 May – 16 Jun*	*Teleost*	*5*	*5*
	TBB	*eGSL*	*24 May – 16 Jun*	*Teleost*	*7*	*7*
	Supplementary		*24 May – 16 Jun*	*Teleost*	*23*	*11*
Total					*69*	*57*
Fall Survey	*TESL*	*wGSL*	*21 Oct – 18 Nov*	*Coriolis II*	*7*	*7*
	TSI	*wGSL*	*21 Oct – 18 Nov*	*Coriolis II*	*6*	*6*
	TASO	*wGSL*	*21 Oct – 18 Nov*	*Coriolis II*	*5*	*5*
	TIDM	*sGSL*	*21 Oct – 18 Nov*	*Coriolis II*	*10*	*10*
	TDC	*eGSL*	*21 Oct – 18 Nov*	*Coriolis II*	*6*	*6*
	TCEN	*eGSL*	*21 Oct – 18 Nov*	*Coriolis II*	*5*	*5*
	TBB	*eGSL*	*21 Oct – 18 Nov*	*Coriolis II*	*7*	*7*
	Supplementary		*21 Oct – 18 Nov*	*Coriolis II*	*31*	*0*
Total					*77*	*46*

FIGURES

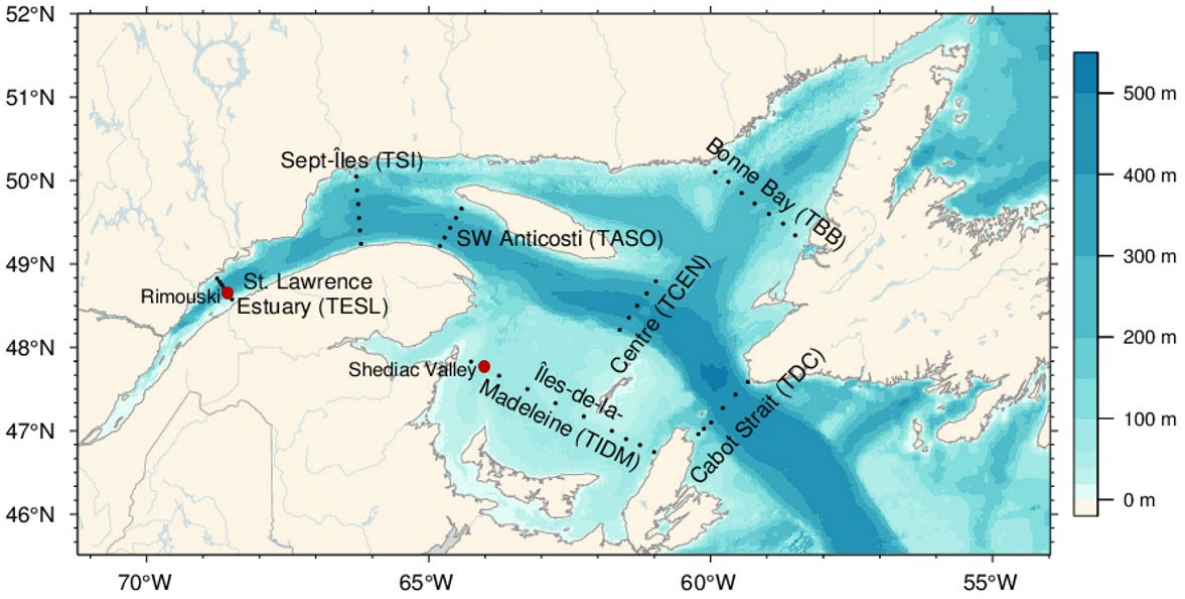

Figure 1. Bathymetric map of the Estuary and Gulf of St. Lawrence showing regular core AZMP sampling stations on the different sections (dots) and at Rimouski and Shediac Valley stations (red circles).

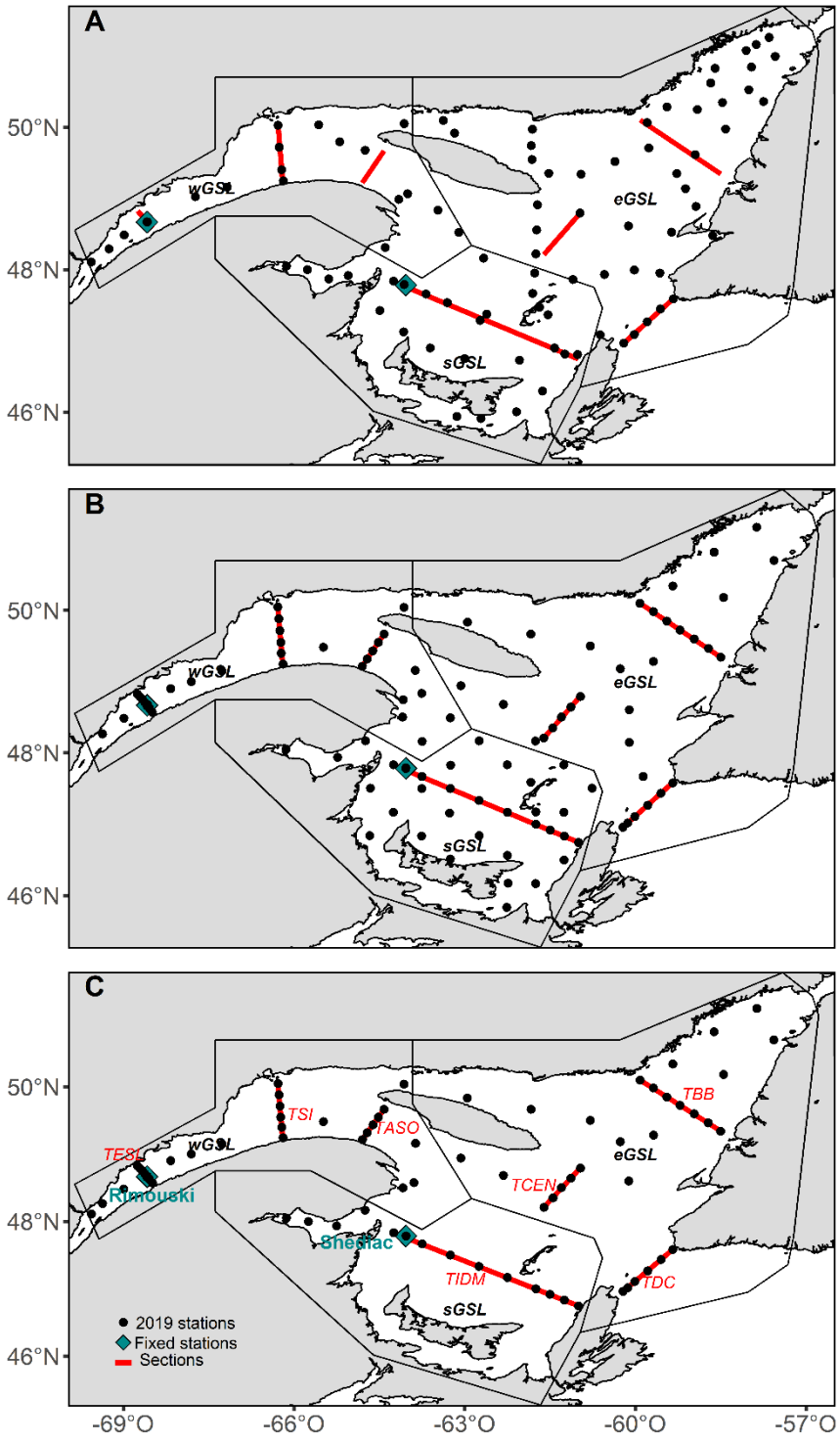

Figure 2. Locations of stations sampled during winter (A), summer (B), and fall (C) 2019. Sections are grouped to form subregions within the western GSL (TESL, TSI, TASO), southern GSL (TIDM), and eastern GSL (TBB, TCEN, TDC).

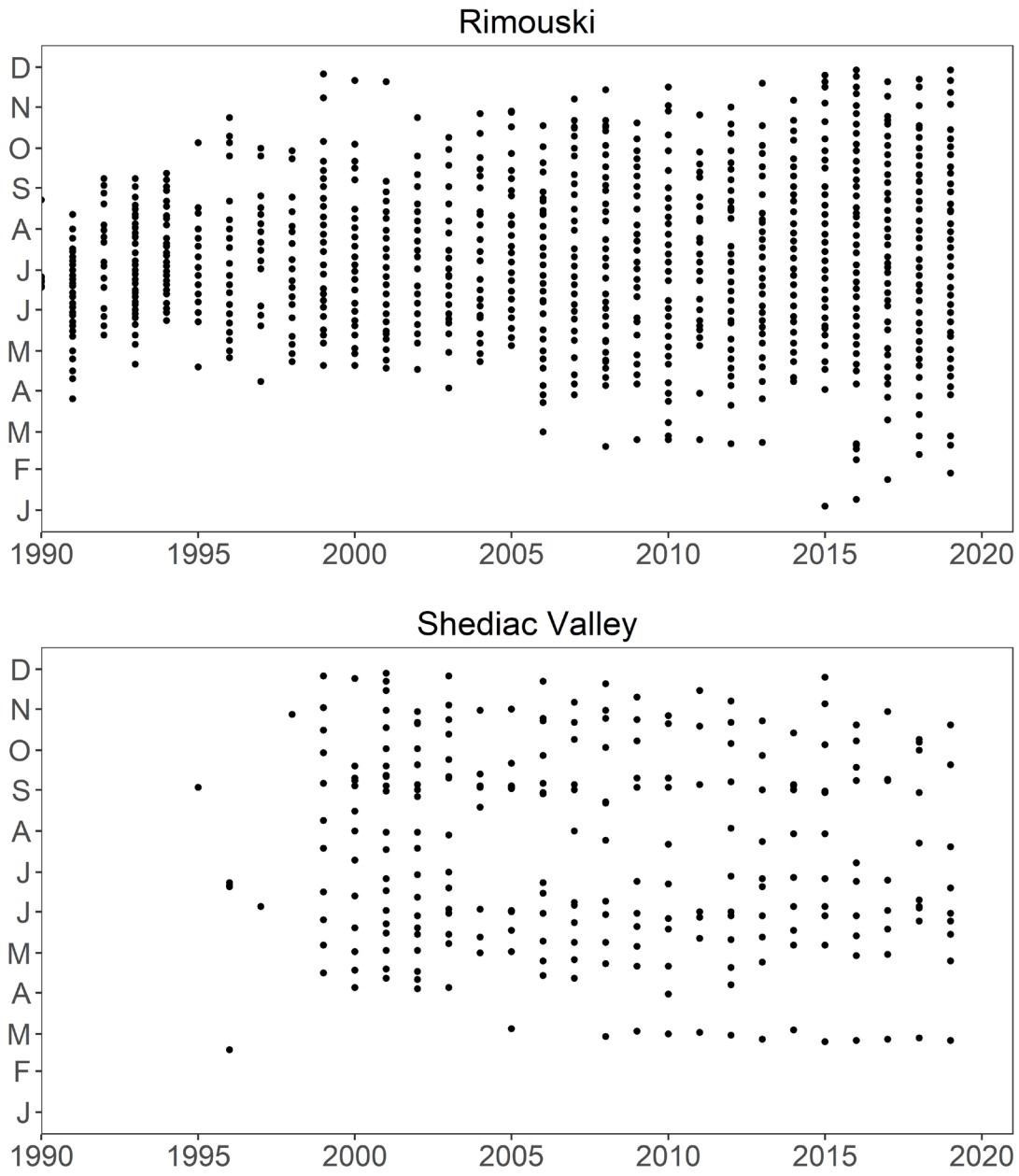

Figure 3. Sampling frequencies at Rimouski and Shediac Valley stations through 2019. Sampling included CTD/bottle as well as plankton net tows most of the time (weather permitting).

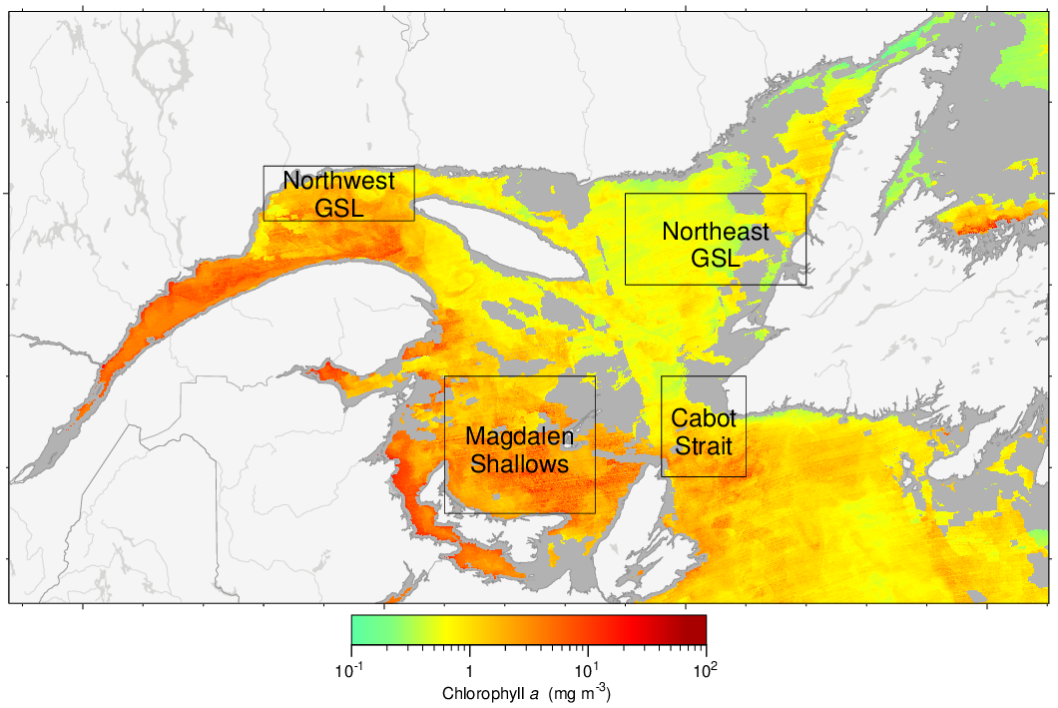

Figure 4. Statistical boxes in the GSL identified for the spatial/temporal analysis of satellite ocean colour data. The figure is a VIIRS composite image showing chlorophyll a from 16–30 April 2019. Grey areas indicate no data (near-shore regions in this case).

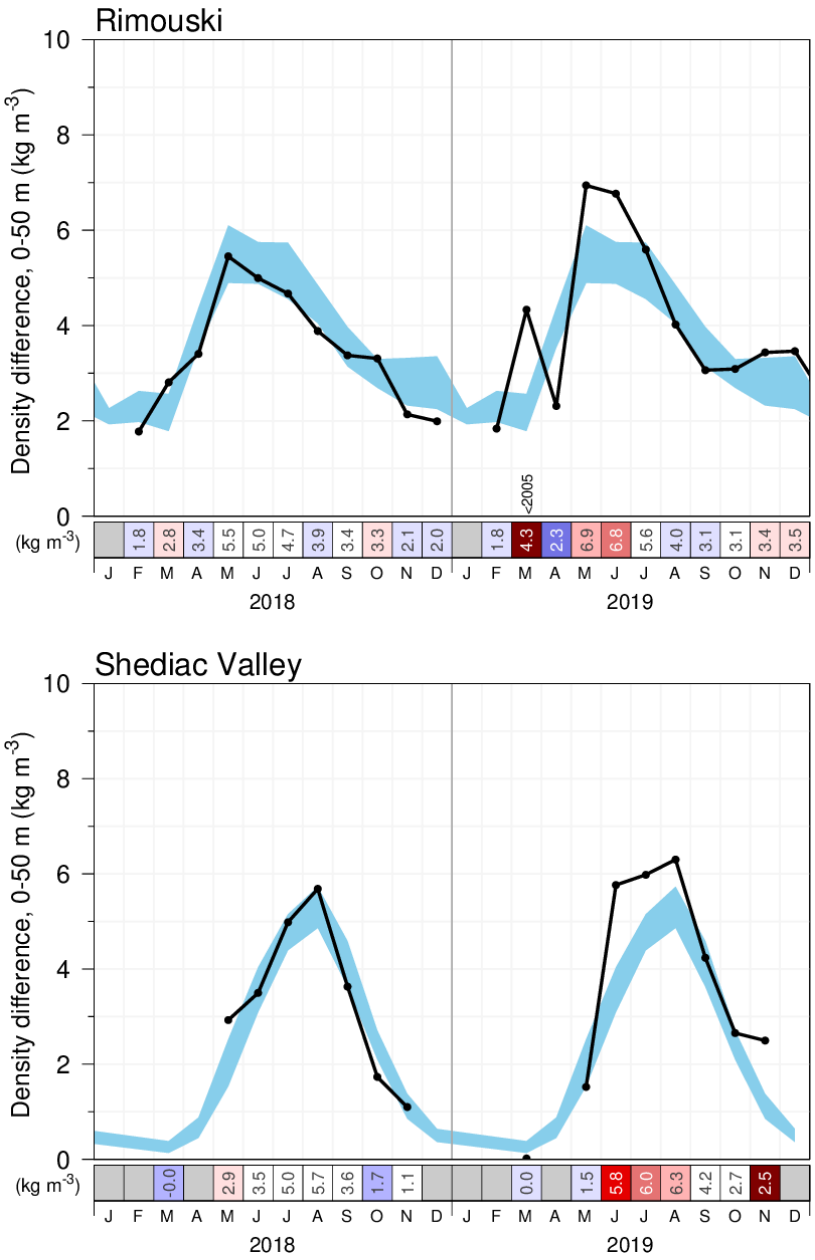

Figure 5. Seasonal stratification index (calculated as the density difference between 50 m and the surface; black solid line) during 2018 and 2019 at Rimouski station (upper panel) and at Shediac Valley station (lower panel). The blue area represents the climatological monthly mean ± 0.5 SD (1991–2015 for Rimouski and 1981–2015 for Shediac Valley). The positive anomalies are shown in red and correspond to low salinity and strong stratification. Numbers in the scorecard are the monthly density differences in kg m^{-3}. For anomalies greater than 2 SD, the prior year with a greater anomaly is indicated.

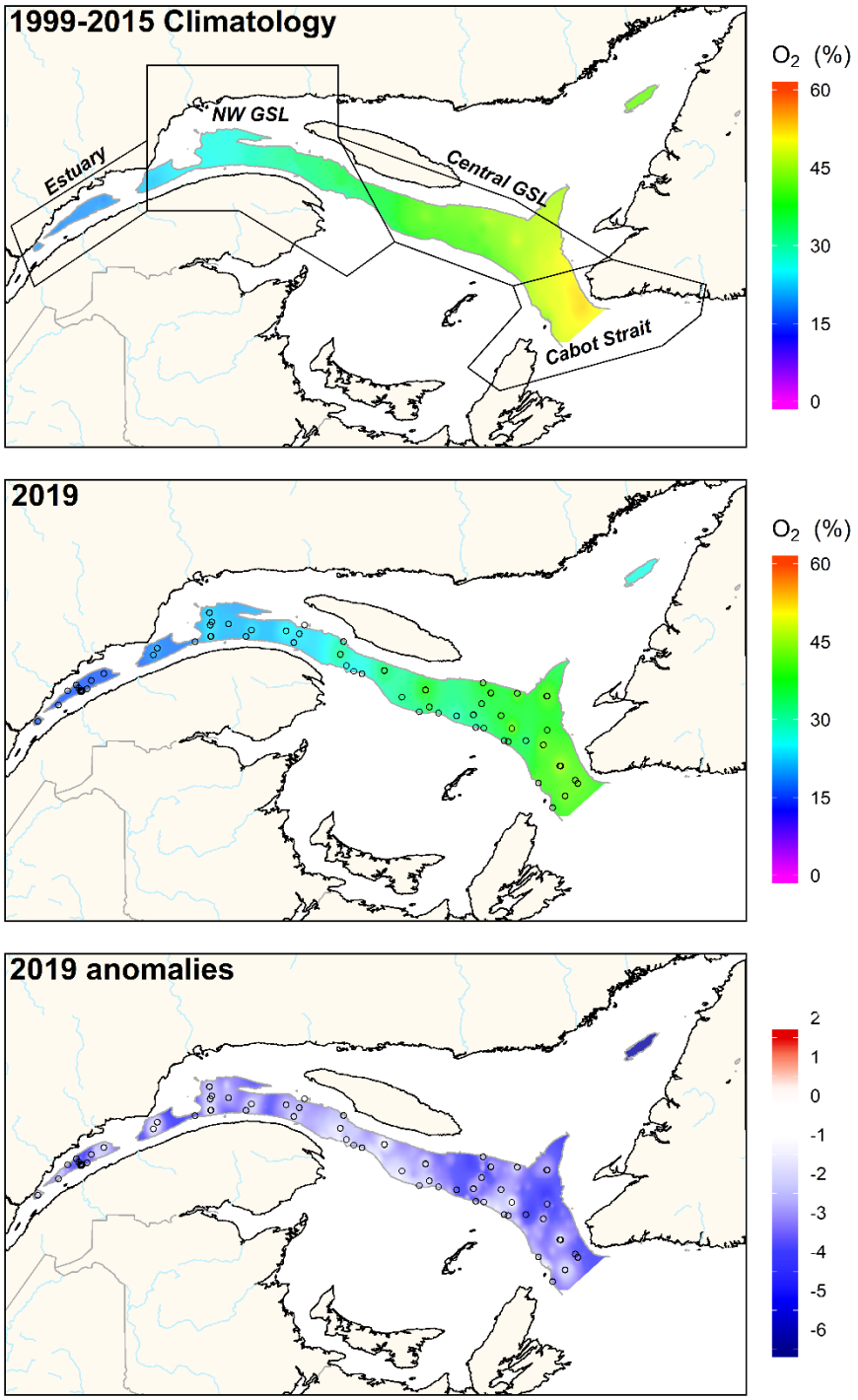

Figure 6. Annual average distribution of dissolved oxygen saturation at a depth of 300 m in the Estuary and Gulf of St. Lawrence during 2019 (upper panel). The climatology (1999–2015; middle panel) and anomalies (lower panel) are also shown. Blue colours indicate anomalies below the mean, reds are anomalies above the mean, and white represents normal conditions. Polygons in the upper panel are used to calculate regional anomalies. Open circles represent station locations in 2019.

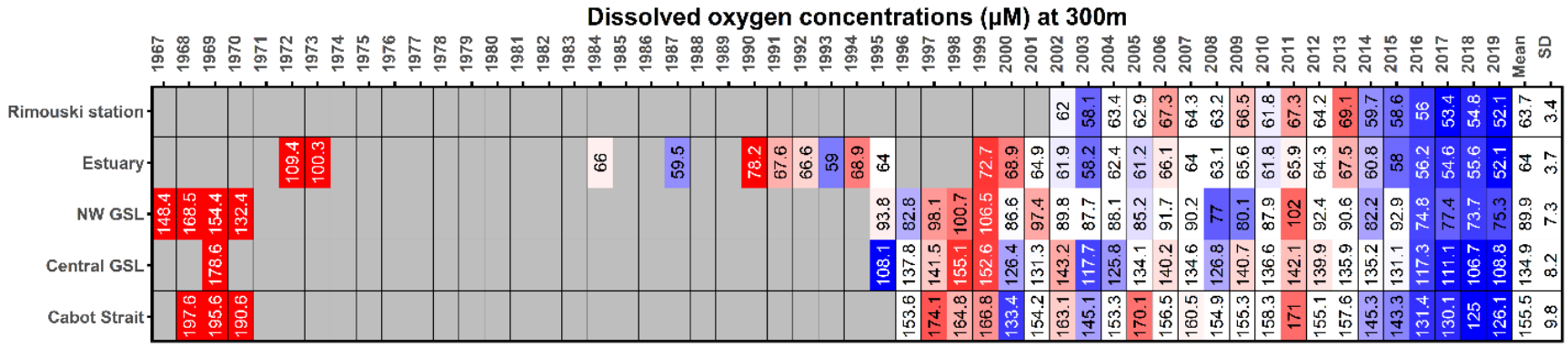

Figure 7. Time series of deep-layer dissolved oxygen concentration (µM). This figure uses the subregions presented in Figure 6. The oxygen time series presented in Gilbert et al. (2005) for the Estuary is included in our Estuary dataset. The numbers on the right are the 1999–2015 climatological means and standard deviations, and the numbers in the boxes are the oxygen concentrations. Cell colour represents the anomaly: blue colours indicate anomalies below the mean, reds are anomalies above the mean, and white represents normal conditions.

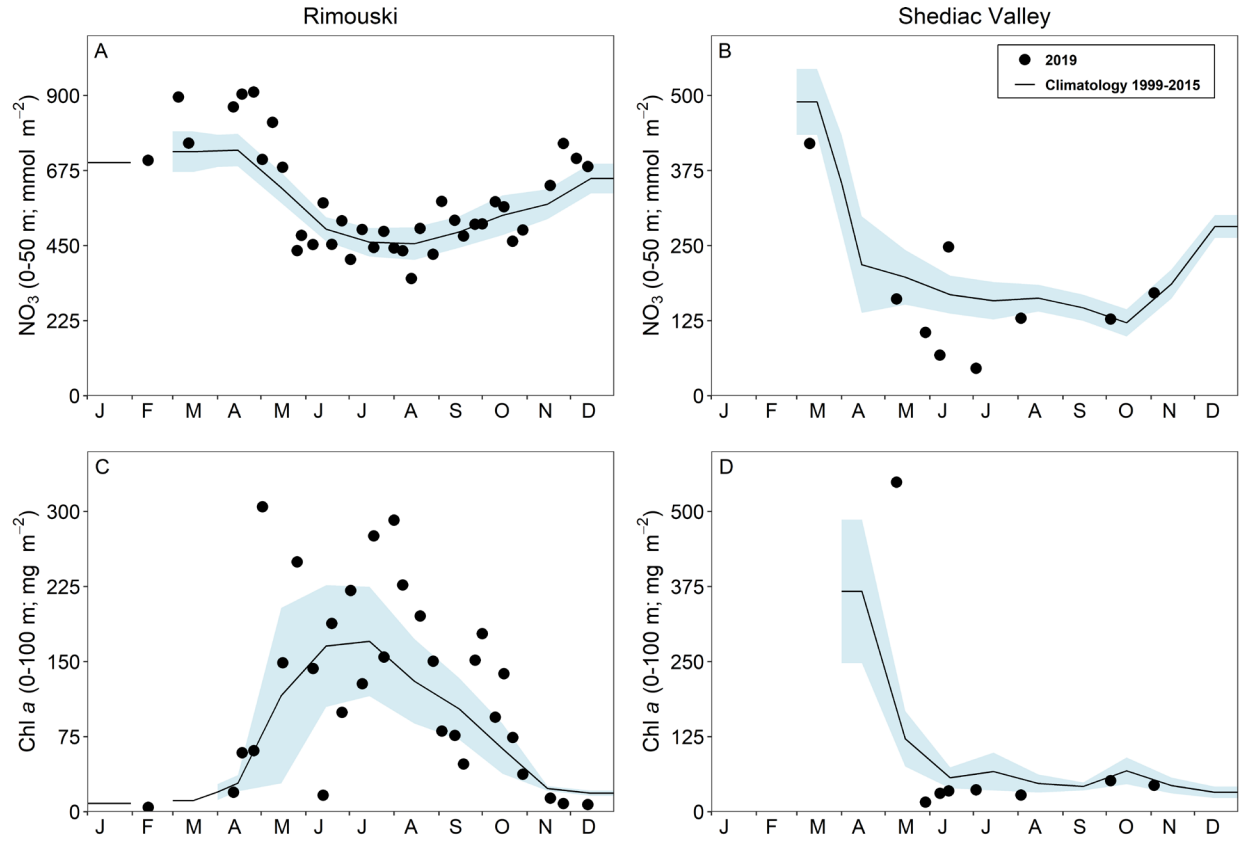

Rimouski

	1999	2000	2001	2002	2003	2004	2005	2006	2007	2008	2009	2010	2011	2012	2013	2014	2015	2016	2017	2018	2019	Mean	SD
Chl *a* 0-100m	2.25	-0.65	0.71	-0.13	0.75	-1.37	-0.89	-0.83	0.61	-1.92	-0.18	0.01	0.03	0.47	-0.37	1.24	0.27	0.67	-0.28	0.45	0.81	34.2	19
NO_3 0-50m	-0.34	0.96	0.39	1.69	-0.41	1.24	-0.33	0	-0.5	0.77	-1.61	-2.14	-0.85	-0.58	0.37	0.69	0.66	-1.31	0.2	-1.19	0.39	590.4	78.4
NO_3 50-150m	-1.37	-0.43	1.03	1.4	-0.65	-0.15	-0.38	1.17	1.37	-0.39	0.16	-1.76	-1.29	0.23	-0.68	1.07	0.67	0.4	-0.29	-2.12	1.47	1430.9	101
NO_3 150-320m	2.49	-1.06	0.24	0.28	-0.06	-0.14	1.01	1.22	0.24	-1.37	-0.06	-1.68	-0.77	-0.46	-0.48	0.41	0.2	-0.97	-1.11	-1.36	-0.18	3883.7	142.5

Shediac Valley

	1999	2000	2001	2002	2003	2004	2005	2006	2007	2008	2009	2010	2011	2012	2013	2014	2015	2016	2017	2018	2019	Mean	SD
Chl *a* 0-100m	-1.03	-1.39	-0.14	2.36	0.16	-0.38	-0.69	-0.05	1.49	1.43	-0.06	-0.69	-1.16	0.34	0.54	-0.32	-0.39	-0.92	1.23	-0.59	-0.41	50.2	16.5
NO_3 0-50m	0.71	1.58	-0.1	0.52	0.59	0.75	-0.88	0.6	-2.02	-0.14	1.05	-1.97	-1.17	-0.02	0.09	0.46	-0.06	-0.23	0.82	-1.35	-0.86	176.5	44
NO_3 50-84m	0.35	1.81	0.62	-0.35	0.6	-0.03	-0.71	1.48	-1.37	0.3	-0.33	-2.17	-1.21	-0.22	0.13	0.8	0.27	-0.16	0.05	-0.17	0.73	255	39.1
	1999	2000	2001	2002	2003	2004	2005	2006	2007	2008	2009	2010	2011	2012	2013	2014	2015	2016	2017	2018	2019	Mean	SD

Figure 8. Nitrate inventories (0–50 m; top panels) and phytoplankton biomass (0–100 m Rimouski and 0–84 m Shediac Valley; bottom panels) in 2019 (black circles) with monthly mean conditions (± 0.5 SD) for the 1999–2015 reference period (black line with blue shading) at Rimouski and Shediac Valley stations. Time series of normalized annual anomalies for nitrate inventories (mmol m^{-2}) and phytoplankton biomass (mg chl a m^{-2}) are also presented with the variable means and standard deviations for the 1999–2015 reference period to the right of the scorecard. Blue colours indicate anomalies below the mean, reds are anomalies above the mean, and white represents normal conditions.

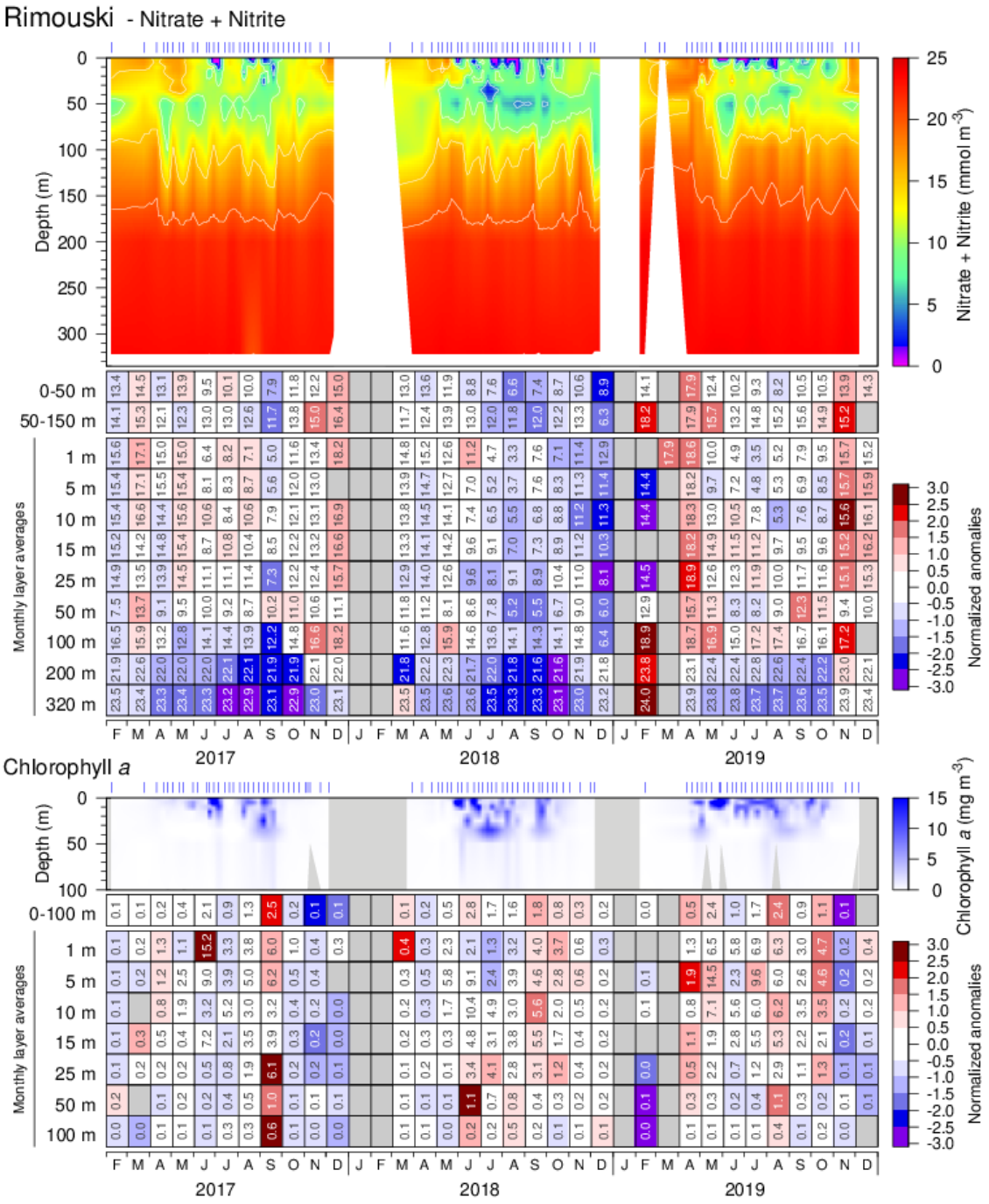

Figure 9. Nitrate (top) and chlorophyll a (bottom) concentrations at Rimouski station during the 2017 to 2019 sampling seasons. Contour plots use data from individual sorties while monthly means are shown in the tables below the graphics (nitrates: mmol m^{-3}; chl a: mg m^{-3}). Cell colours indicate normalized anomalies based on the 1991–2015 climatology: blue colours indicate anomalies below the mean, reds are anomalies above the mean, and white represents normal conditions. During March, the integrated (0–50) monthly average and the depth-specific average for nitrate for the reference period do not include the same amount of data, and this might result in inconsistent anomalies between integrated and depth-specific values.

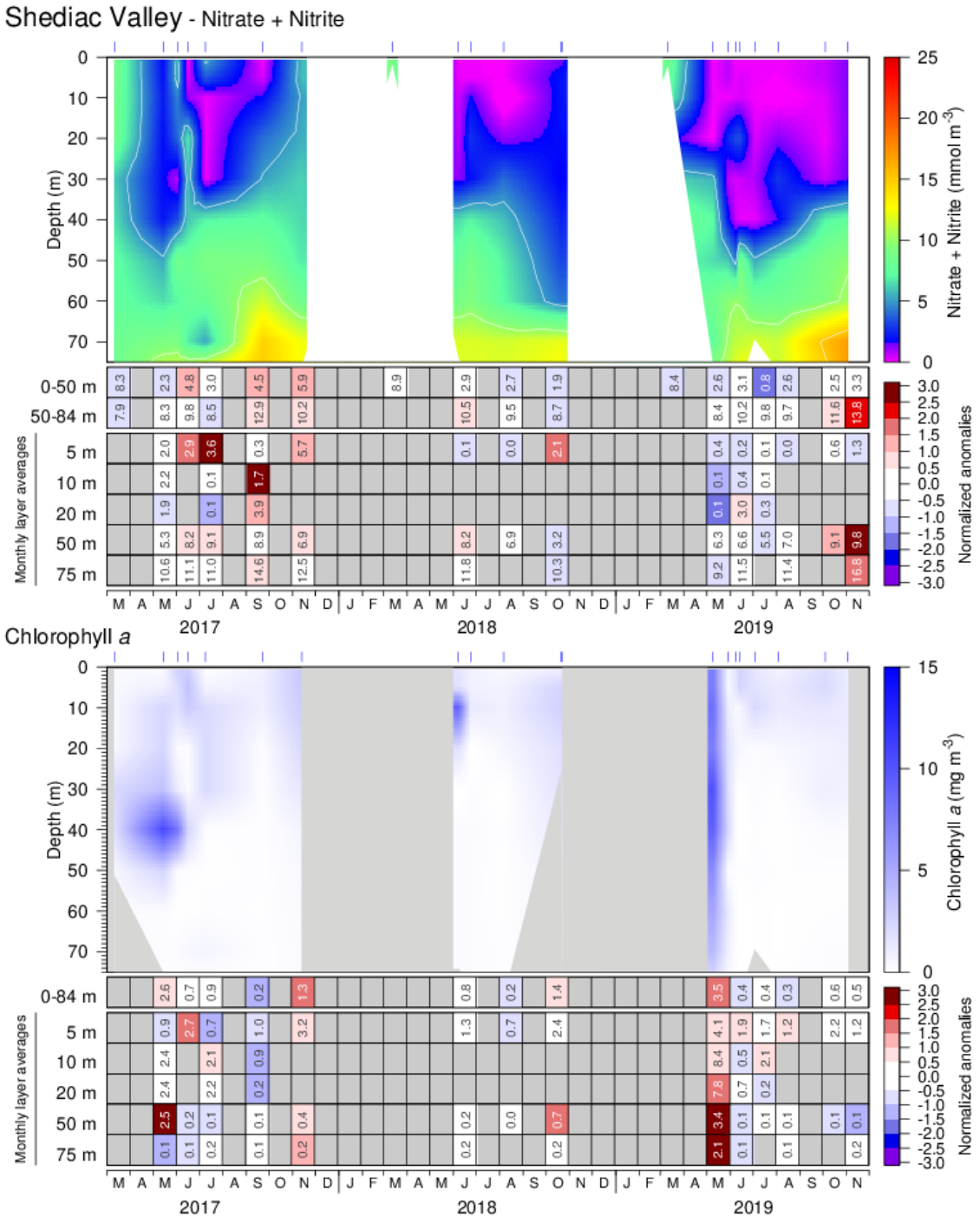

Figure 10. Nitrate (top) and chlorophyll a (bottom) concentrations at Shediac Valley station during the 2017 to 2019 sampling seasons. Contour plots use data from individual sorties while monthly means are shown in the tables below the graphics (nitrates: mmol m^{-3}; chl a: mg m^{-3}). Nitrate values in March are from the winter survey across the Gulf. Cell colours indicate normalized anomalies based on the 1991–2015 climatology: blue colours indicate anomalies below the mean, reds are anomalies above the mean, and white represents normal conditions. Only seven to ten observations per year were used to produce annual vertical profiles, so interpolation between sampling date (blue tick marks above vertical profiles) might not be accurate.

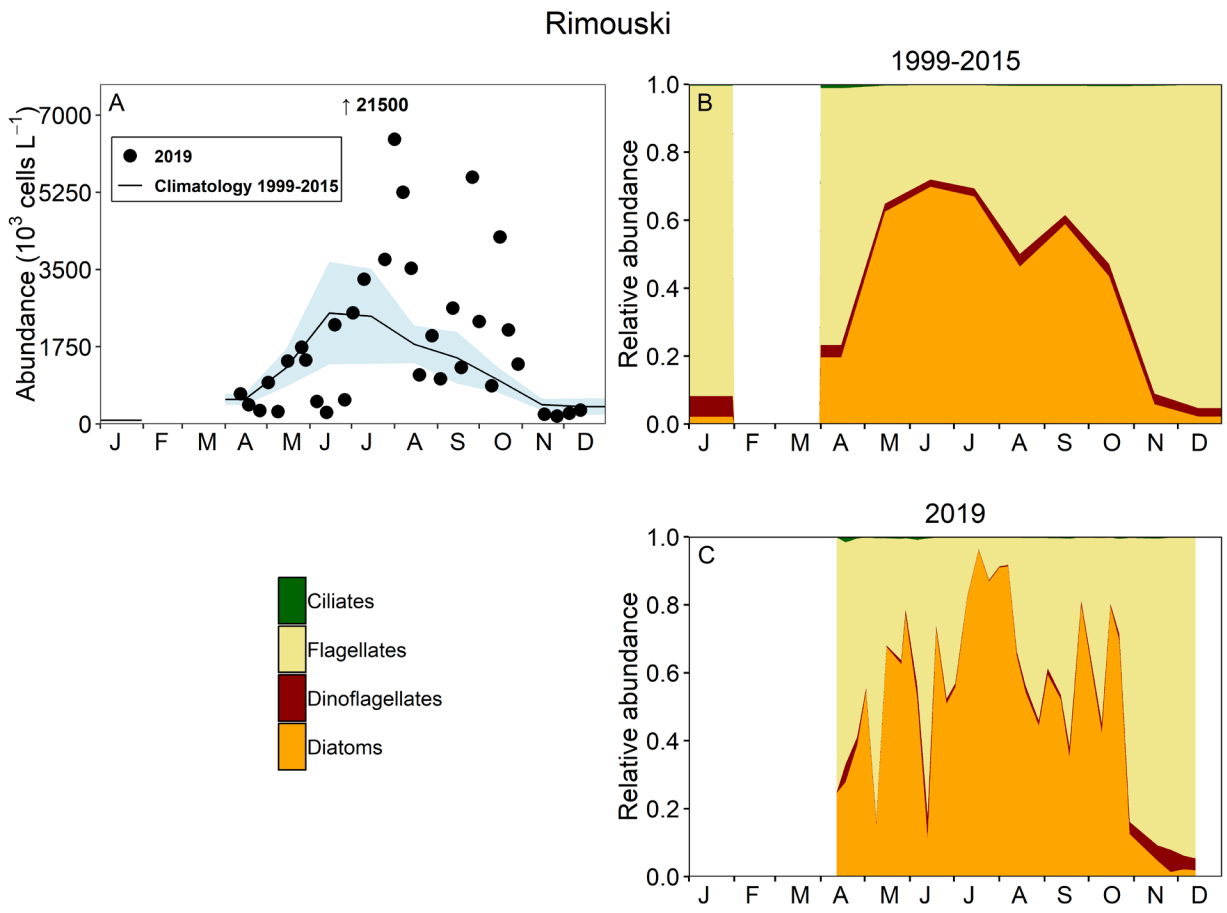

Figure 11. Phytoplankton abundance (A) and community composition at Rimouski station for the 1999–2015 reference period (B; no data in 2010) and for 2019 (C). Blue shading on panel (A) represents ± 0.5 SD of the monthly mean phytoplankton abundance for the reference period. On panel A, an abundance of 21 500 000 cells L^{-1} is indicated with the arrow since it is out of the graphic's range.

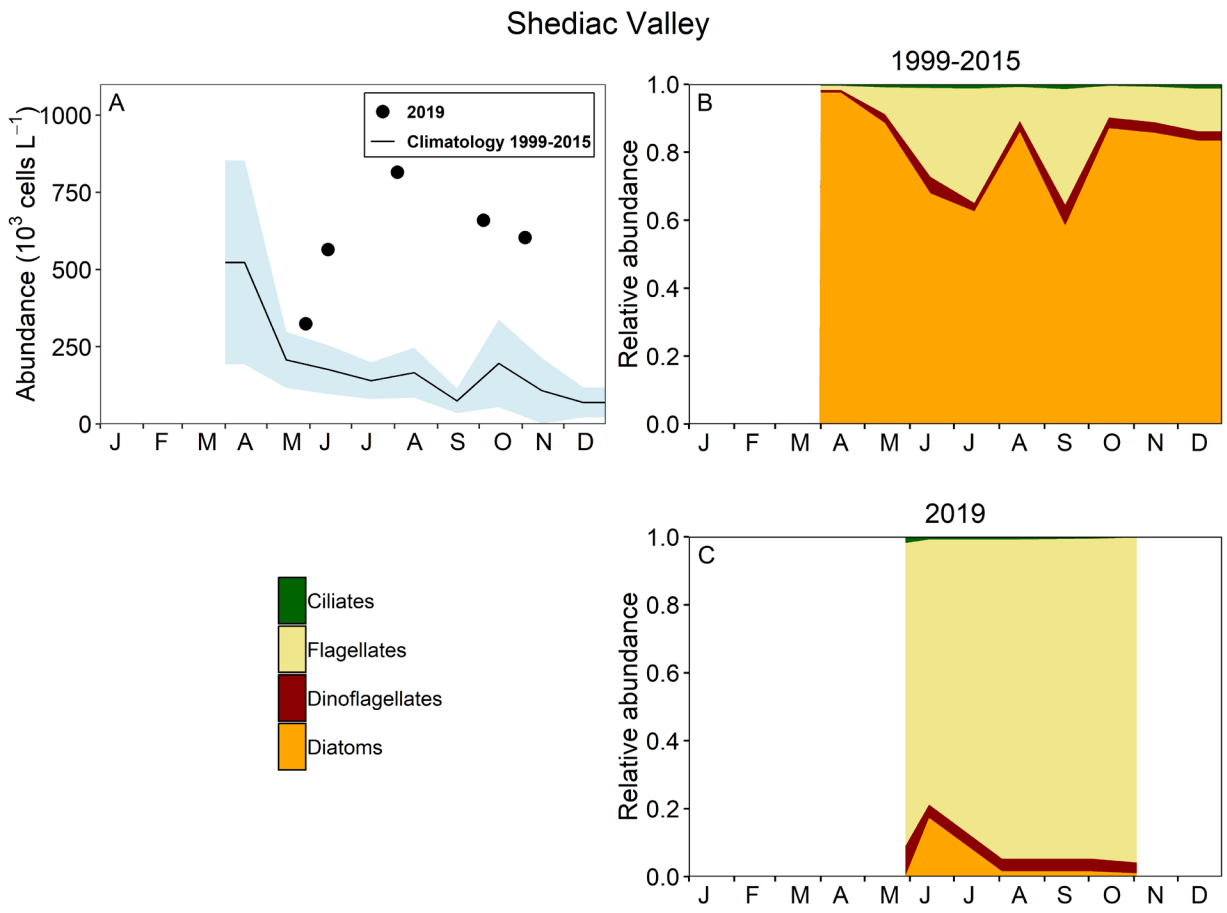

Figure 12. Phytoplankton abundance (A) and community composition at Shediac Valley station for the 1999–2015 reference period (B) and for 2019 (C). Blue shading on panel (A) represents ± 0.5 SD of the monthly mean phytoplankton abundance for the reference period.

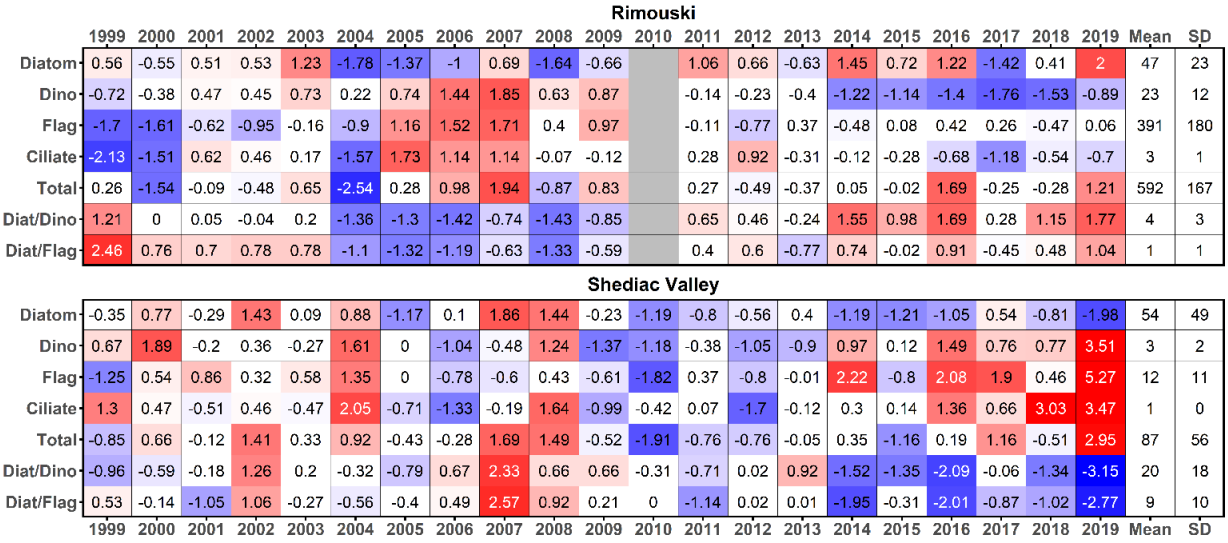

Figure 13. Time series of normalized annual (April–December) anomalies for abundance (10^3 cells L^{-1}) of the main phytoplankton taxonomic groups (diatoms, dinoflagellates, flagellates, ciliates) and total microphytoplankton, and for the diatom/dinoflagellate and diatom/flagellate ratios at Rimouski and Shediac Valley stations. Variable means and standard deviations for the1999–2015 reference period are shown to the right of the scorecard. Blue colours indicate anomalies below the mean, reds are anomalies above the mean, and white represents normal conditions. No data are available for 2010 at Rimouski station.

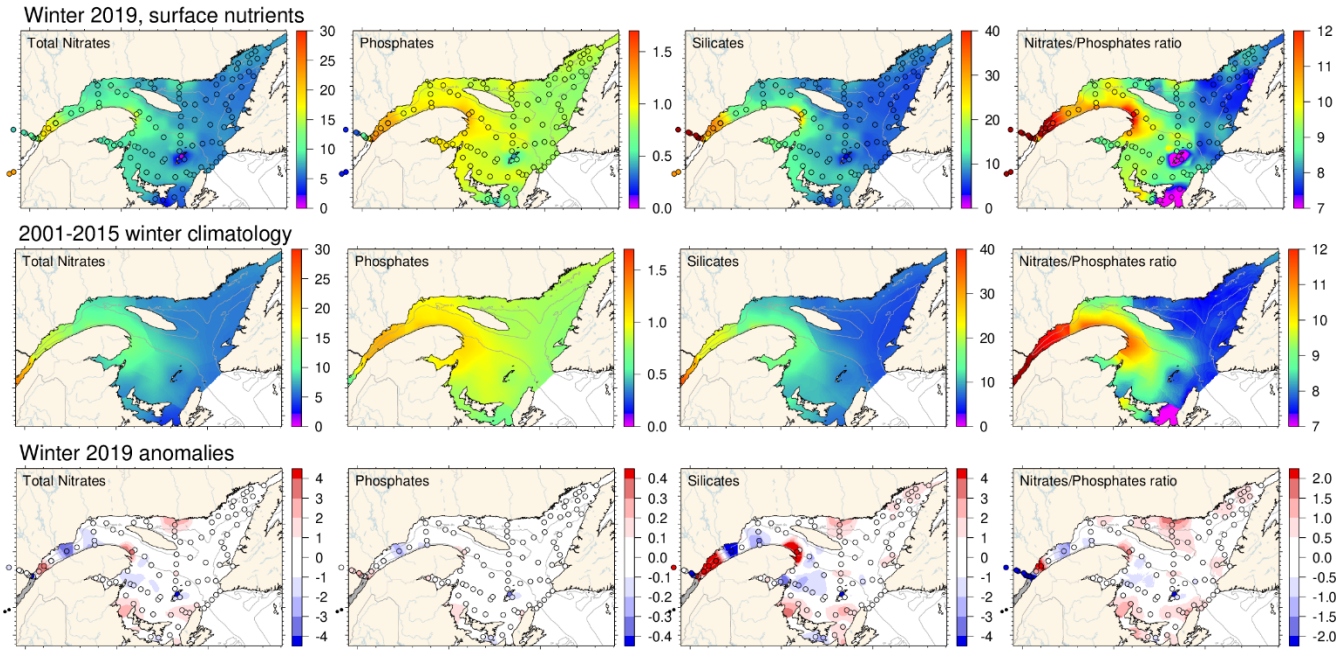

Figure 14. Total nitrate (NO_3^- + NO_2^-), phosphate, and silicate concentrations (mmol m^{-3}) and N:P ratio near the surface in the Estuary and Gulf of St. Lawrence during early March 2019 (upper panels). The climatology (2001–2015; middle panels) and anomalies (lower panels) are shown for each nutrient. Blue colours indicate anomalies below the mean, reds are anomalies above the mean, and white represents normal conditions.

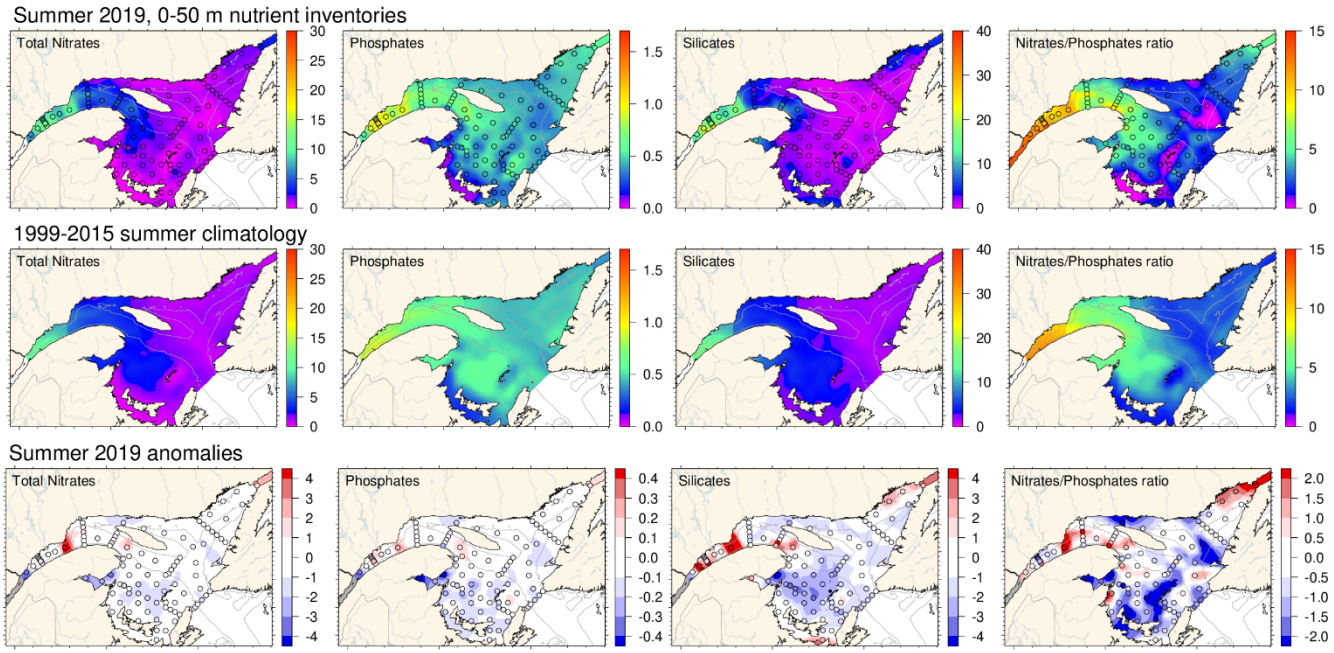

Figure 15. Total nitrate (NO_3^- + NO_2^-), phosphate, and silicate concentrations (mmol m^{-3}) and N:P ratio averaged in the surface layer (0–50 m) in the Estuary and Gulf of St. Lawrence during June 2019 (upper panels). The climatology (1999–2015; middle panels) and anomalies (lower panels) are shown for each nutrient. Blue colours indicate anomalies below the mean, reds are anomalies above the mean, and white represents normal conditions.

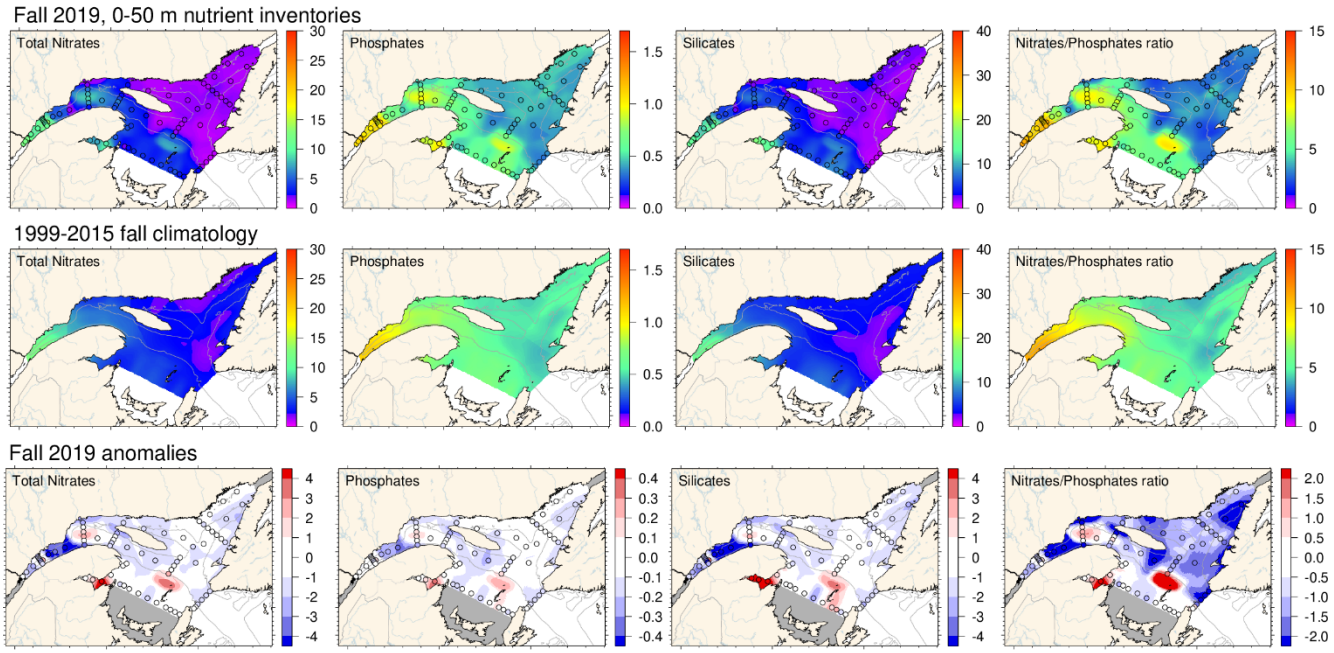

Figure 16. Total nitrate (NO_3^- + NO_2^-), phosphate, and silicate concentrations (mmol m^{-3}) and N:P ratio averaged in the surface layer (0–50 m) in the Estuary and Gulf of St. Lawrence during fall 2019 (upper panels). The climatology (1999–2015; middle panels) and anomalies (lower panels) are shown for each nutrient. Blue colours indicate anomalies below the mean, reds are anomalies above the mean, and white represents normal conditions.

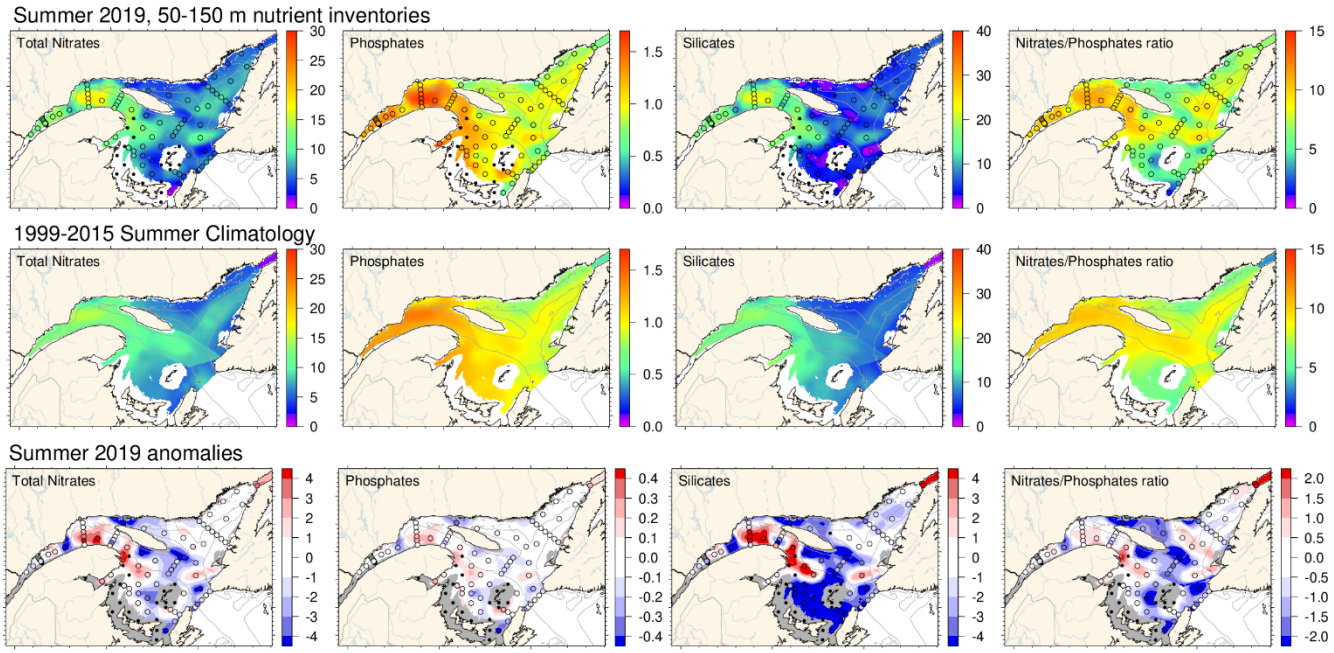

Figure 17. Total nitrate (NO_3^- + NO_2^-), phosphate, and silicate concentrations (mmol m^{-3}) and N:P ratio averaged over the mid-layer (50–150 m) in the Estuary and Gulf of St. Lawrence during June 2019 (upper panels). The climatology (1999–2015; middle panels) and anomalies (lower panels) are shown for each nutrient. Blue colours indicate anomalies below the mean, reds are anomalies above the mean, and white represents normal conditions.

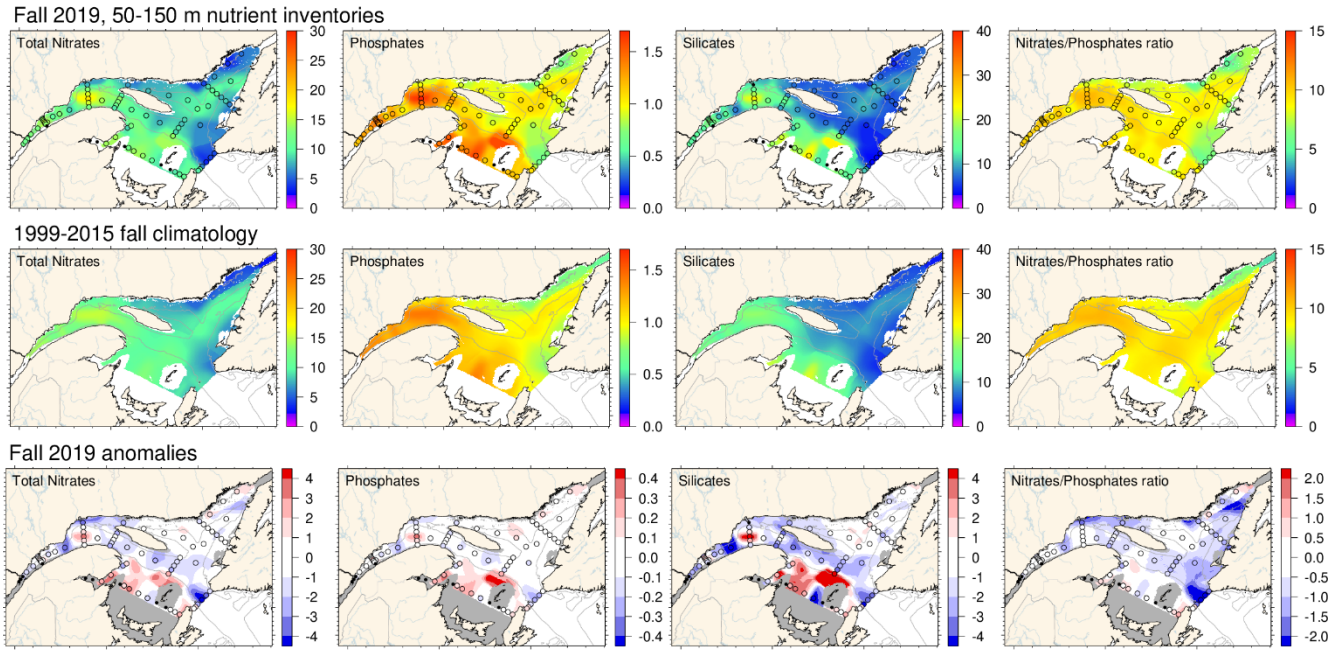

Figure 18. Total nitrate (NO_3^- + NO_2^-), phosphate, and silicate concentrations (mmol m^{-3}) and N:P ratio averaged over the mid-layer (50–150 m) in the Estuary and Gulf of St. Lawrence during fall 2019 (upper panels). The climatology (1999–2015; middle panels) and anomalies (lower panels) are shown for each nutrient. Blue colours indicate anomalies below the mean, reds are anomalies above the mean, and white represents normal conditions.

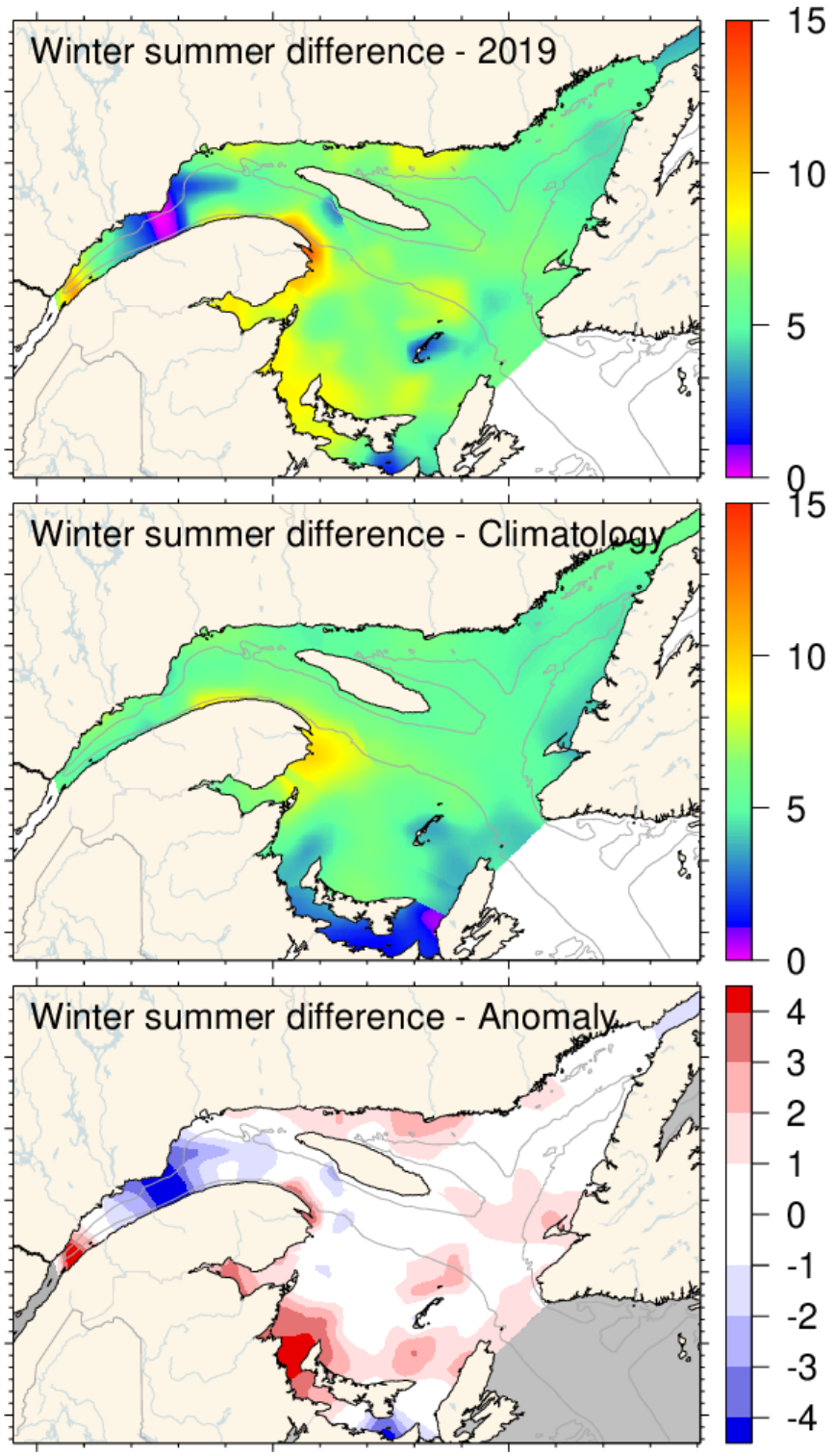

Figure 19. Difference in total nitrate (NO_3^- + NO_2^-) concentrations (mmol m^{-3}) at 2 m in the Estuary and Gulf of St. Lawrence between winter and summer. Top: winter–summer difference in 2019; middle: winter–summer climatology difference (2001–2015); bottom: winter–summer anomaly difference in 2019. Negative anomalies (blue) suggest weak nitrate drawdowns and positive anomalies (red) suggest strong nitrate drawdowns.

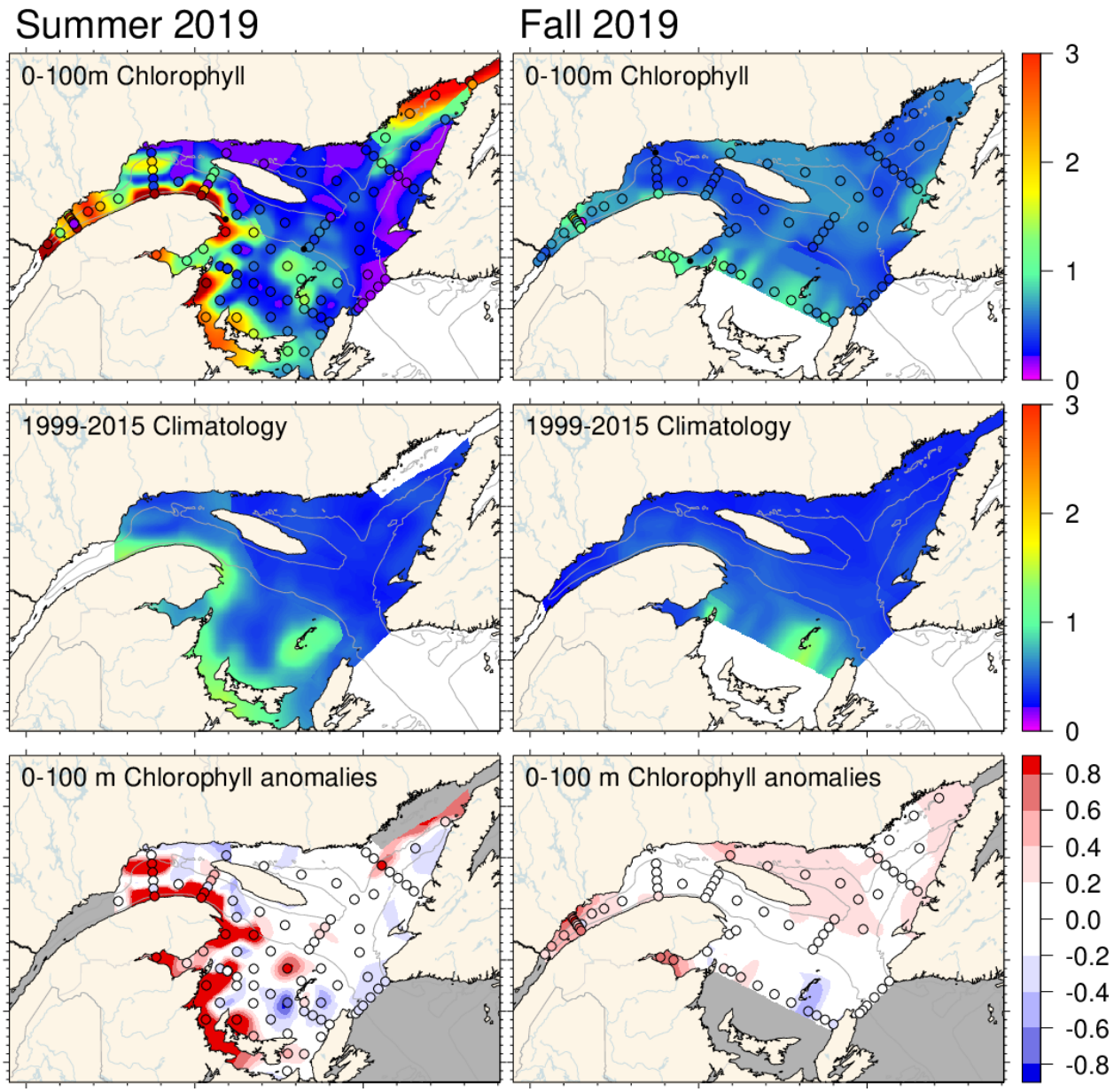

Figure 20. Vertically averaged (0–100 m) chlorophyll a concentrations (mg m^{-3}) in the Estuary and Gulf of St. Lawrence during summer (left panels) and fall (right panels) 2019. The climatology (1999–2015; middle panels) and anomalies (lower panels) are shown for both periods. Blue colours indicate anomalies below the mean, reds are anomalies above the mean, and white represents normal conditions.

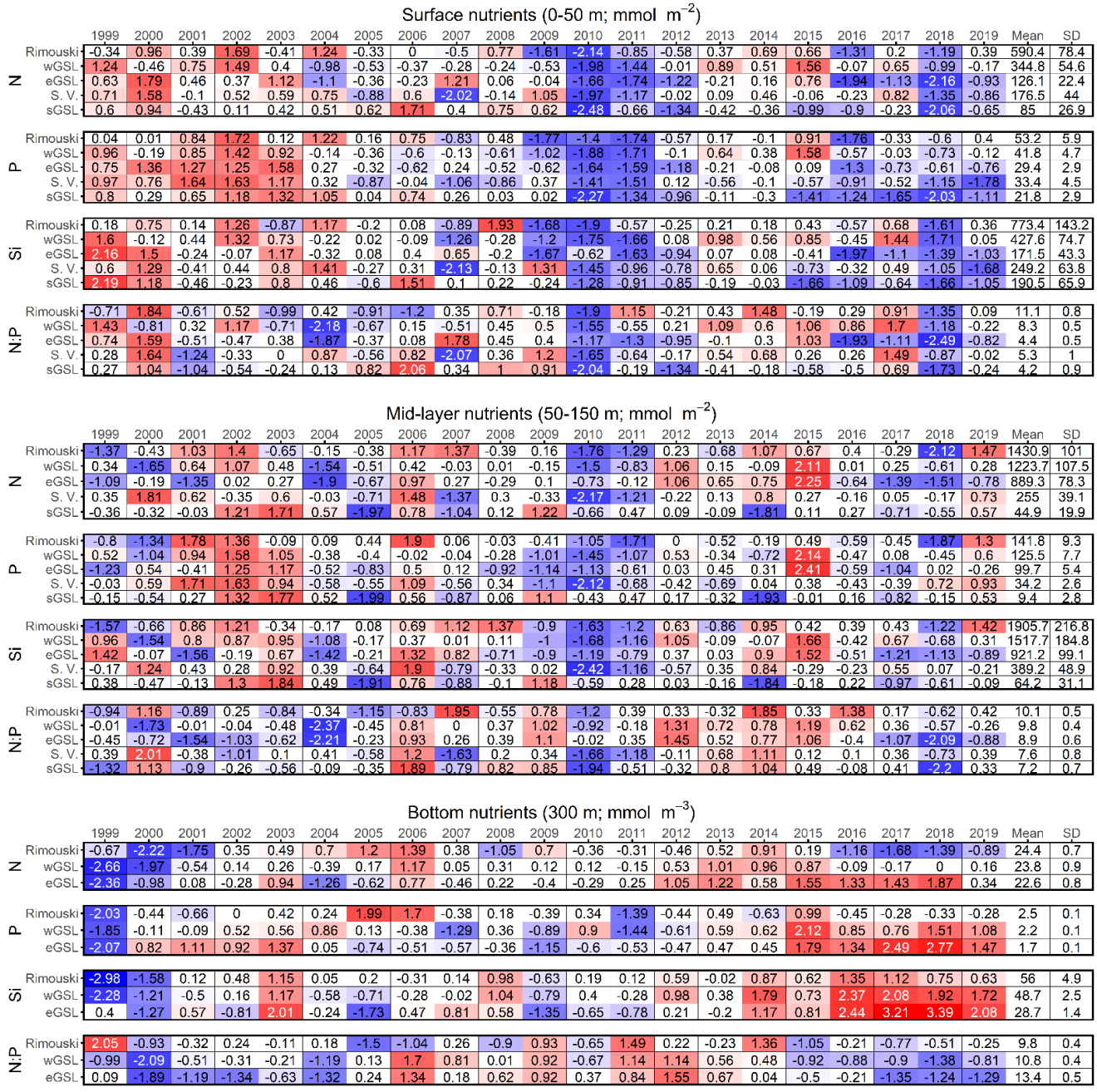

Figure 21. Time series of normalized annual anomalies for nitrate, phosphate, and silicate inventories as well as N:P ratio, in the surface and mid layers and at 300 m for GSL subregions and the high frequency monitoring stations. For Shediac Valley, the mid-layer integration depth is 50–84m Variable means and standard deviations for the 1999–2015 reference period are shown to the right of the scorecard. Blue colours indicate anomalies below the mean, reds are anomalies above the mean, and white represents normal conditions.

NO_3 (0-50 m; mmol m^{-2})

		1999	2000	2001	2002	2003	2004	2005	2006	2007	2008	2009	2010	2011	2012	2013	2014	2015	2016	2017	2018	2019	Mean	SD
Winter	wGSL	1.72	-0.55	-0.21	-0.19	0.93	0.36	0.08	0.13	1.42	-0.52	0.22	-2.08	-1.94	-0.19	0.42	0.88	-0.48	-0.09	-1.07	-0.01	-0.02	586.5	99.3
	eGSL	-0.71		0.14	0.12	1.55	1.13	-0.54	-0.1	1.03	-0.23	-0.07	-2.85	-0.45	-0.51	0.46	0.45	0.59	-0.89	-0.35	-0.18	0.68	311.4	43.8
	sGSL	0.61	0.55	0.25	0.33	0.09	0.76	-0.06	0.7	0.41	-0.13	0.56	-2.72	-0.53	-1.84	-0.68	0.29	1.39	-0.02	0	0.4	0.73	281	109.8
Summer	wGSL	0.04	-0.08	0.62	1.07	0.26	0.11	-0.66	-0.09	-0.41	0.41	-0.45	-2.31	-1.35	-1.03	1.21	1.67	0.98	-0.49	0.72	-1.88	0.33	228.2	46.8
	eGSL	-0.75	0.58	-0.02	-0.58	1.38	-1.38	-0.32	0.43	0.75	0.9	-0.09	-0.87	-1.76	-1.09	-0.06	1.62	1.26	-1.57	-1.45	-2.47	-0.71	61.1	21.7
	sGSL	0.44	0.72	-0.72	-0.04	0.49	-0.03	0.69	1.78	0.42	1.38	0.55	-2.11	-0.48	-0.45	-0.08	-0.84	-1.71	-0.97	-0.21	-2.08	-1.63	40	16.7
W - S	wGSL	2.17	-0.58	-0.62	-0.87	0.94	0.32	0.37	0.15	1.95	-0.81	0.44	-1.02	-1.25	0.23	-0.28	-0.03	-1.12	0.11	-1.53	0.76	-0.25	358.3	91
	eGSL	-0.47		0.17	0.43	1.17	2.11	-0.48	-0.39	0.9	-0.87	-0.05	-2.45	0.17	-0.12	0.62	-0.62	-0.11	-0.37	0.2	0.68	1.21	250.9	38
	sGSL	0.59	0.44	0.21	0.23	-0.18	0.93	-0.41	0.41	0.27	-0.66	0.49	-1.8	-0.72	-1.62	-0.91	0.27	2.47	-0.13	-0.19	0.53	1.04	240.9	107.8
Fall	wGSL	1.62	-0.43	0.72	1.51	-0.09	-1.89	-0.54	-0.67	-0.97	-0.62	-0.65	0.22	-0.38	1.24	0.22	-0.72	1.42	0.22	0.73	0.24	-0.65	351.5	79.9
	eGSL	1.58	1.32	1.15	1.31	0.24	-1.58	0.06	-0.59	1.09	-0.46	0.26	-0.17	-1.27	-0.8	-0.57	-1.29	-0.28	-1.44	-0.03	-1.33	-1.64	113.4	29.3
	sGSL	0.5	1.6	-0.06	-0.12	-0.15	1.46	0.69	1.5	-0.78	0.21	-0.29	-0.33	-1.97	-0.29	0.08	-0.2	-1.84	-0.83	-0.41	-4.04	-0.57	152	44.5

Chl *a* (0-100 m; mg m^{-2})

		1999	2000	2001	2002	2003	2004	2005	2006	2007	2008	2009	2010	2011	2012	2013	2014	2015	2016	2017	2018	2019	Mean	SD
Summer	wGSL	0.73	-1.28	0.49	1.3	1.44	-0.16	-1.04	-0.02	0.39	-1.07	0.59	0.59	-0.43	0.9	-2.33	0.33	-0.44	-0.84	0.16	1.8	1.35	69.9	26.3
	eGSL	0.25	0.59	0.08	2.18	-1.17	-0.47	-0.75	-0.42	-0.34	0.31	-0.24	-0.66	-1.23	-0.75	0.71	-0.34	2.26	-0.76	0.75	-0.87	0.13	34.5	12.4
	sGSL	0.63	-2.13	-0.01	2.64	-0.07	-0.21	-0.81	0.59	-0.17	-0.65	-0.42	0.83	-0.67	-0.32	0.28	-0.45	0.93	0.9	2.61	0.26	-0.53	31.1	9.6
Fall	wGSL	-0.67	-1.46	-0.33	0.05	0.8	-0.35	0.35	-0.13	-0.18	2.91	-0.67	-0.62	-1	0.42	-0.7	0.51	1.08	-0.24	-1.07	1.22	1.59	33.5	16.3
	eGSL	-0.73	-1.91	-0.38	0.82	0.88	-0.5	-1.19	-0.26	0.32	-0.39	0.61	-0.39	-0.87	-0.15	0.5	1.69	1.96	1.03	0.82	4.05	2.09	37.5	6.1
	sGSL	-0.37	-2.62	0.37	1.39	0.59	-0.95	-1.11	-0.89	1.01	-0.19	-0.19	-0.21	0.26	0.79	1.18	0.5	0.44	0.29	0.82	0.95	0.58	34.4	12.4
Annual	wGSL	-0.01	-1.95	0.29	0.98	1.71	-0.36	-0.36	-0.1	0.35	1.02	-0.01	0.06	-0.94	0.9	-2.2	0.46	0.16	-0.95	-0.84	1.91	1.84	47.6	12.5
	eGSL	-0.29	-0.65	-0.09	1.66	-0.18	-0.58	-1.18	-0.45	-0.06	-0.06	0.19	-0.58	-1.23	-0.6	0.79	0.58	2.74	-0.01	1.06	0.62	1.1	35.9	7.7
	sGSL	0.43	-2.42	0.18	2.37	0.33	-0.55	-1.13	-0.03	0.27	-0.63	-0.45	0.5	-0.47	0.05	0.92	-0.15	0.78	0.44	2.08	0.47	-0.27	32.7	8.9

Figure 22. Time series of normalized seasonal anomalies for nitrate and chlorophyll a inventories as well as normalized annual anomalies for chlorophyll a in the 0–50 m (nitrates) and 0–100 m (chl a) layers for GSL subregions. Variable means and standard deviations for the 1999–2015 reference period are shown to the right of the scorecard. Blue colours indicate anomalies below the mean, reds are anomalies above the mean, and white represents normal conditions. W–S is the difference in the nitrate inventory between winter and summer.

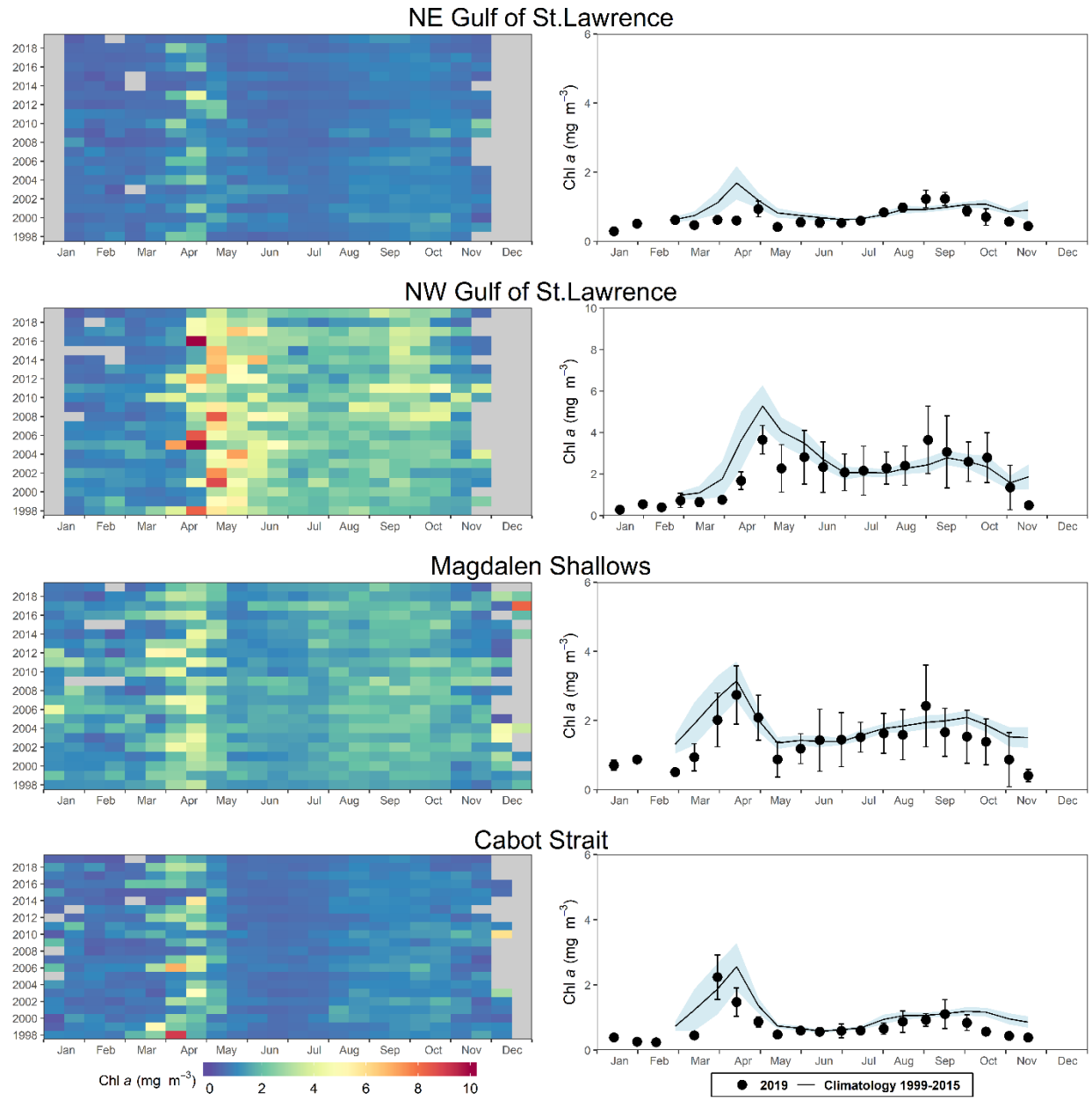

Figure 23. Left panels: time series of surface chlorophyll a concentrations from semi-monthly SeaWiFS (1998–2007), MODIS (2008–2011), and VIIRS (since 2012) ocean colour data in the northeast Gulf of St. Lawrence, northwest Gulf of St. Lawrence, Magdalen Shallows, and Cabot Strait statistical boxes (see Figure 4). Right panels: comparison of mean 2019 (black circles) surface chlorophyll a estimates using satellite ocean colour data with mean (± 0.5 SD) conditions from 1999–2015 (solid line with blue shading) for the same statistical boxes.

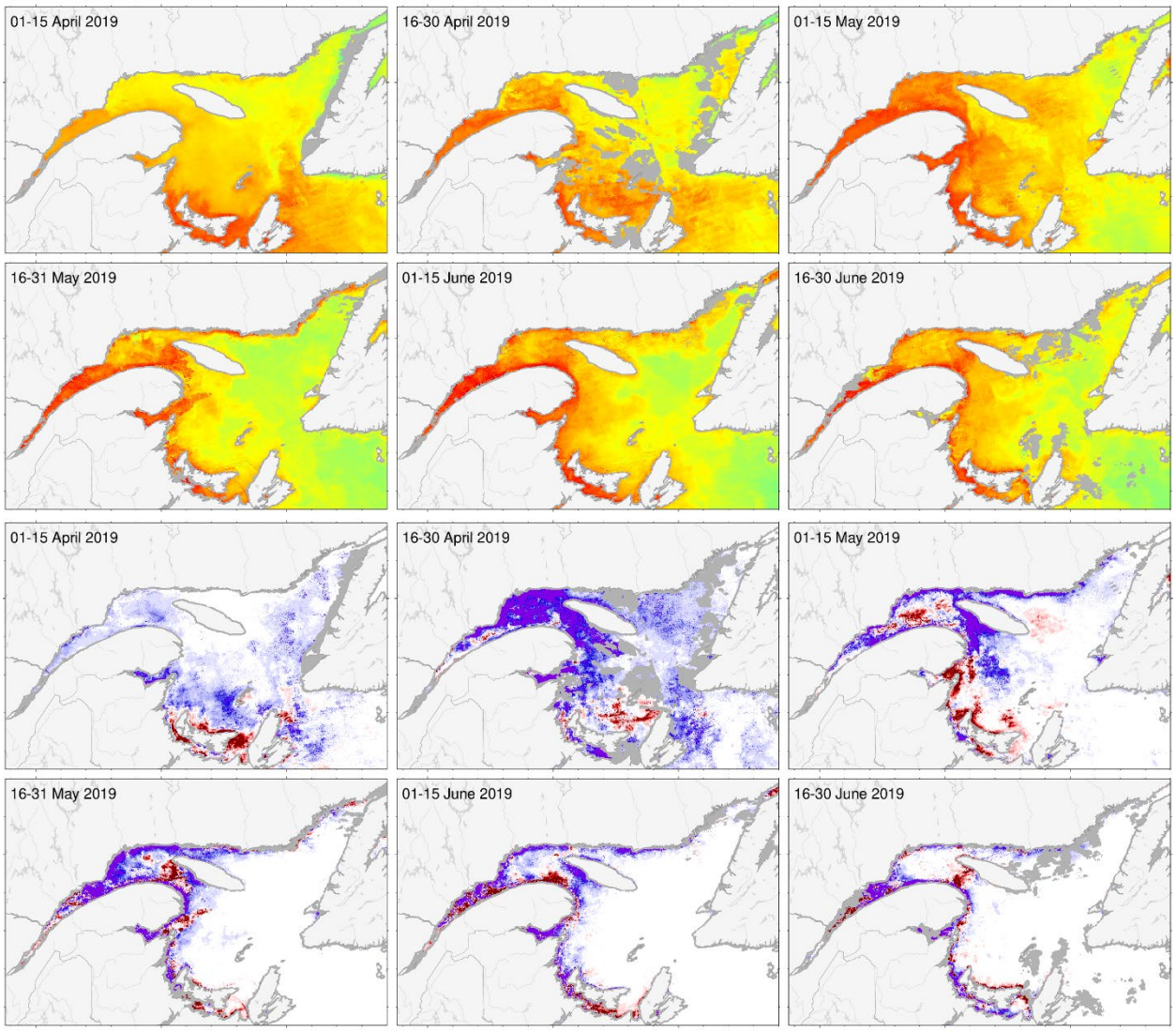

Figure 24. VIIRS twice-monthly composite images of surface chlorophyll a *(upper panels) and chlorophyll* a *anomaly based on the 1999–2015 climatology (lower panels) in the Gulf of St. Lawrence during spring/summer 2019.*

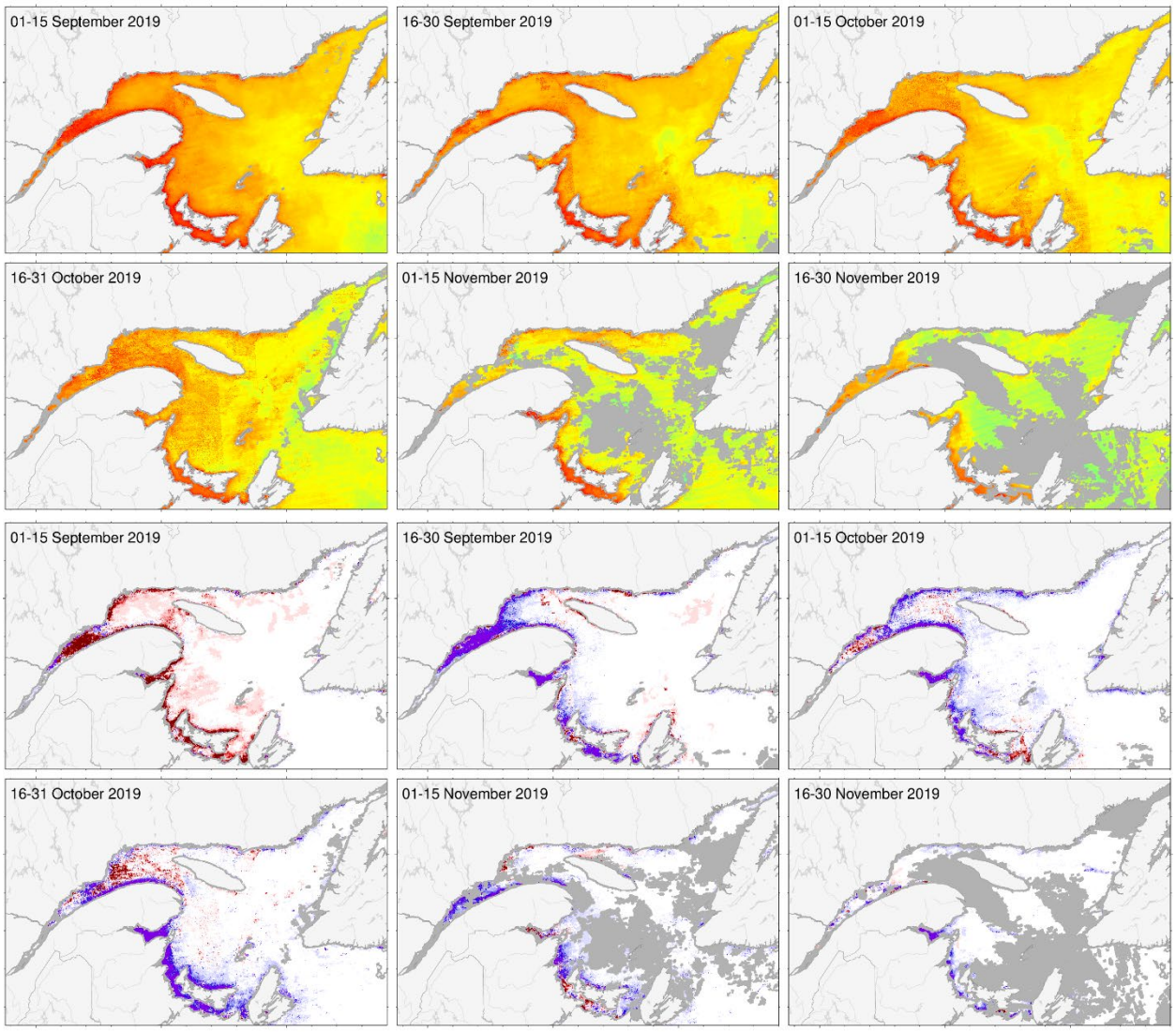

Figure 25. VIIRS twice-monthly composite images of surface chlorophyll a *(upper panels) and chlorophyll* a *anomaly based on the 1999–2015 climatology (lower panels) in the Gulf of St. Lawrence during fall 2019.*

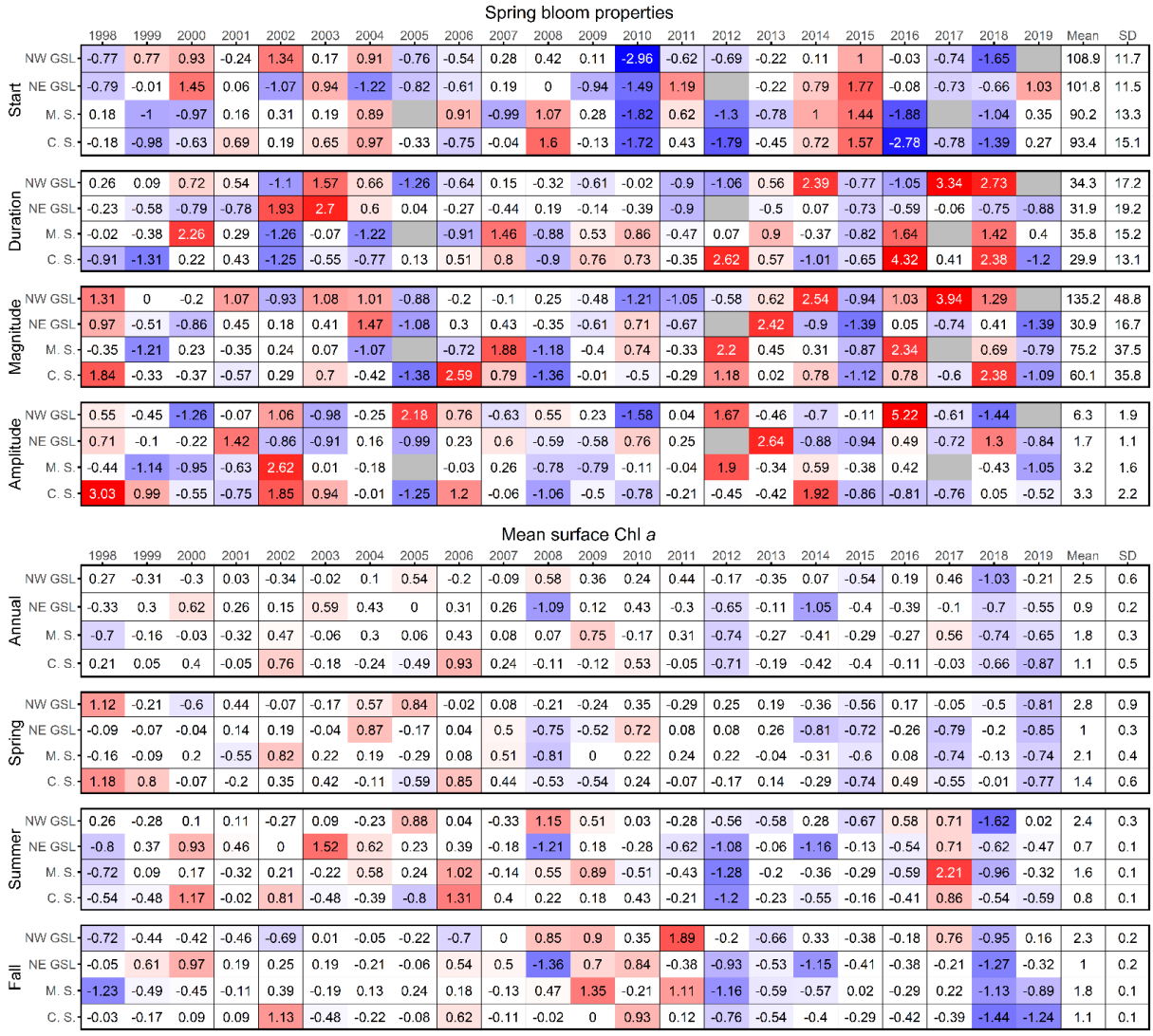

Figure 26. Time series of normalized anomalies for indices of change in spring bloom properties (upper section) and annual/seasonal mean surface chlorophyll a (lower section; mg m^{-3}) estimated from satellite ocean colour data (SeaWiFS: 1998–2007; MODIS: 2008–2011; and VIIRS 2012–present) across the Gulf of St. Lawrence statistical boxes (see Figure 4). The spring bloom indices are start (day of the year), duration (days), magnitude (mg chl m^{-2}), and amplitude (mg chl m^{-3}). Variable means and standard deviations for the 1999–2015 reference period are shown to the right of the scorecard. Blue colours indicate anomalies below the mean, reds are anomalies above the mean, and white represents normal conditions. Spring is from March to May, summer from June to August, and fall from September to November.

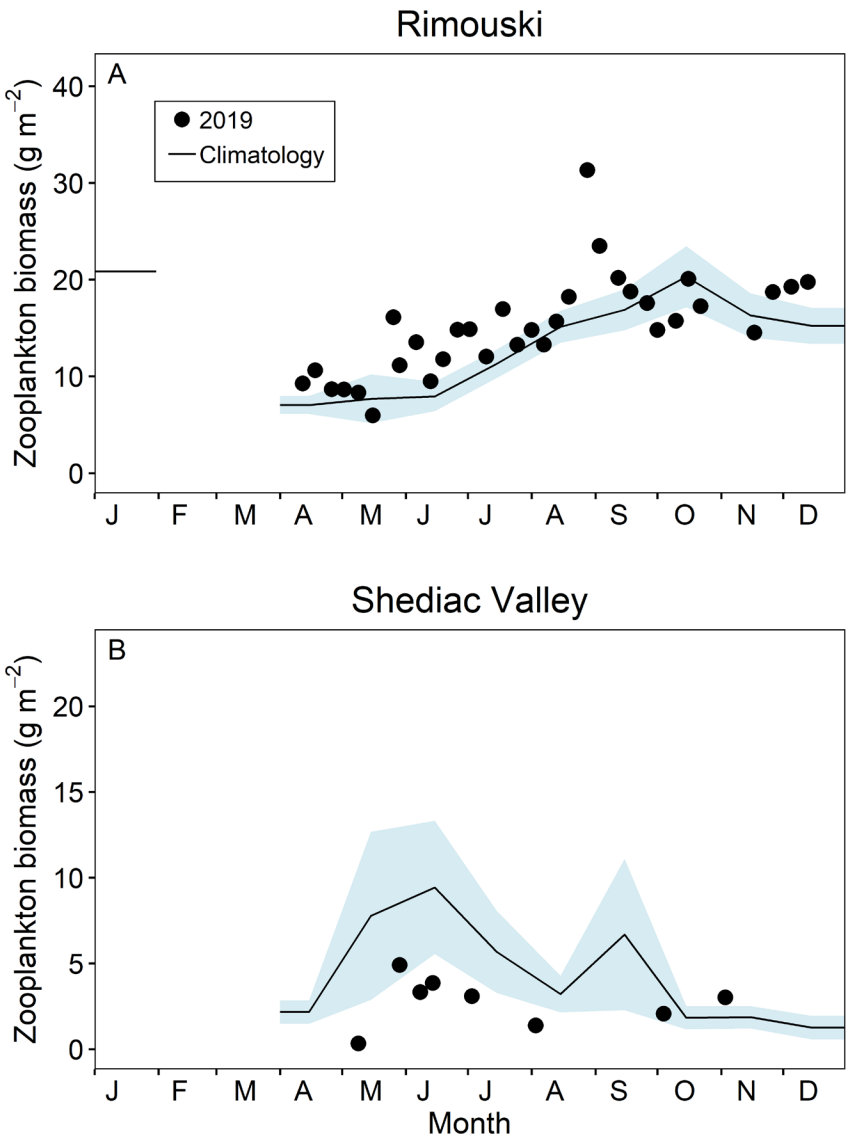

Figure 27. Comparison of total zooplankton biomass (dry weight) in 2019 (circles) with the monthly climatology from (A) Rimouski (2005–2015) and (B) Shediac Valley (1999–2015) stations (black line with blue shading). Blue shading represents ± 0.5 SD of the monthly means.

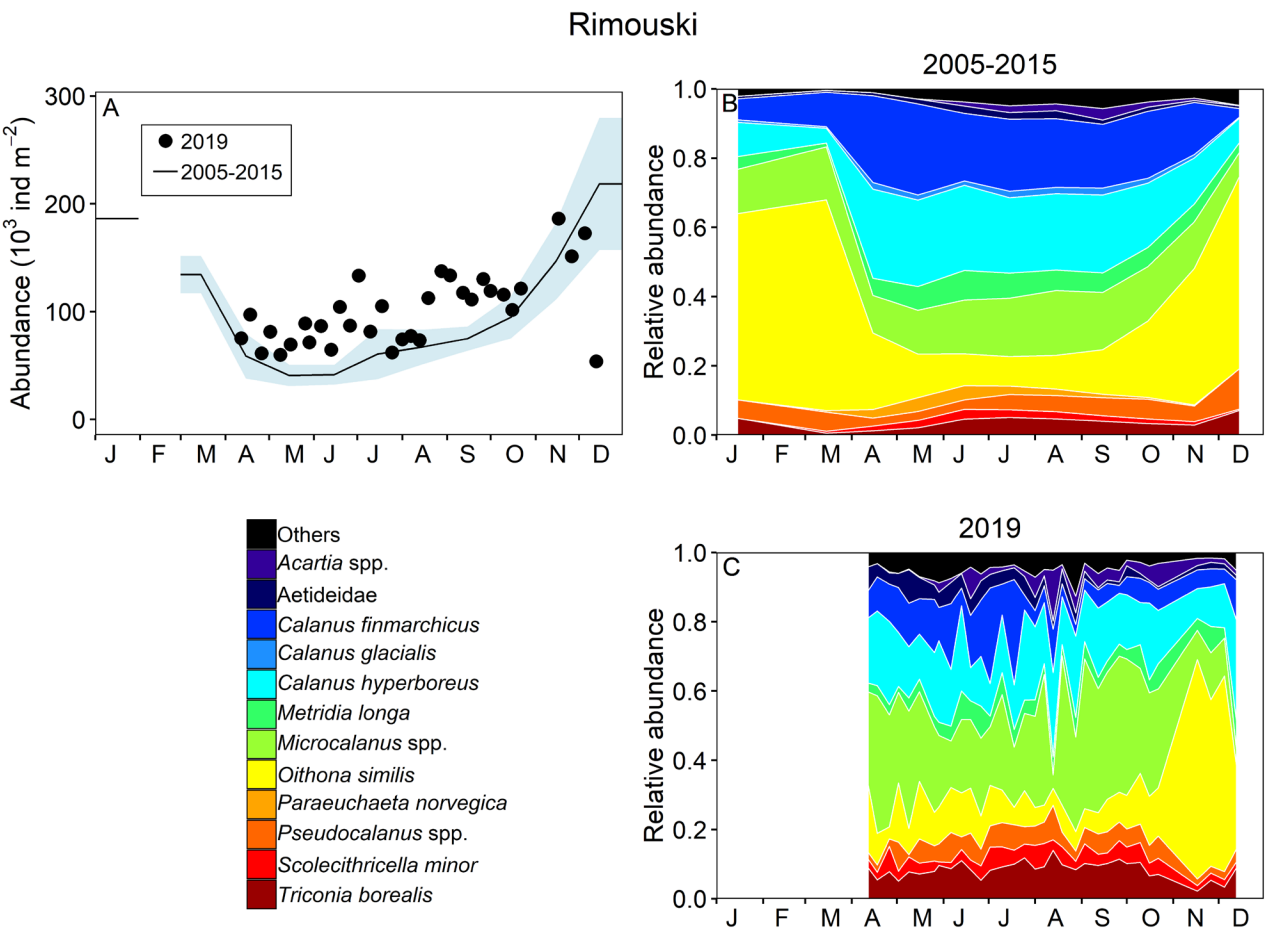

Figure 28. Seasonal variability of dominant copepods at Rimouski station. Copepod abundance (excluding nauplii) during the reference period (black line with blue shading indicating ± 0.5 SD) and in 2019 (circles) (A); climatology of the relative abundance of the identified copepod taxa representing 95% of total copepod abundance during the 2005–2015 period (B) and in 2019 (C).

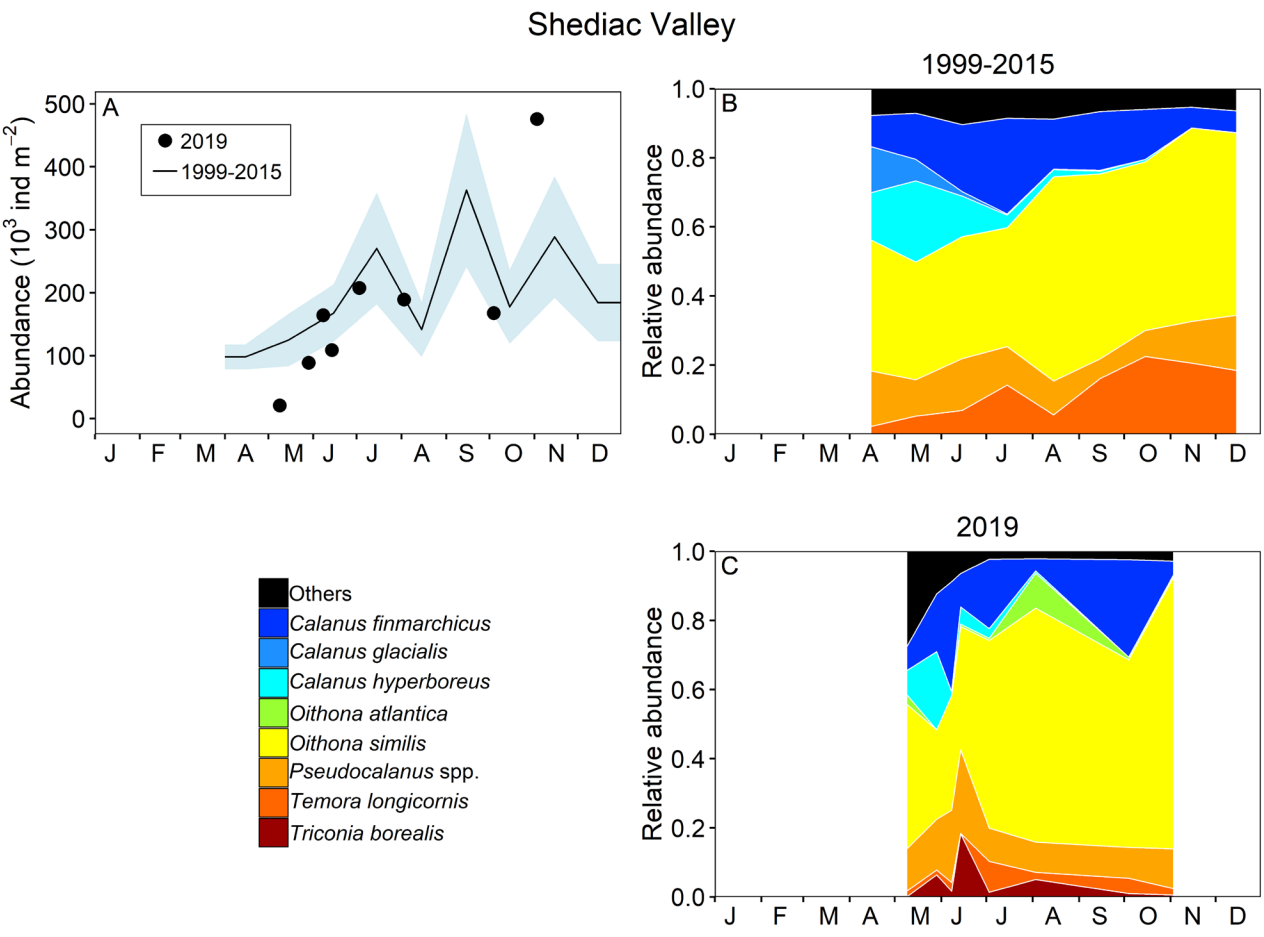

Figure 29. Seasonal variability of dominant copepods at Shediac Valley station. Copepod abundance (excluding nauplii) during the reference period (black line with blue shading indicating ± 0.5 SD) and 2019 (circles) (A); climatology of the relative abundance of the identified copepod taxa representing 95% of total copepod abundance during the 1999–2015 period (B) and in 2019 (C).

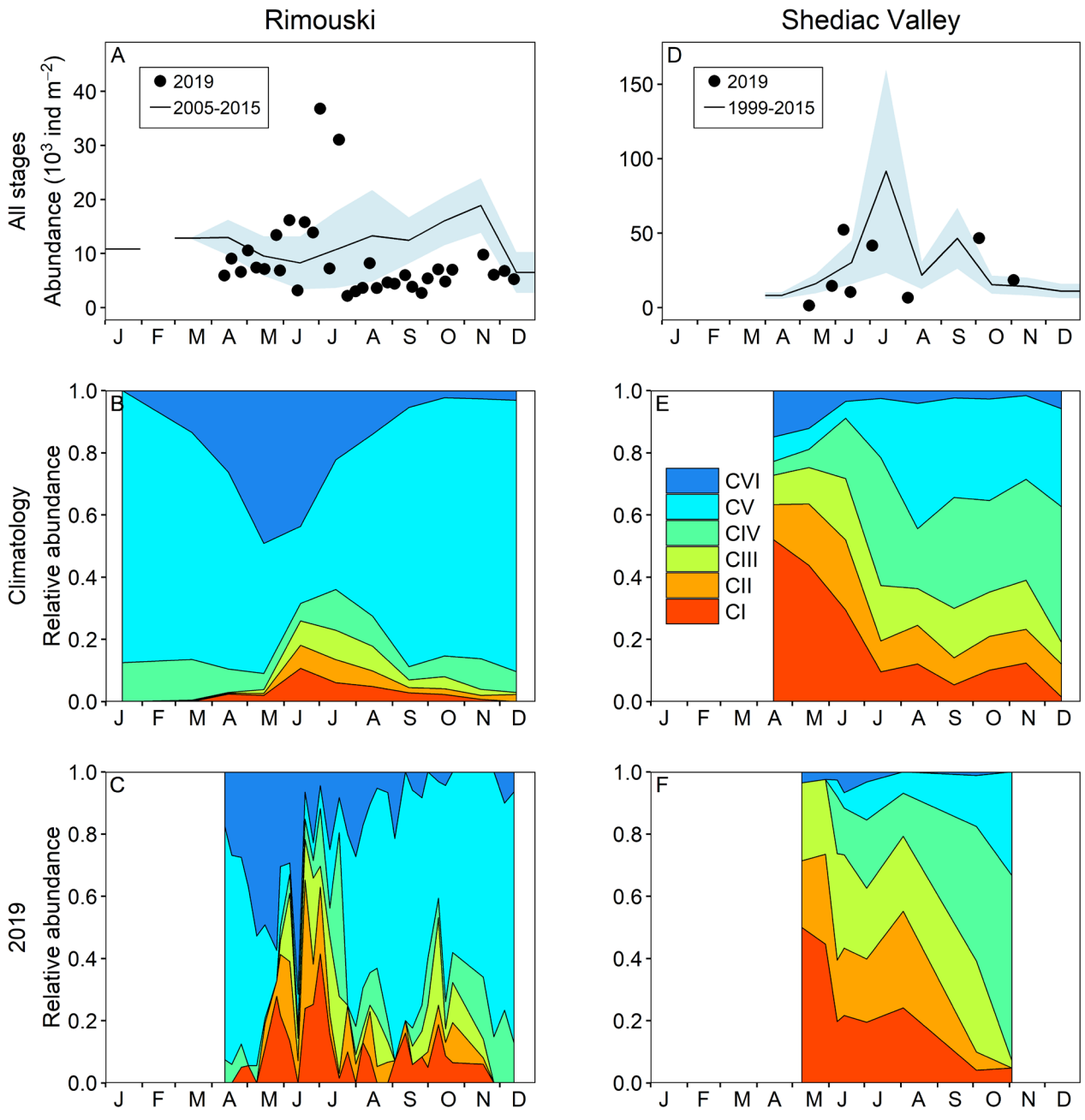

Figure 30. Seasonal variability in Calanus finmarchicus *copepodite abundance at Rimouski (A–C) and Shediac Valley (D–F) stations. The climatologies of the combined counts for the reference periods (black line with blue shading indicating ± 0.5 SD) are plotted with data from 2019 (circles) (A, D). The seasonal variabilities for the individual copepodite stages for the reference periods (B, E) and for 2019 (C, F) are also shown.*

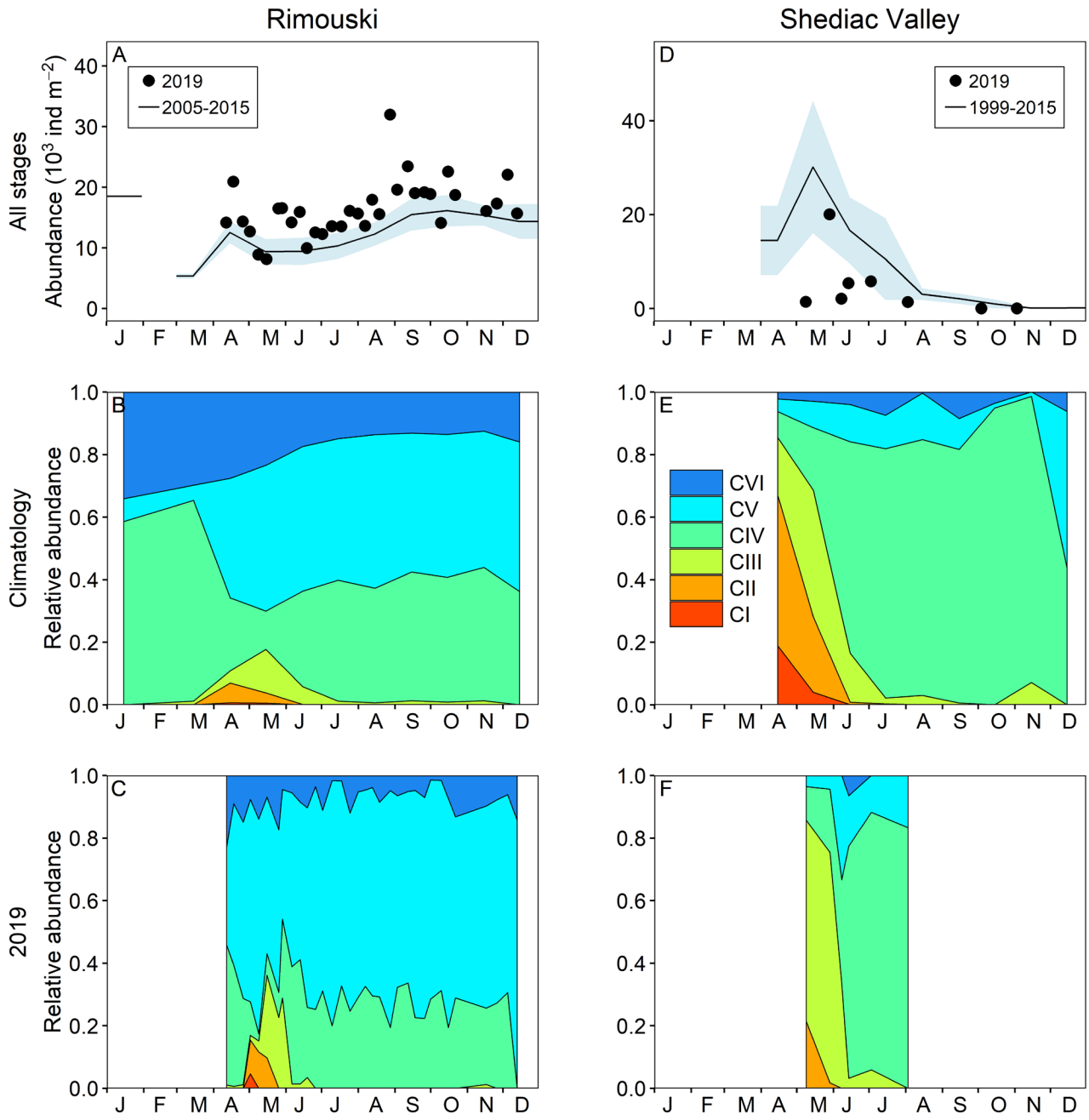

Figure 31. Seasonal variability in Calanus hyperboreus *copepodite abundance at Rimouski (A–C) and Shediac Valley (D–F) stations. The climatologies of the combined counts for the reference periods (black line with blue shading indicating ± 0.5 SD) are plotted with data from 2019 (circles) (A, D). The seasonal variabilities for the individual copepodite stages for the reference periods (B, E) and for 2019 (C, F) are also shown.*

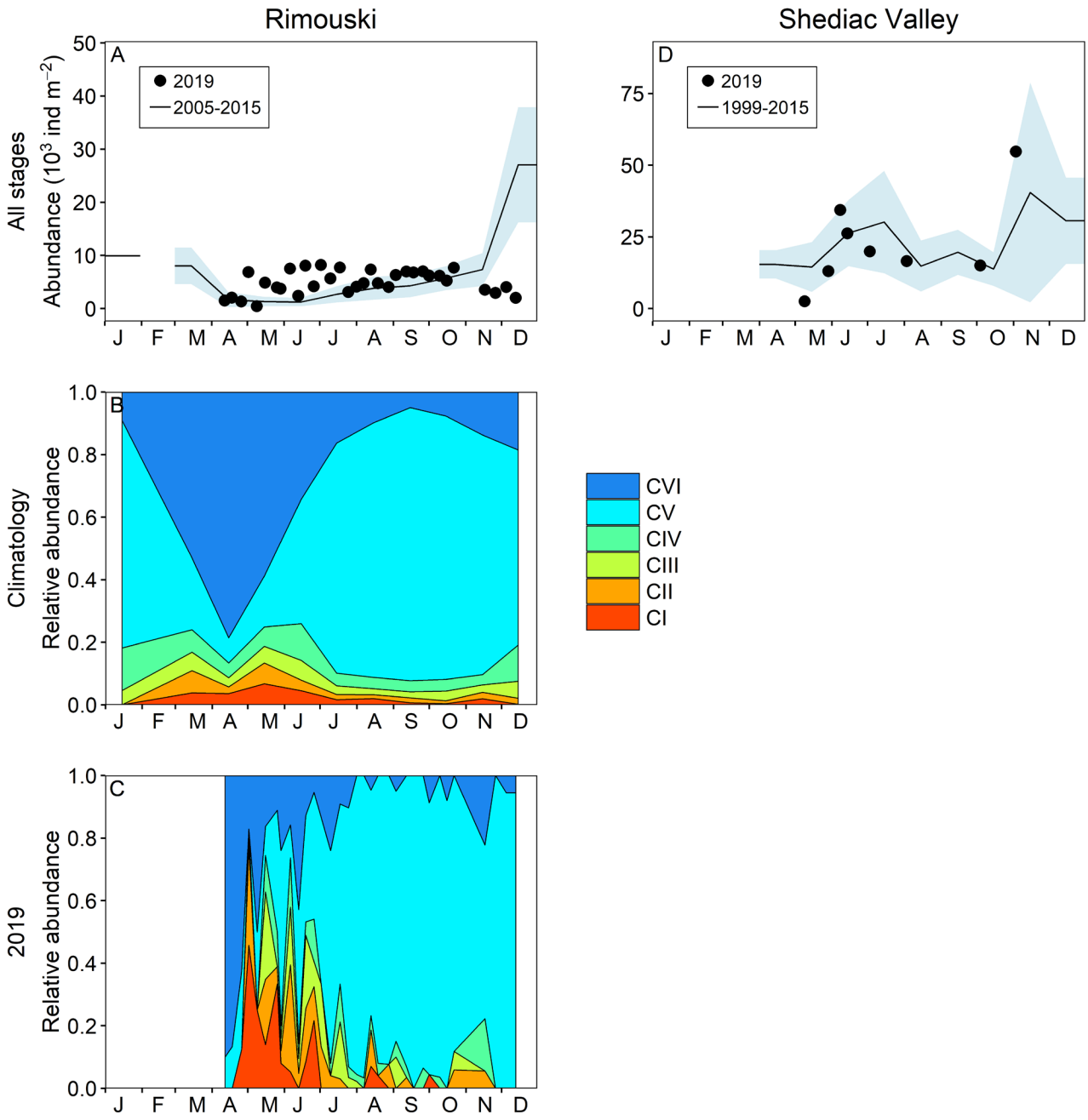

Figure 32. Seasonal variability in Pseudocalanus spp. copepodite abundance at Rimouski (A–C) and Shediac Valley (D) stations. The climatologies of the combined counts for the reference periods (black line with blue shading indicating ± 0.5 SD) are plotted with data from 2019 (circles) (A, D). Seasonal variability for the individual copepodite stages for the reference period (B) and for 2019 (C) are also shown. No stage information is available for Shediac Valley.

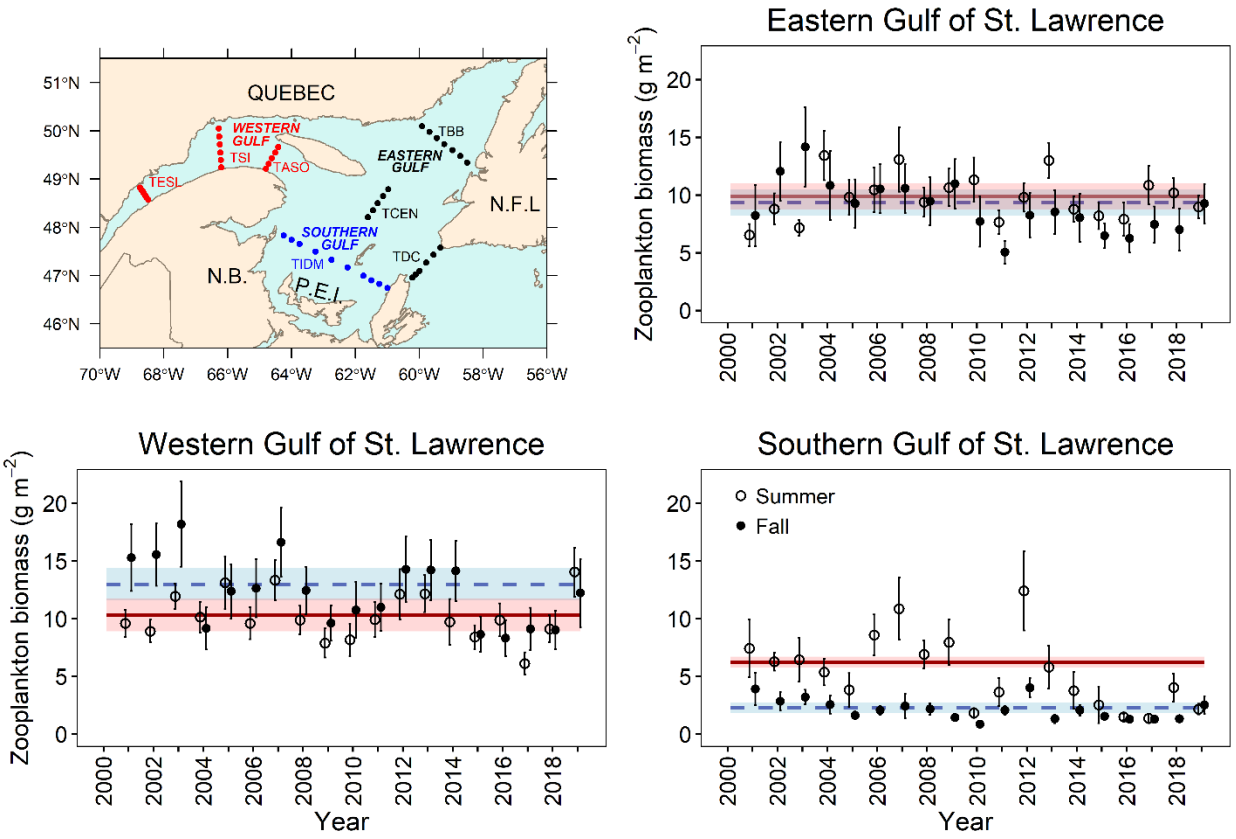

Figure 33. Time series of mean total zooplankton biomass (dry weight) during summer (open circles) and fall (filled circles) for the three subregions of the Gulf of St. Lawrence. Vertical lines represent standard errors. Solid red line and dashed blue line represent the climatology (1999–2015) *averages (shading represents ± 0.5 SD) for summer and fall, respectively.*

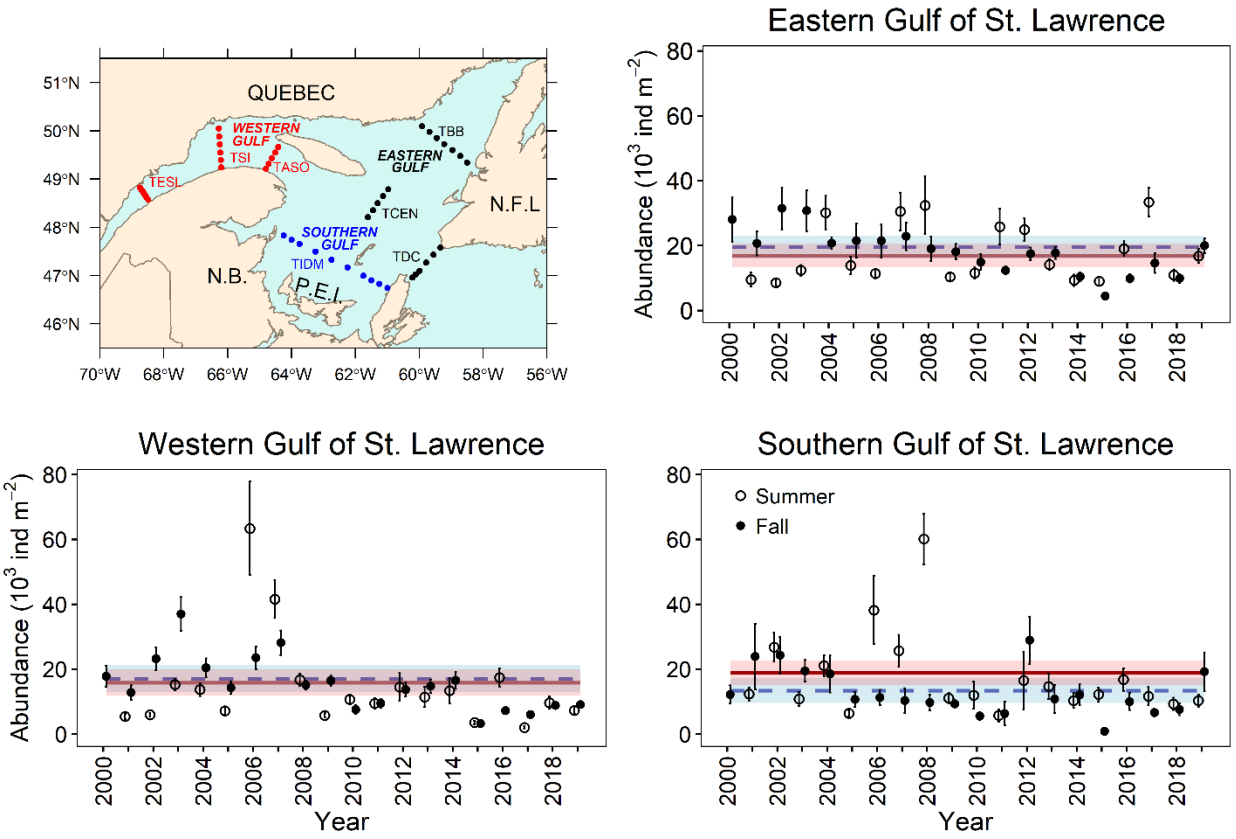

Figure 34. Time series of mean total abundance of Calanus finmarchicus *during summer (open circles) and fall (filled circles) for the three subregions of the Gulf of St. Lawrence. Vertical lines represent standard errors. Solid red line and dashed blue line represent the climatology* (1999–2015) *averages (shading represents ± 0.5 SD) for summer and fall, respectively.*

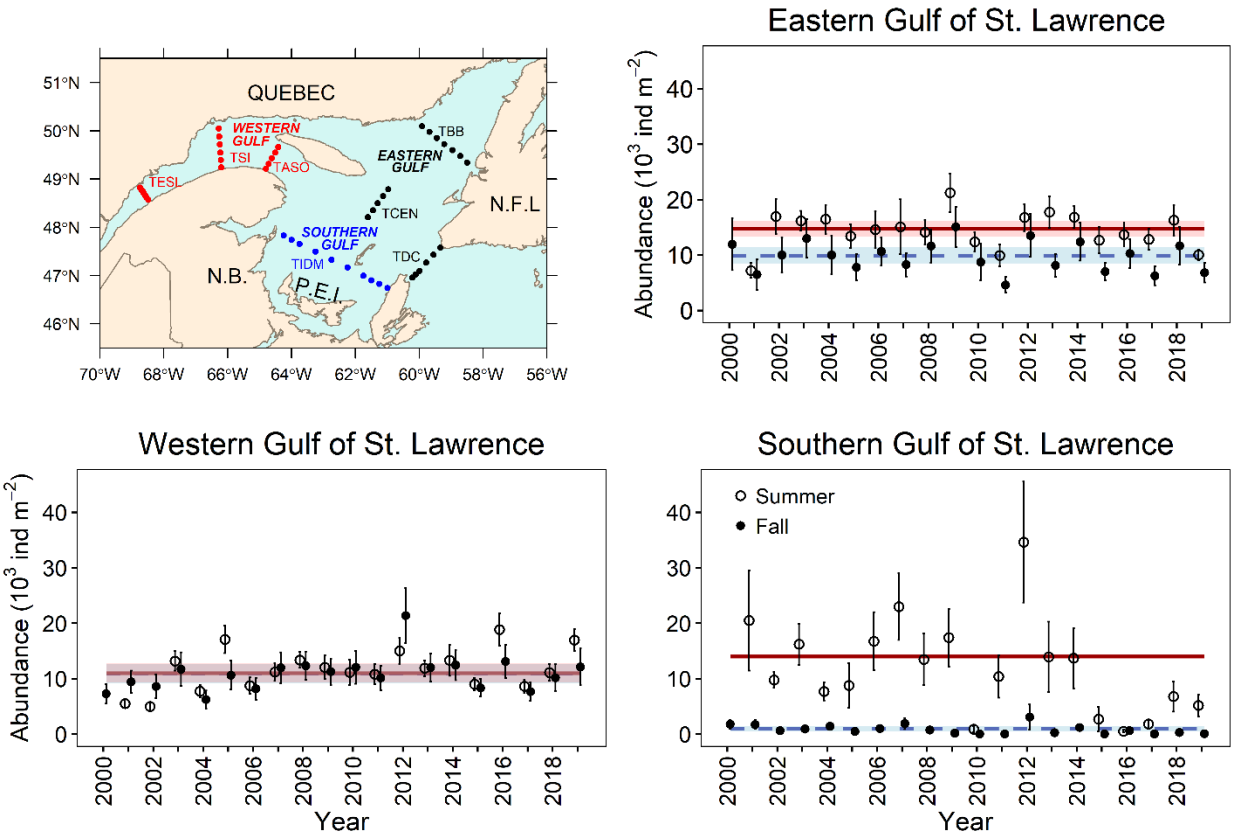

Figure 35. Time series of mean total abundance of Calanus hyperboreus *during summer (open circles) and fall (filled circles) for the three subregions of the Gulf of St. Lawrence. Vertical lines represent standard errors. Solid red line and dashed blue line represent the climatology* (1999–2015) *averages (shading represents ± 0.5 SD) for summer and fall, respectively.*

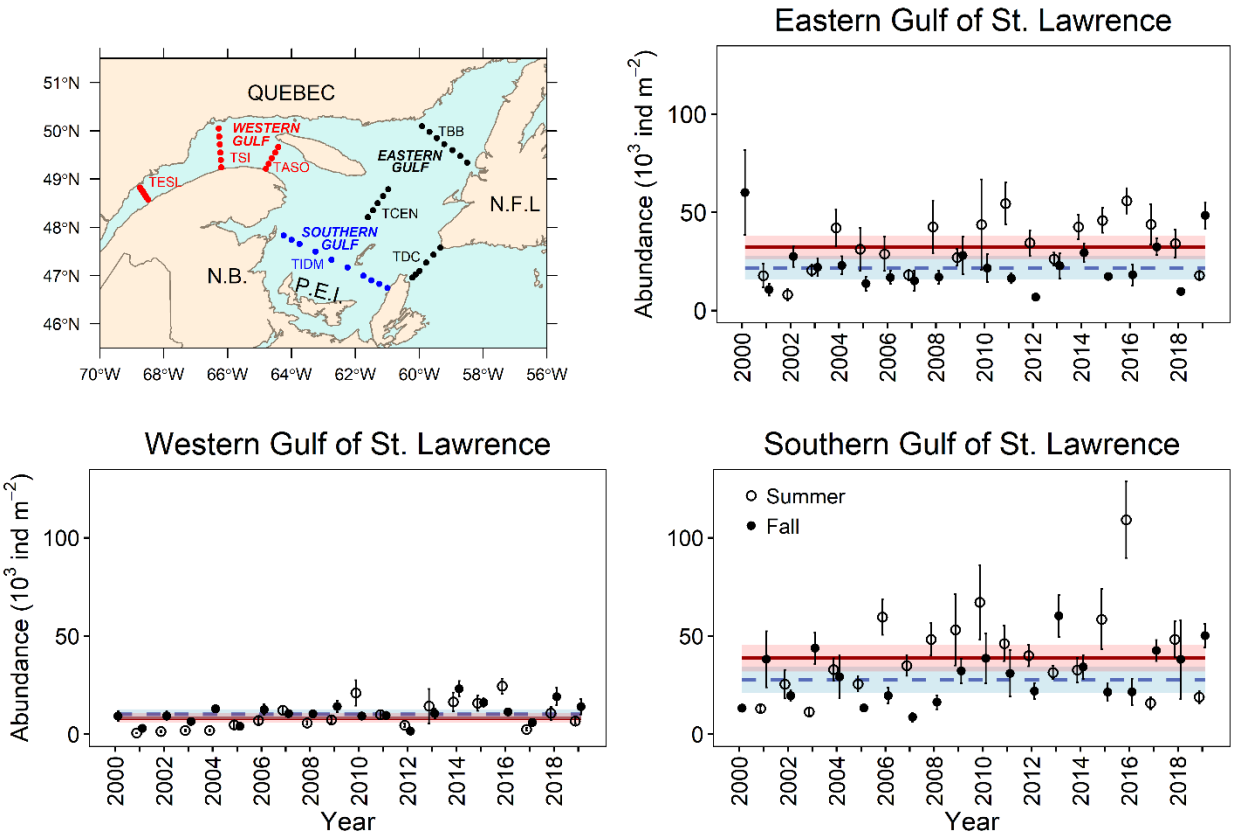

Figure 36. Time series of mean total abundance of Pseudocalanus *spp. during summer (open circles) and fall (filled circles) for the three subregions of the Gulf of St. Lawrence. Vertical lines represent standard errors.* Solid red line and dashed blue line represent the climatology (1999–2015) averages (shading represents ± 0.5 SD) for summer and fall, respectively.

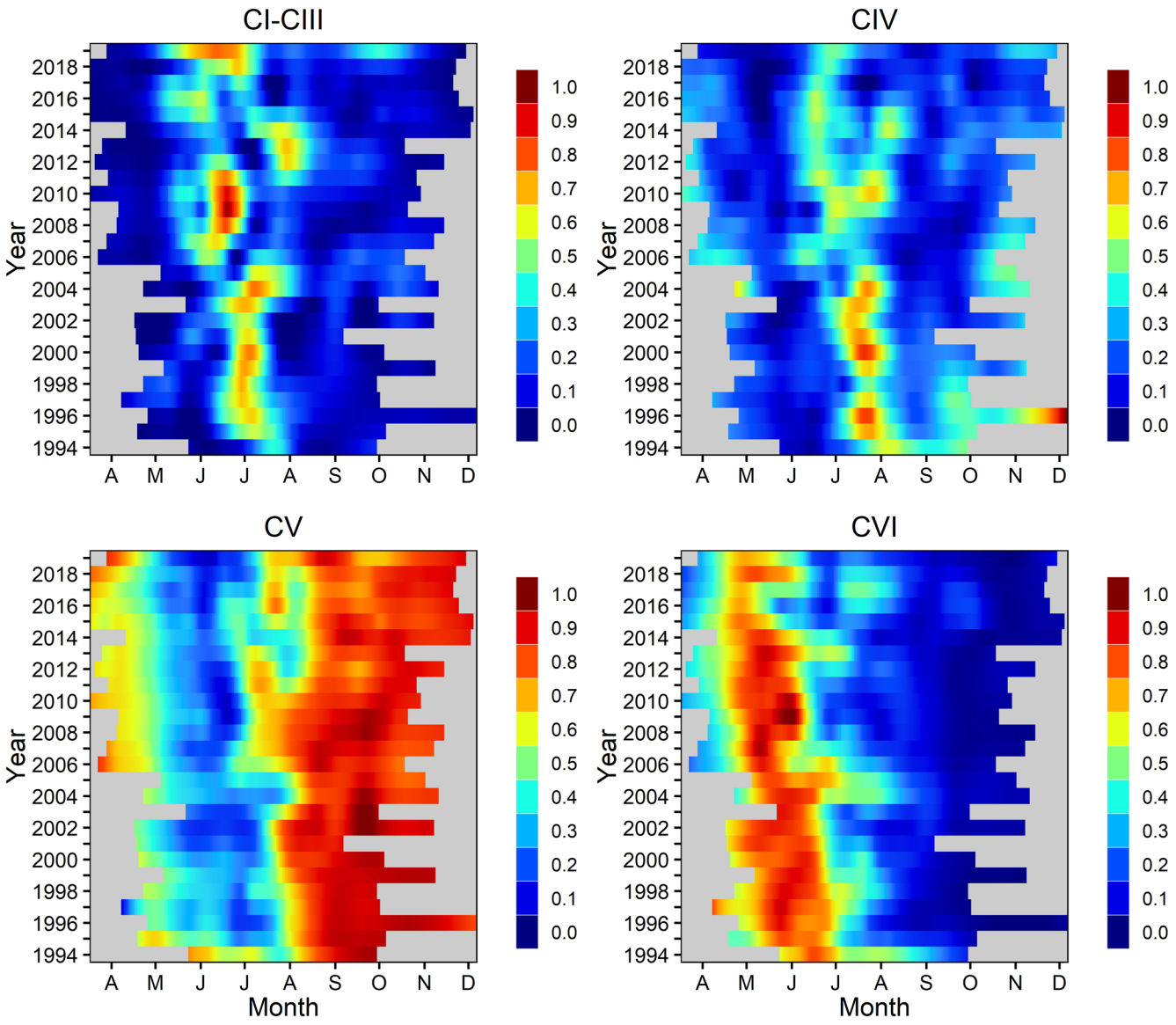

Figure 37. Time series of the seasonal cycle in relative proportion of total abundance for Calanus finmarchicus *copepodite stages (CI–CIII, CIV, CV, and CVI male + female) at Rimouski station. Proportions are normalized by the annual maximum and smoothed using a Loess regression.*

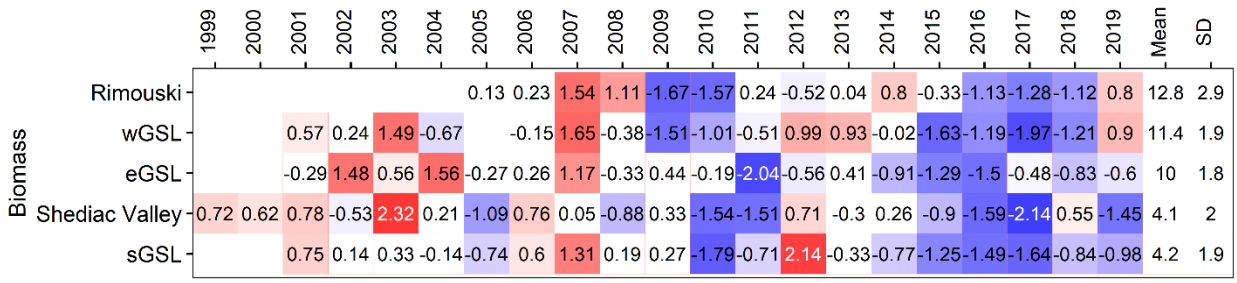

Figure 38. Time series of normalized annual anomalies of zooplankton biomass (dry weight; g m^{-2}) at the high-frequency monitoring stations and the three subregions of the Gulf of St. Lawrence. Variable means and standard deviations for the 1999–2015 (2005–2015 for Rimouski) reference period are shown to the right of the scorecard. Blue colours indicate anomalies below the mean, reds are anomalies above the mean, and white represents normal conditions.

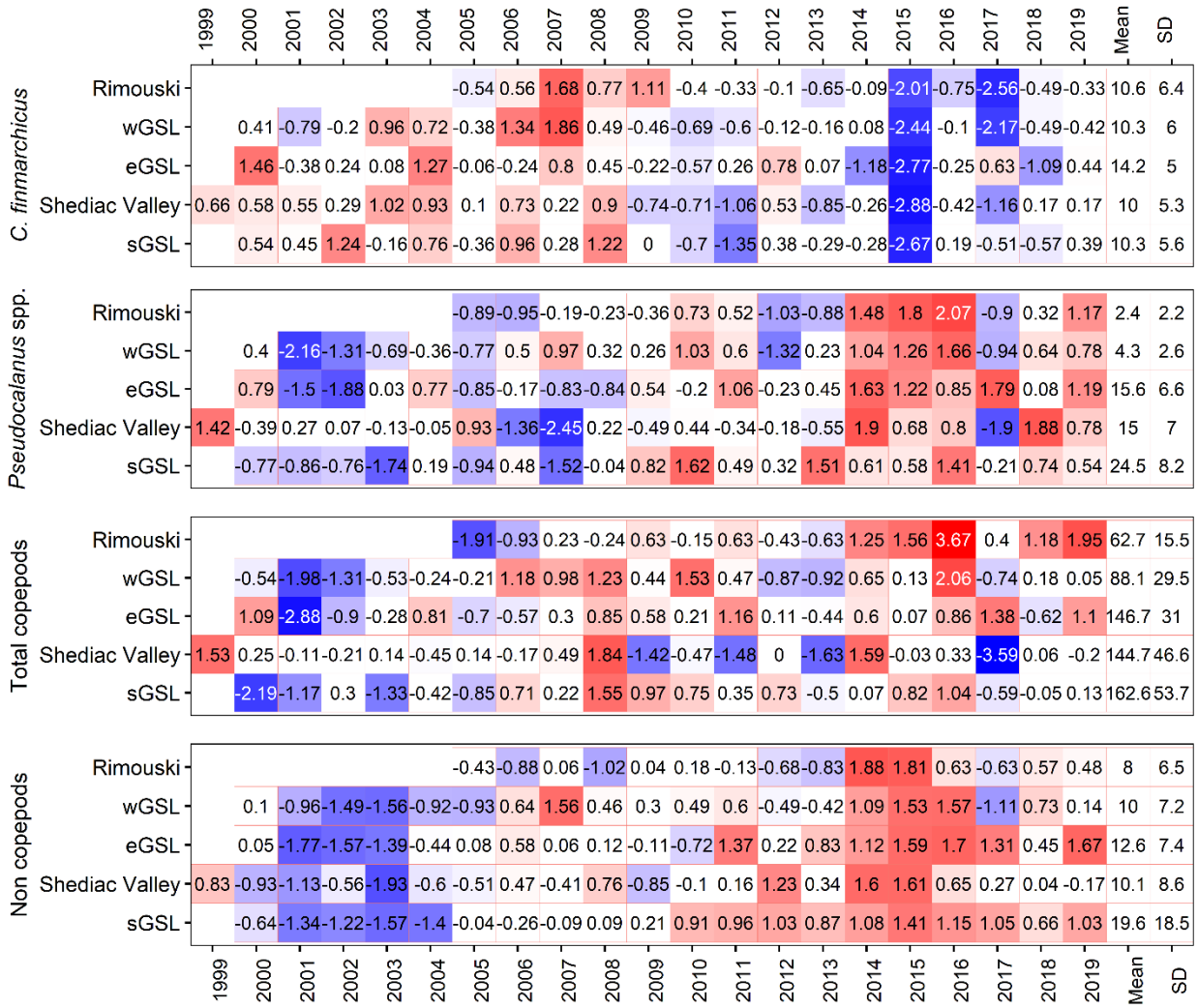

Figure 39. Time series of normalized annual anomalies for the abundance (×10³ ind m⁻²) of four zooplankton categories at the high-frequency monitoring stations and the three subregions of the Gulf of St. Lawrence. Variable means and standard deviations for the 1999–2015 (2005–2015 for Rimouski) reference period are shown to the right of the scorecard. Blue colours indicate anomalies below the mean, reds are anomalies above the mean, and white represents normal conditions.

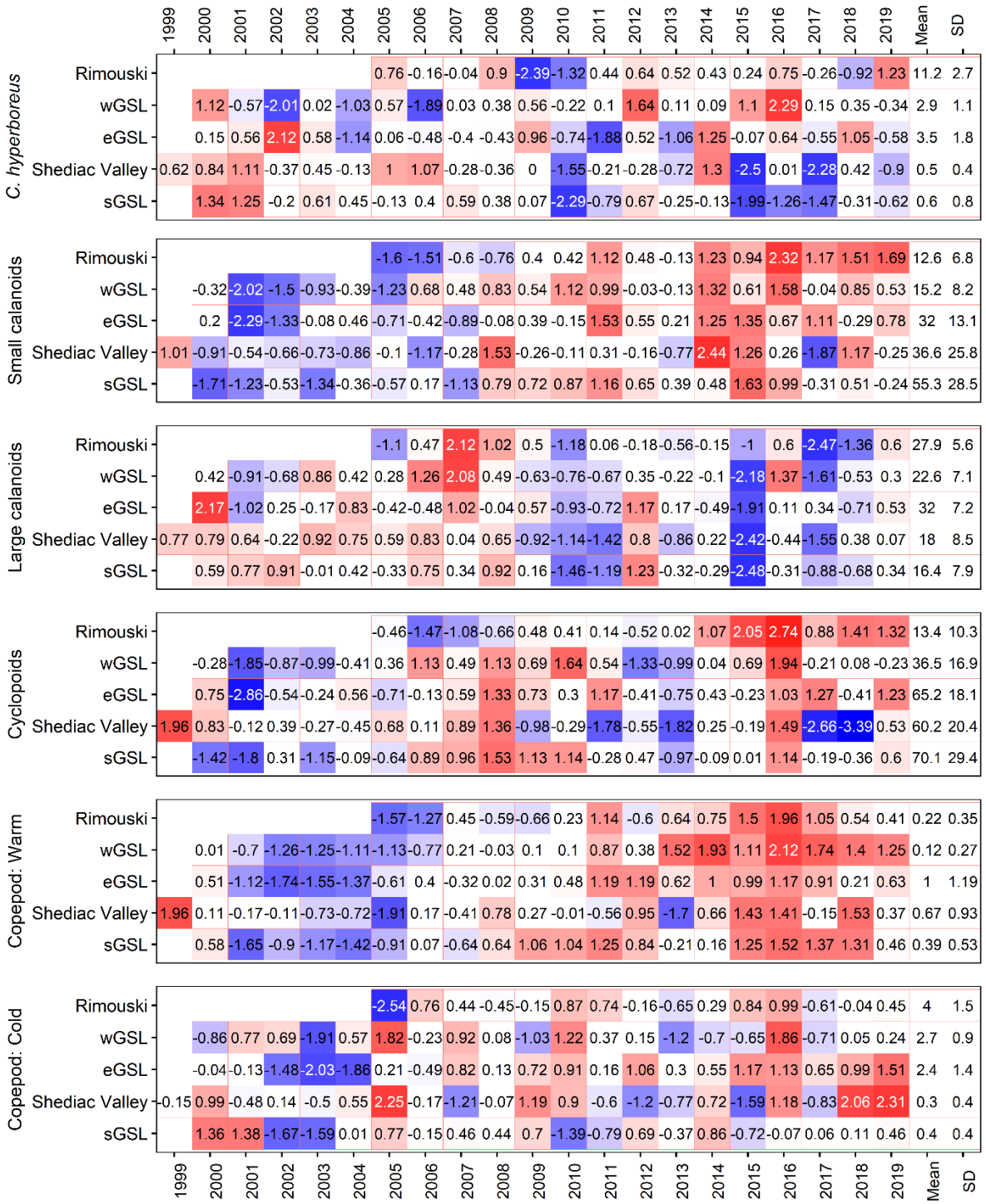

Figure 40. Time series of normalized annual anomalies for the abundance (×10³ ind m⁻²) of six categories of zooplankton assemblages at the high-frequency monitoring stations and the three subregions of the Gulf of St. Lawrence. Variable means and standard deviations for the 1999–2015 (2005–2015 for Rimouski) reference period are shown to the right of the scorecard. Blue colours indicate anomalies below the mean, reds are anomalies above the mean, and white represents normal conditions. A detailed list of species included in each large copepod index is presented in Appendix 1.

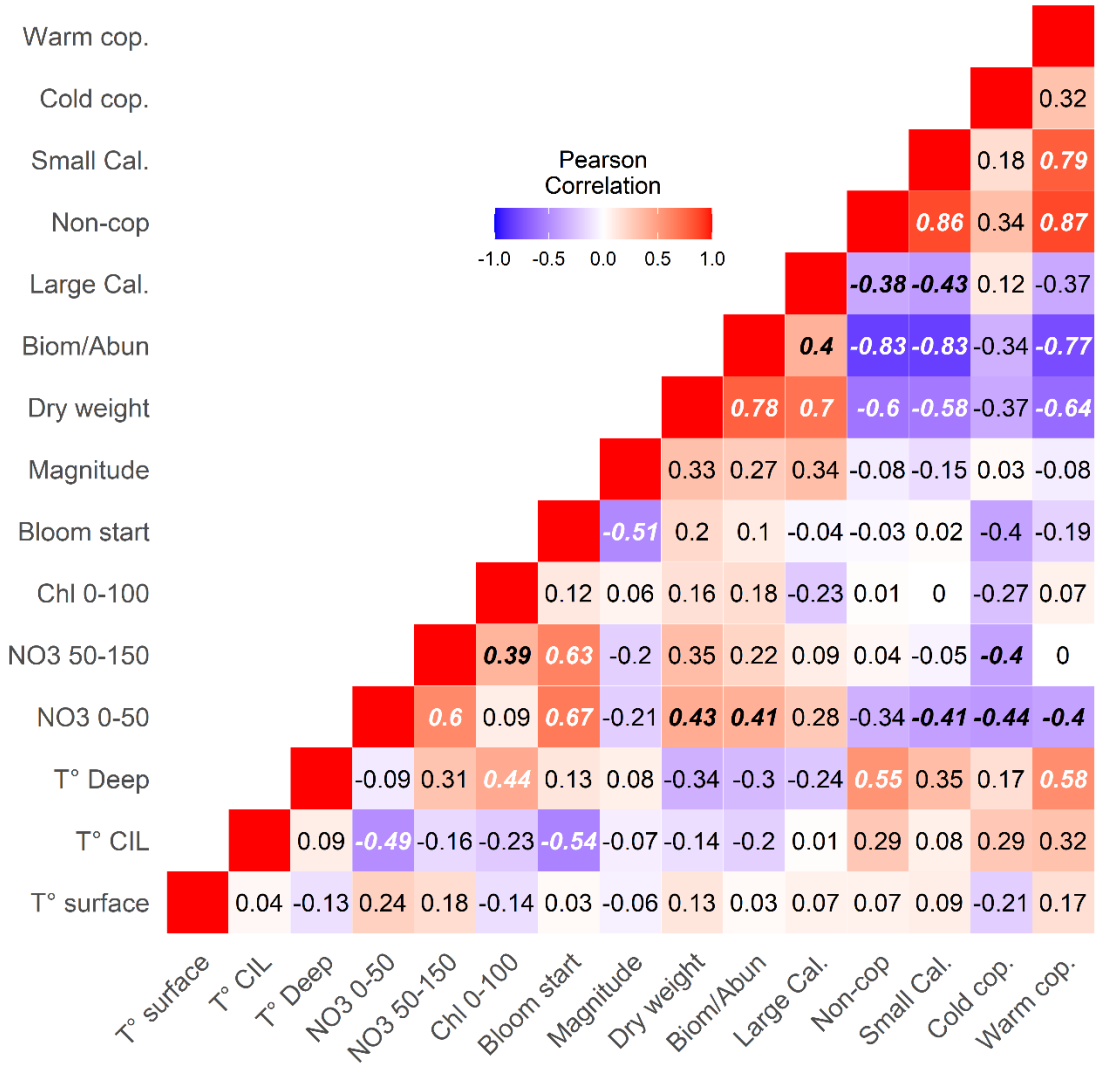

Figure 41. Correlation matrix for summed anomalies of some GSL indices. Blue colours indicate negative correlations, reds are positive correlations, and white represents normal conditions. Significant correlations ($p < 0.1$) are indicated in black bold-italic, or in white bold-italic ($p < 0.05$). Biom/Abun is used as an index of zooplankton average size.

APPENDICES

Appendix 1. List of taxa associated with each large copepod index.

Large copepod index	Taxa
Small calanoids	*Acartia* spp.
	Aetideidae
	Centropages spp.
	Clausocalanus spp.
	Eurytemora spp.
	Microcalanus spp.
	Nannocalanus minor
	Paracalanus parvus
	Pseudocalanus spp.
	Scolecithricella spp.
	Spinocalanus spp.
	Temora spp.
	Tortanus spp.
Large calanoids	*Anomalocera* spp.
	Calanus finmarchicus
	Calanus glacialis
	Calanus hyperboreus
	Euchaeta spp.
	Metridia spp.
	Paraeuchaeta norvegica
	Pleuromamma borealis
	Pleuromamma robusta
Warm copepods	*Centropages* spp.
	Clausocalanus spp.
	Metridia lucens
	Nannocalanus minor
	Paracalanus spp.
	Pleuromamma borealis
	Pleuromamma robusta
Cyclopoids	*Oithona* spp.
	Oncaea spp.
	Triconia borealis
	Triconia conifer
	Triconia similis
Cold copepods	*Metridia longa*
	Calanus glacialis

Appendix 2. GLM results for Rimouski and Shediac Valley stations. Significance of the year and month effects as well as the adjusted R squared of the regression for nutrients or chorophyll a are presented.

Station	Index	Year (*p*)	Month (*p*)	R^2
Rimouski	Chlorophyll *a* (0–100m)	<0.0001	<0.0001	0.41
	Nitrate (0–50m)	<0.0001	<0.0001	0.33
	Phosphate (0–50m)	<0.0001	<0.0001	0.32
	Silicate (0–50m)	<0.0001	<0.0001	0.46
	Nitrate (50–150m)	<0.0001	<0.0001	0.25
	Phosphate (50–150m)	<0.0001	<0.0001	0.31
	Silicate (50–150m)	<0.0001	<0.001	0.27
	Nitrate (300m)	<0.0001	0.005	0.48
	Phosphate (300m)	<0.0001	0.02	0.36
	Silicate (300m)	<0.0001	<0.0001	0.61
	Nitrate (150–320m)	<0.0001	0.3	0.39
Shediac Valley	Chlorophyll *a* (0–100m)	<0.0001	<0.0001	0.38
	Nitrate (0–50m)	<0.001	<0.0001	0.34
	Phosphate (0–50m)	<0.0001	<0.0001	0.35
	Silicate (0–50m)	0.001	<0.0001	0.29
	Nitrate (50–150m)	0.3	<0.0001	0.15
	Phosphate (50–150m)	<0.01	<0.0001	0.32
	Silicate (50–150m)	0.4	<0.0001	0.20

Appendix 3. GLM results for Rimouski and Shediac Valley stations. Significance of the year and month effects as well as the adjusted R squared of the regression for phytoplankton groups are presented.

Region	Group	Year (*p*)	Month (*p*)	R^2
Rimouski	Diatoms	<0.0001	<0.0001	0.37
	Dinoflagellates	<0.0001	<0.0001	0.53
	Flagellates	<0.0001	<0.0001	0.38
	Ciliates	<0.0001	<0.0001	0.35
	Total	<0.0001	<0.0001	0.24
	Diatoms/Dinoflagellates	<0.0001	<0.0001	0.32
	Diatoms/Flagellates	<0.0001	<0.0001	0.24
Shediac Valley	Diatoms	<0.0001	<0.001	0.36
	Dinoflagellates	<0.0001	0.03	0.37
	Flagellates	<0.0001	<0.0001	0.54
	Ciliates	0.07	0.4	0.08
	Total	<0.0001	<0.0001	0.39
	Diatoms/Dinoflagellates	<0.0001	<0.001	0.38
	Diatoms/Flagellates	<0.0001	<0.0001	0.43

Appendix 4. GLM results for GSL subregions. Significance of the year, season, and station effects as well as the adjusted R squared of the regression for nutrients or chorophyll a are presented.

Region	Index	Year (*p*)	Season (*p*)	Station(*p*)	R^2
wGSL	Chlorophyll *a* (0–100m)	<0.0001	<0.0001	<0.0001	0.36
	Nitrate (0–50m)	<0.0001	<0.0001	<0.0001	0.69
	Phosphate (0–50m)	<0.0001	<0.0001	<0.0001	0.66
	Silicate (0–50m)	<0.0001	<0.0001	<0.0001	0.68
	Nitrate (50–150m)	<0.0001	0.09	<0.0001	0.49
	Phosphate (50–150m)	<0.0001	0.5	<0.0001	0.46
	Silicate (50–150m)	<0.0001	<0.0001	<0.0001	0.51
	Nitrate (300m)	<0.0001	<0.001	0.3	0.11
	Phosphate (300m)	<0.0001	<0.001	<0.0001	0.65
	Silicate (300m)	<0.0001	<0.0001	<0.0001	0.68
sGSL	Chlorophyll *a* (0–100m)	<0.0001	<0.001	0.001	0.27
	Nitrate (0–50m)	<0.0001	<0.0001	<0.0001	0.68
	Phosphate (0–50m)	<0.0001	<0.0001	<0.0001	0.69
	Silicate (0–50m)	<0.0001	<0.0001	<0.0001	0.61
	Nitrate (50–150m)	<0.0001	0.06	<0.0001	0.61
	Phosphate (50–150m)	<0.0001	0.3	<0.0001	0.63
	Silicate (50–150m)	<0.0001	0.06	<0.0001	0.61
eGSL	Chlorophyll *a* (0–100m)	<0.0001	<0.0001	0.003	0.17
	Nitrate (0–50m)	<0.0001	<0.0001	<0.0001	0.75
	Phosphate (0–50m)	<0.0001	<0.0001	<0.0001	0.78
	Silicate (0–50m)	<0.0001	<0.0001	<0.0001	0.78
	Nitrate (50–150m)	<0.0001	<0.0001	<0.0001	0.61
	Phosphate (50–150m)	<0.0001	0.003	<0.0001	0.55
	Silicate (50–150m)	<0.0001	<0.0001	<0.0001	0.51
	Nitrate (300m)	<0.0001	<0.0001	<0.0001	0.21
	Phosphate (300m)	<0.0001	<0.0001	<0.0001	0.6
	Silicate (300m)	<0.0001	<0.0001	<0.0001	0.53

Appendix 5. GLM results for Rimouski and Shediac Valley stations. Significance of the year and month effects as well as the adjusted R squared of the regression for each zooplankton index are presented.

Station	Index	Year (*p*)	Month (*p*)	R^2
Rimouski	*Calanus finmarchicus*	<0.0001	<0.0001	0.51
	Pseudocalanus spp.	<0.0001	<0.0001	0.56
	Total copepods	<0.0001	<0.0001	0.57
	Non-copepods	<0.0001	<0.0001	0.42
	Calanus hyperboreus	<0.0001	<0.0001	0.42
	Small calanoids	<0.0001	<0.0001	0.66
	Large calanoids	<0.0001	<0.0001	0.32
	Cyclopoids	<0.0001	<0.0001	0.59
	Copepods: Warm	<0.0001	0.8	0.49
	Copepods: Cold	<0.0001	<0.0001	0.44
	Dry weight	<0.0001	<0.0001	0.6
Shediac Valley	*Calanus finmarchicus*	<0.0001	<0.0001	0.33
	Pseudocalanus spp.	0.1	0.2	0.06
	Total copepods	0.2	<0.0001	0.18
	Non-copepods	0.001	0.0001	0.21
	Calanus hyperboreus	<0.0001	<0.0001	0.66
	Small calanoids	0.01	<0.0001	0.19
	Large calanoids	<0.0001	<0.0001	0.35
	Cyclopoids	0.07	<0.0001	0.22
	Copepods: Warm	0.1	0.06	0.07
	Copepods: Cold	0.08	<0.0001	0.3
	Dry weight	0.3	<0.0001	0.17

Appendix 6. GLM results for GSL subregions. Significance of the year, season, and station effects as well as the adjusted R squared of the regression for each zooplankton group are presented.

Region	Group	Year (*p*)	Season (*p*)	Station(*p*)	R^2
wGSL	*Calanus finmarchicus*	<0.0001	0.001	<0.0001	0.66
	Pseudocalanus spp.	<0.0001	<0.0001	<0.0001	0.54
	Total copepods	<0.0001	<0.0001	<0.0001	0.76
	Non-copepods	<0.0001	<0.0001	<0.0001	0.58
	Calanus hyperboreus	0.01	<0.0001	<0.0001	0.59
	Small calanoids	<0.0001	<0.0001	<0.0001	0.67
	Large calanoids	<0.0001	0.006	<0.0001	0.77
	Cyclopoids	<0.0001	<0.0001	<0.0001	0.72
	Copepods: Warm	<0.0001	0.007	<0.0001	0.53
	Copepods: Cold	<0.0001	<0.0001	<0.0001	0.66
	Dry weight	<0.0001	<0.0001	<0.0001	0.65
sGSL	*Calanus finmarchicus*	<0.0001	<0.001	<0.0001	0.30
	Pseudocalanus spp.	<0.0001	<0.001	0.6	0.12
	Total copepods	<0.0001	<0.0001	<0.001	0.32
	Non copepods	<0.0001	<0.0001	<0.0001	0.54
	Calanus hyperboreus	<0.0001	<0.0001	<0.0001	0.49
	Small calanoids	<0.0001	<0.0001	0.002	0.28
	Large calanoids	<0.0001	<0.0001	<0.0001	0.47
	Cyclopoids	<0.0001	<0.0001	<0.0001	0.38
	Copepods: Warm	<0.0001	<0.0001	0.2	0.53
	Copepods: Cold	<0.0001	<0.0001	<0.0001	0.40
	Dry weight	<0.0001	<0.0001	<0.0001	0.35
eGSL	*Calanus finmarchicus*	<0.0001	0.8	<0.0001	0.20
	Pseudocalanus spp.	<0.0001	<0.0001	<0.0001	0.26
	Total copepods	<0.0001	<0.0001	<0.0001	0.26
	Non-copepods	<0.0001	<0.0001	<0.0001	0.45
	Calanus hyperboreus	0.06	<0.0001	<0.0001	0.54
	Small calanoids	<0.0001	0.7	<0.0001	0.35
	Large calanoids	<0.0001	<0.0001	<0.0001	0.45
	Cyclopoids	<0.0001	<0.0001	0.001	0.32
	Copepods: Warm	<0.0001	<0.0001	<0.0001	0.49
	Copepods: Cold	<0.0001	<0.0001	<0.0001	0.39
	Dry weight	<0.0001	0.03	<0.0001	0.58